Optical Methods of Imaging In-plane and Normal Load Distributions Between Contacting Bodies

C G Tompkins

September 2022

Abstract

The work presented here details the creation of two novel force sensors: one which gives a direct optical measure of contact forces using Frustrated Total Internal Reflection, and another which measures the in-plane traction forces between contacting bodies using a matrix of dye-doped dots suspended in an elastomer film. The application of these devices shows how unique information of the contact mechanics between two bodies can be gathered. The contact device is used to study lower-body biomechanics during simple training exercises. The traction device is used for a more fundamental study of the shape dependence of friction in elastic media. This has resulted in a correction factor to the force distributions which may be used to increase the accuracy of simulations of this friction regime. It has also been determined that the shape dependence of friction is likely caused by compressive strain at the interface, and the mechanics of this investigated.

Publications

- Tompkins, Christopher Sharp, James. (2019). **Dual optical force plate for time resolved measurement of forces and pressure distributions beneath shoes and feet.** Scientific Reports. 9. 10.1038/s41598-019-45287-9.

- Tompkins, Christopher Sharp, James. **An optical imaging device for two-dimensional in-plane traction analysis**. Status: pre-print.

Acknowledgements

Firstly I would like to thank my supervisor, James, for his support and guidance over the years. Without this, I would not have completed this PhD. He also gave me the freedom to explore ideas and concepts on my own (with some sensible restraint!). This has helped me become an independent researcher able to identify my own strengths, and I am equally greatful for it.

Next, I would like to thank all of those people who have offered me professional and intellectual advice over the years. This includes George, Max, Stu, Darcey. Their wide range of skills and fields provided a uniquely wide knowledge base and skill set, which was indispensable. This should also include everyone in the tea room who listened to me complain whenever I couldn't get something to work!

Finally, I would also like to thank Fran for the emotional support throughout the years, and just generally being there when I needed something. She helped make a difficult process a lot easier, and has always been excited to listen to whatever random idea I have at any moment.

Contents

Chapter 1

Motivation

The overall aims of the work detailed here were to develop new methods of imaging the contact and traction forces at the interface between objects, in regimes and at length scales that other methods and technologies are unable to. In order to understand why research in this area is desired, the motivation behind each type of force sensing has been detailed here.

1.1 Traction Motivation

The frictional interaction between two bodies is a widely applicable topic and is frequently studied. This may fit into any length-scale one may imagine, from nanotribology, to geological and planetary sciences: the wearing of gears or other mechanical surfaces [1], the prediction and nature of earthquakes [2], and even single-atom manipulation [3] are prime examples of this range. One regime that is noteworthy in its use, and complexity of study, is the traction forces between elastic and inelastic interfaces.

Every vehicle and piece of footwear with a rubberised tread relies on this interface to transfer force from the object to the surface [4], and needs to be designed in such a way that the behaviour is predictable. Emerging fields of research, like soft robotics, also require knowledge of the frictional interaction in order to appropriately grip objects [5], [6]. Even well established fields require knowledge of this area to progress - polymer based gears have better shock resistance and do not require external lubrication, compared to metal gears, but the frictional and thermal wearing performance is not as well defined [7]. For simple materials, the theory behind these kinds of interactions is well

known: they are microscopic in scale and follow established models, such as the Greenwood model of friction [8]. Unfortunately, it is well known that frictional forces in elastic materials do not obey classical friction laws [9], and instead introduce unique phenomena such as shape dependent friction. Without a complete theory, nor a way to easily spatially resolve the traction forces, developing the most efficient (or indeed safest [10], [11]) tread patterns is a labour-intensive task.

The lack of understanding of elastic frictional interactions, coupled with their prevalence in industry and science, has already driven interest into this field. This began by using methods such as photoelasticity [12], [13] and total internal reflection [14], [15] to study the shape of (and strain under) interfaces under sliding millimetre objects. However, full two-dimensional spatial resolution of these interfacial forces had yet to be achieved, leaving gaps in both knowledge and what fields these methods may be applied to. This has therefore driven the development of a new prototype device capable of spatially resolving these forces, detailed in this work. By using this device to study simple geometries, it was then hoped that a cause of the shape dependence could begin to be quantified.

1.2 Contact Motivation

As for the desire to measure the contact forces involving soft bodies, there is similar ubiquity: these can still involve the contact forces under objects like shoes or tyres, where the ability of a material to evenly distribute load naturally also has an influence on the scale of the traction forces experienced and their ability to resist impact [16], but is also further reaching. There are various medical applications where the contact forces a person can apply have been shown to correlate to various types of illness [17] or injury [18]–[20]. This has led to interest in custom developed orthotics [21] or prostheses [22], designed for the specific needs of a patient. Although methods to image these kinds of forces already exist, they are generally quite expensive and offer a limited resolution. It is arguable that techniques such as atomic force microscopy already have the required resolution, however their slow speed and inability to account for large simultaneous contact areas make them unsuitable to study

the dynamic and (overall) macroscopic contacting objects considered here [3].

As for theoretical models, these are long established. A. E. H. Love was one of the first to record a complete theory of contact mechanics [23]. As noted in his work, however, only very few objects have shapes and mechanical properties simple enough to be modelled accurately. Even dust or thin-film layers between contacting objects have been shown to wildly alter expected results [24].

This has therefore driven the development of optical methods of contact force measurement, as they potentially offset these disadvantages. A method which has existed for some time is based on Frustrated Total Internal Reflection (FTIR), although the technology of the time limited analysis to mere inference [25]. It was not until recently that the method was revisited, slowly developing from the analysis of contact patch sizes under mathematically well-understood objects [26], to a method able to infer the forces under arbitrarily shaped soft objects [27], [28]. It was therefore the intention of this work to build on these newly discovered features to design and apply a new FTIR contact sensor to investigate contact forces in a biomechanics setting – an area where the dynamic, high resolution, and non-invasive nature of the imaging method is a marked advantage.

Chapter 2

Introduction & Background

2.1 Contact Background

The measurement of contact forces is a concept with an understandably large range of applications: measuring the contact forces between mechanical parts is naturally desirable in engineering, where frictional wearing between mechanical parts is a common problem. It is even applicable in advanced fields like soft robotics [1], [2], where some measurement of the contact forces are required to appropriately grip objects. For example, surgical robots must be capable of applying delicate forces of a specified amount, to not damage tissue. Further afield, even certain atomic force microscopy methods take advantage of measuring contact forces to image the position of atoms [3]. The more precise methodology of interest here is the measurement of contact forces between macroscopic soft contacting objects.

Measuring the contact forces between specifically soft objects also has wide ranging applications: Sports science and medicine are both fields where the bio-mechanical aspect is important. The contact forces a person can produce can be indicative of muscle growth and injury [4]–[6]. Designing physiotherapy routines or footwear based off of this kind of data is therefore of interest, but the current methods of measuring contact forces that are available are not suited to tasks requiring high spatial resolution or accuracy.

From a theoretical standpoint, the basic contact mechanics of these situations have been well known for over 100 years. One of the first to outline the elastic contact theory in its entirety was A. E. H. Love, in 1897 [7]. The

complete detail of the derivation is mathematically complex, indeed it takes an entire book to explain in its entirety, but some key components are worth noting. The simplest case to theoretically define, on which all others are based on, is a point load applied to a half-space. This half-space is assumed to be purely elastic, while the point load is solid and incompressible, and the contact load is uniform and approximated to a point. This setup is shown in figure 2.1 for clarity.

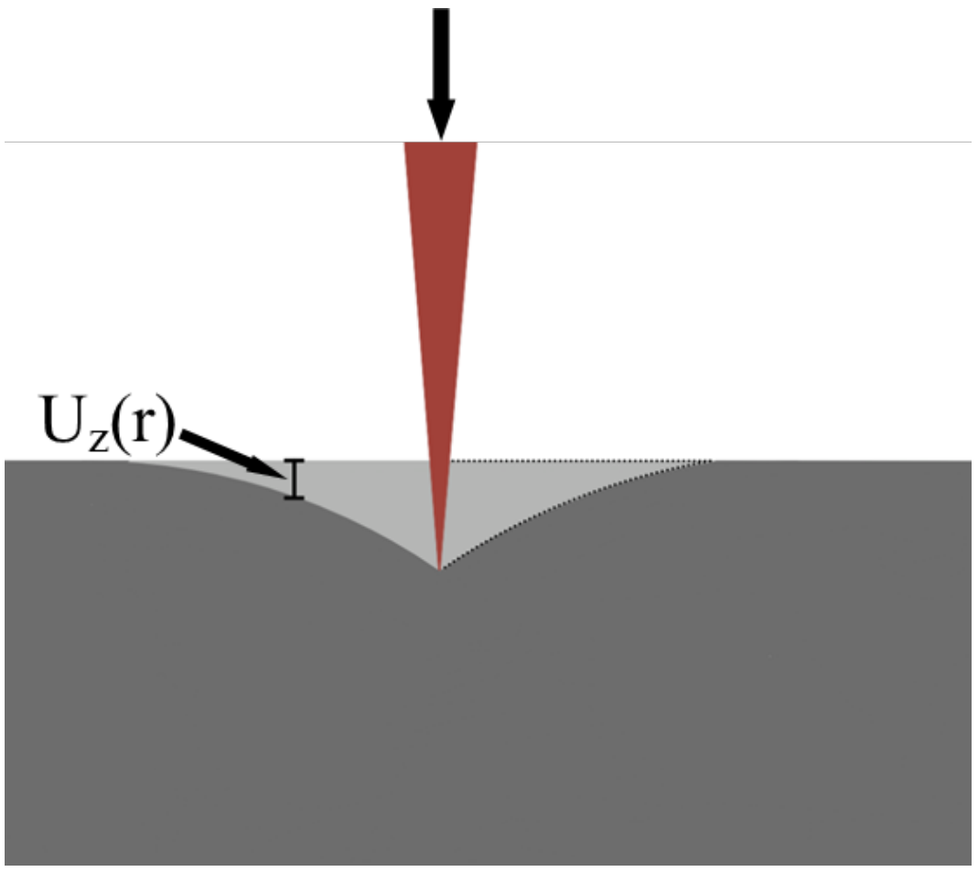

Figure 2.1: An example of the simplest contact loading setup: point loading an elastic half-space. A thin point (red) approximated as infinitely small at the tip is loaded vertically, and deforms the half-space. The half-space is indicated in grey, showing a cross section of the radially symmetric deformed (dark) and undeformed (light) states. The profile of the deformation is indicated by the dotted line and decays as $\frac{1}{r}$, where r is the radial distance from the centre of the loading. The induced deformation in the direction of loading (u_z) is therefore a function of the applied load and distance from the origin. Simple experiments like this, where the radial profile could be easily measured for different materials, allowed basic contact mechanics theory to develop.

As well as the simplest case to define mathematically, this is also an easy experimental system to approximate. By using a long and fine needle as an approximate point load, it was simple to visually assess how the plane responded to various contact loads, and build the accompanying theory accordingly [7]. It was found that by applying a point load P to the plane with a shear modulus

G, the displacement in the z direction (normal to the plane) of a point within the surface u_z was

$$u_z = \frac{P}{4\pi G}\left(\frac{z^2}{r^3} + \frac{2(1-\nu)}{r}\right). \tag{2.1}$$

Here, r is the radial distance away from the point load, and ν is the Poisson ratio of the elastic surface. At the top of the half-space, where $z = 0$, this simplifies to

$$u_z(z=0) = \frac{(1-\nu)}{2\pi G}\frac{P}{r}, \tag{2.2}$$

which has been indicated on figure 2.1 above, to show how this relates to the observed profile. This profile decays as $\frac{1}{r}$ from the distance to the point of contact. From this result, it is also trivial to compute the displacements in the remaining axes. As the volume of any element of the surface must be conserved, then the x and y displacements are easily found [8] and can be converted to a radial displacement for convenience [9]:

$$u_x(z=0) = -\frac{(1-2\nu)}{4\pi G}\frac{Px}{r^2}, \tag{2.3}$$

$$u_y(z=0) = -\frac{(1-2\nu)}{4\pi G}\frac{Py}{r^2}, \tag{2.4}$$

$$u_r(z=0) = -\frac{(1-2\nu)}{2\pi G}\frac{P}{r}. \tag{2.5}$$

Knowing how a surface will deform in response to a point load is, by itself, of limited use. However, these results may also then be applied to more complex objects. The next simplest case considers a load which is not a point, but rather the non-infinitely small equivalent: a flat-ended cylinder with radius a.

When a flat ended cylindrical punch is considered, the results are similar: there is still a radial decay outside of the contact region, and inside the contact region the pressure is dependent on the contact load. The key difference is the contact pressure observed by each point, according to Hertzian contact theory [10], which also varies radially:

$$P(r) = \frac{p_0}{a}\left(a^2 - r^2\right)^{\frac{1}{2}}, \tag{2.6}$$

where p_0 is the pressure experienced at the centre of the contact region.

Incorporating this varying pressure distribution by integrating over all elements in the surface then gives new expressions for u_r [8]:

$$u_r = -\frac{(1-2\nu)}{4G}\frac{a^2}{r}p_0\left[1-\left(1-\frac{r^2}{a^2}\right)^{\frac{3}{2}}\right], \quad r \leq a, \tag{2.7}$$

$$u_r = -\frac{(1-2\nu)}{4G}\frac{a^2}{r}p_0, \quad r > a, \tag{2.8}$$

This can be considered to be a sum of an infinite number of point loads, with a well known pressure distribution, but what of an arbitrary shape? The same process of summing an infinite number of point loads can be applied to any object. However, if the object cannot be described quantitatively, then numerical solutions are required. This can be computationally intensive for complex shapes and dynamic loading, becoming impractical even on modern hardware [11], and therefore experimental measures are important. These results are still extremely useful, and help provide simple situations that can be used to test and calibrate experimental devices, which can then be applied to cases the theory cannot.

Experimental methods are therefore significantly more ideal in the complex everyday situations explored by the previously mentioned fields. There are a number of technologies that can spatially resolve these forces, although all are currently some variant of a force plate. These consist of an array of electrically addressable load cells, which must be placed between the contacting object and the surface (say, inside a shoe, like the cases studied here), and are well known to introduce errors simply from the fact that they are a bulky rigid additional interface, i.e. they are not a direct measurement and can in fact alter the way a person moves because they are bulky and uncomfortable. The sensors themselves are also of a finite size, and this results in fairly low resolution images, such as the example in figure 2.2.

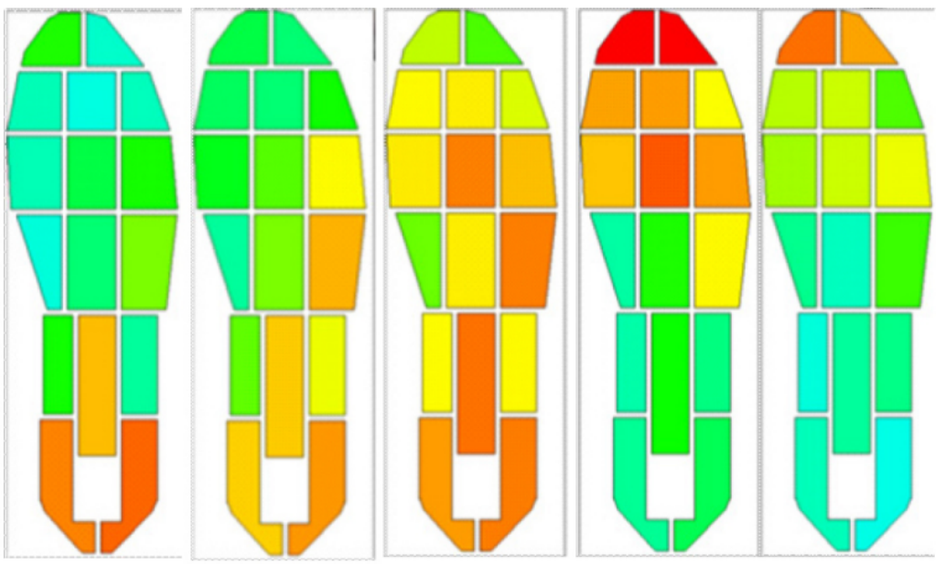

Figure 2.2: An example of the pressure images from a standard piezoelectric force plate [12]. As they measure compression, but a solid working surface is required, these often only have a small number of sensor elements supporting a ridged plate. Therefore, only the net load distributed in each axis is discernible. Higher details require a compressive surface, which can be added inside of a shoe. The available viewing area is small and the resolution is low because of the limited size of the individual sensors. They also do not provide a direct measure of the forces at the interface between the foot and platform, but rather at the compressive element in the middle of the device. This limits both the accuracy and resolution of the data they produce.

Depending on the exact application, sensors which take advantage of different effects may be built into these force plates. One is to take advantage of the piezoelectric effect, where adding strain to a piezoelectric crystal (in this case, compressing it), produces a small voltage. The piezoelectric effect only measures changes, however. If the crystal remains in the compressed state, no voltage will be produced until the load changes. To get static changes, which are commonly needed in the situations considered here (e.g. a person standing still), capacitive load cells are used. Here, each element is a thin film (parallel plate) capacitor: two plates that are significantly larger in area A than the gap which separates them d, which is filled with a material with permittivity ϵ. The capacitance C of this capacitor is known to vary as approximately

$$C = \frac{\epsilon A}{d}. \tag{2.9}$$

Therefore, as a load compresses the capacitive cell, d decreases and C increases. This change in capacitance can be measured by measuring the voltage across the cell, and therefore calibrated to measure force. These are, however, only the standard methods used in commercial devices and common applications. There

has been recent work in developing an entirely new method, which removes the need to add an object between the contacting interface, and has much higher resolution [13], [14]. This method takes advantage of frustrated total internal reflection.

2.2 Frustrated Total Internal Reflection

Recent advanced methods of contact force imaging take advantage of frustrated total internal reflection (FTIR) to directly measure the forces at the interface between a transparent and opaque object. In order to understand how this works, it is first worth understanding what FTIR is, and how this differs from the traditional assumptions involved with total internal reflection. It should also be noted that there are other (more common) uses of the acronym FTIR, such as Fourier-transform infrared spectroscopy. These represent very different techniques/physical phenomena and the reader should therefore be careful when assuming familiarity.

Total internal reflection, as the name suggests, generally considers the light transmitted through some medium i remains within said medium, with no component transmitted through to the surrounding material t. Instead, the light reflects back into material i at the boundary between the two materials. This is straightforward to achieve: the material i will have a critical angle θ_c dependent on the refractive indices n of both itself and the surroundings t [13]:

$$sin\theta_c = \frac{n_t}{n_i}. \tag{2.10}$$

If the angle of the light incident to the boundary between materials i and t is less than the critical angle, the light will be contained within material i. This is the traditional view of total internal reflection. When Maxwell's electromagnetic boundary conditions are considered, however, this view becomes suspect [15], [16].

Maxwell's equations consider light to be an electromagnetic wave, rather than a particle or ray. It has been shown that rearranging these equations gives the following boundary conditions between two media (i and t in this

example) [16]:

$$\hat{n} \times \mathbf{E} = -\mathbf{J}_m, \quad \hat{n} \cdot \mu\mathbf{H} = \rho_m \tag{2.11}$$

$$\hat{n} \times \mathbf{H} = \mathbf{J}_e, \quad \hat{n} \cdot \eta\mathbf{H} = \rho_e. \tag{2.12}$$

Here $\hat{n}$ is a unit vector normal to the interface, $\mathbf{E}$ is the electric field, $\mathbf{H}$ the magnetic field, and $\mathbf{J}$ and ρ denote the current and charge distributions across the boundary (e and m for electric and magnetic fields, respectively).

In the case of total internal reflection, there can be no flow of current transmitted into material t, so $\mathbf{J} = 0$. Now, by expanding out the boundary conditions, the problem with classical internal reflection becomes obvious:

$$\hat{n} \cdot (\mathbf{E}_i - \mathbf{E}_t) = E_{iz} - E_{tz} = 0 \tag{2.13}$$

$$\hat{n} \cdot (\mathbf{H}_i - \mathbf{H}_t) = H_{iz} - H_{tz} = 0 \tag{2.14}$$

$$\hat{n} \times -(\mathbf{E}_i - \mathbf{E}_t) = \begin{bmatrix} (E_{iy} - E_{ty}) \\ -(E_{ix} - E_{tx}) \end{bmatrix} = 0 \tag{2.15}$$

$$\hat{n} \times (\mathbf{H}_i - \mathbf{H}_t) = \begin{bmatrix} -(H_{iy} - H_{ty}) \\ (H_{ix} - H_{tx}) \end{bmatrix} = 0 \tag{2.16}$$

In this case $\hat{n}$ has been taken to be $0\hat{x} + 0\hat{y} + 1\hat{z}$. There must be some components of the electric and magnetic fields in material t to prevent current flow, but as there is no current flow, these fields cannot transmit energy.

This problem is, unsurprisingly, similar to the commonly demonstrated problem of an electron tunnelling through a potential well. The solution therefore takes a very similar form: there must be a wave transmitted into material t with a complex amplitude, such that the time (s) averaged intensity is 0 [15]:

$$\mathbf{E} = \mathbf{E}_0 e^{-\alpha x} e^{i\omega s} \tag{2.17}$$

These waves are referred to as evanescent waves, where α and ω are the attenuation and phase constant respectively.

This is the solution for two media, but what if a third medium is brought close

to material t, such that the amplitude of the field has yet to decay to 0? This setup is illustrated in figure 2.3.

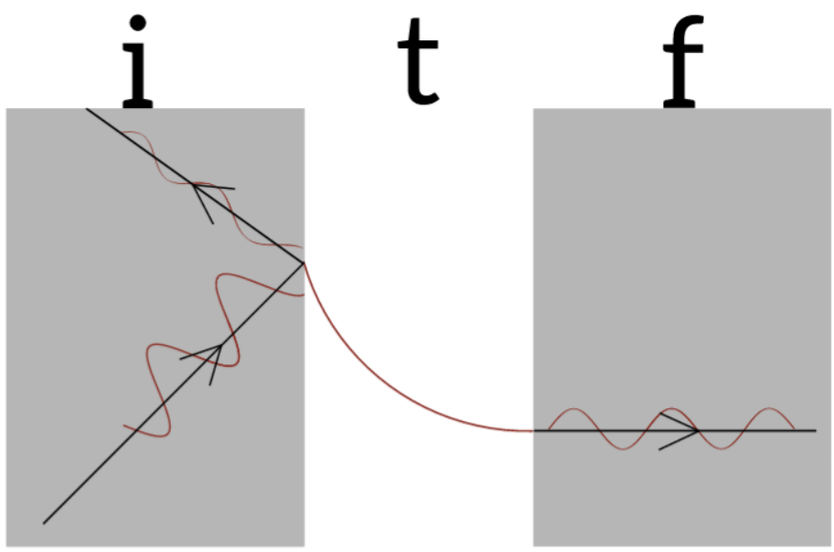

Figure 2.3: An illustration of the propagation of an evanescent wave and Frustrated Total Internal Reflection (FTIR). The classically observed ray paths are drawn in black, and the wave form of light is illustrated in red. There are three materials involved: The original medium i in which the light (classically) remains totally internally reflected, e.g. glass. Medium t is a material with a refractive index such that the light (classically) does not penetrate, e.g. air. Medium f is the material which "frustrates" the internal reflection when brought close enough to material i that the amplitude of the evanescent wave in t has yet to decay to 0. Material f has be a material which would not cause internal reflection under these conditions, e.g. a second layer of glass. No classical wave is observed in material t, however there is an evanescent wave with an amplitude E which decays with distance x into the medium: $E = E_0 e^{-\alpha x}$, where α is the attenuation coefficient. In material f, the wave once again propagates, but with lower amplitude than in material i (i.e a lower probability of finding a photon) due to being attenuated.

If this third material has a refractive index which would not allow total internal reflection, then once again the wave may transmit as normal, although with a reduced intensity due to the decay in material t reducing the probability of finding a photon in this medium. In this way, energy has been transferred to the third medium. Consider if this third medium contains material which scatters the light, and varies in height so that only part of it is close enough to material i to transfer energy to. The material will locally scatter light, only in positions close enough to material i to frustrate the internal reflection, and therefore could be used as a sensor to map the contact patches between the two materials: an FTIR imaging sensor.

2.3 FTIR Contact Forces

It has been known for some time that the FTIR phenomenon can be taken advantage of to measure various features of contact patches. This has included simple measures of the contact area of grains in a silo [17], to more complex measurements of coupling applied pressure to intensity [14], [18]. It is the latter that is of the most interest here: it was observed by Betts and Duckworth in 1985 that regions of higher pressure between feet and an FTIR waveguide had increased brightness, compared to the lower pressure regions [18]. At the time, there were no mass produced digital cameras of any kind, so the ability to analyse the intensity vs pressure was limited. However, recent advancements in digital imaging and machine vision technology mean that this has recently become possible in a general lab setting.

To begin with, the setup must be imagined: there is a contacting object that consists of many microscopic asperities, pressing against what is assumed to be a smooth waveguide plane. An asperity is a single feature of the microscopic surface roughness, and may take any size within this range. In the specific case of FTIR, it is considered to be a transparent medium, containing many smaller scatterers (e.g. dye molecules). These asperities are assumed to not adhere to the surface in any way, so their contact is governed by Hertzian contact mechanics, rather than JKR contact mechanics (the latter describing adhesive contact between an asperity and surface) [8]. Some distance below this is a sensor used to image the scattered light intensity. If the original light intensity at any point is I, then the sensor will observe a different intensity dI_s, due to the light being scattered off molecules in the asperity. This scattered light will then spread out over a larger area, lowering its intensity, as it travels further from the source. The intensity at the observer will then be [13]:

$$dI_s = \frac{8\pi^4\alpha^2(1 + cos^2\theta_s)N_s}{\lambda^4 D^2} I. \tag{2.18}$$

Here, α represents the polarisability of the scattering objects, N_s is the number of said scatterers, λ is the wavelength of the light which is being scattered, D is the separation of the source and observer, and θ_s is the scattering angle. It has been assumed that Rayleigh scattering occurs. So long as the scattering

particle diameters are $\sim \frac{1}{10}$ the wavelength of the light used (e.g. dye molecules trapped between the crosslinks in a polymer, and visible light), this criterion is valid [15]. This gives a scattering intensity $I_s \propto \frac{1}{\lambda^4}$. This is opposed to Mie scattering, which occurs at any particle sizes above this range. Instead of a simple proportionality, an infinite series of spherical harmonics must be solved for Mie scattering [15].

The original scattered intensity I along this line between the source and the observer is then naturally dependent on the intensity of the pre-scattered ray I_0. This is an evanescent wave, which has a decay related to the distance outside of the waveguide. This decay takes the form [13]:

$$I = I_0 exp\left(\frac{-4\pi n_0 cos\theta_r z}{\lambda}\right). \tag{2.19}$$

n_0 is the refractive index of the asperity (the material the evanescent wave is tunnelling into), $cos\theta_r$ is the refraction angle, and z captures the distance between the point on the asperity and the flat plane (where z is the vertical separation). This has been shown schematically in figure 2.4, for clarity.

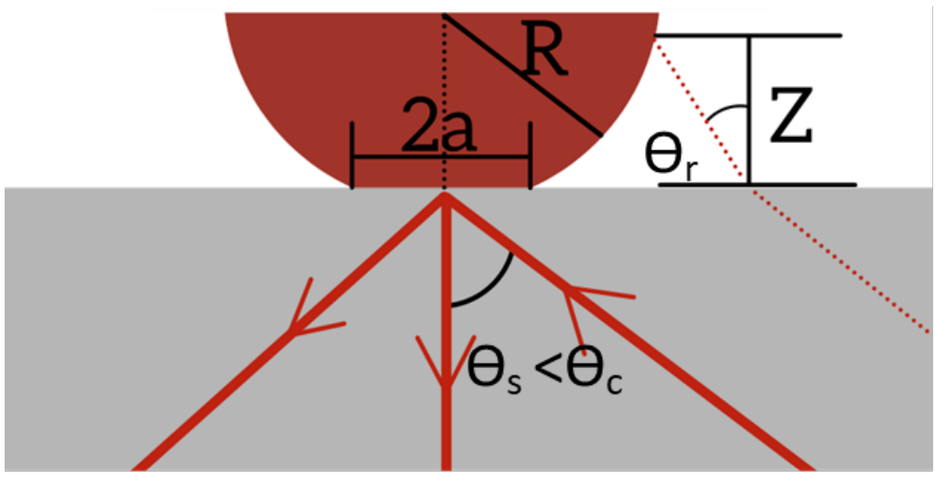

Figure 2.4: A diagram of the arrangement of a single asperity of radius R, pressed into a semi-infinite plane, such that the contact patch between the two has radius a. A red ray path is incident at the boundary between the two, and remains totally internally reflected so long as the incident angle θ_s is less than the critical angle at the interface θ_c. A back scattered ray path is also shown normal to the interface, this is an evanescent wave which has scattered off the asperity. Using a dotted ray as an example, the refraction angle θ_r has been defined. This ray has been offset for clarity; it is actually passing through the asperity.

The term $cos\theta_r$ then dependent on what angle the ray inside the waveguide was incident (θ_i), and the refraction as it passes through the interface:

$$cos\theta_r = \left(\left(\frac{n_w}{n_0} \right)^2 sin^2\theta_i - 1 \right)^{\frac{1}{2}}. \tag{2.20}$$

Here, n_w is the refractive index of the material that makes up the waveguide. This models how light scatters from an individual scattering object, but each sensor/optical element in the observer will be detecting multiple scattering objects simultaneously, so it is now necessary to scale the observed intensity accordingly.

If the number density of scatters in the contacting object is ϕ, then a small volume element with area A and thickness dz will have

$$N_s = \phi A dz \tag{2.21}$$

scattering objects. As the load on an asperity is increased, like in the case of friction, the asperity will deform and ϕ will vary. Each small element of surface will experience a strain (ϵ_z), this will change the volume of the element and (assuming uniformly distributed scattering objects), ϕ will change equally with this. If the number density of scatterers in the undeformed state is ϕ_0, then

$$\phi = \frac{\phi_0}{1 - (1 - 2\nu)\epsilon_z}, \tag{2.22}$$

where ν is the Poisson's ratio of the asperity material. This is simply based on how the volume (and hence density) within any small section of the asperity changes. It is known that, for changes in volume (ΔV) much less than the overall volume of the element (V), that [8], [13]

$$\Delta V = V\,(1–2\nu)\,\epsilon_z. \tag{2.23}$$

When a load is applied to the asperities, they will deform and increase the size of the contact patch, increasing the back-scattering. Assuming a uniform total force F is applied, and that each asperity is a spherical hemisphere $\sim 4R^2$ in area, then the force inferred at each element in the sensor (with area A_{pp}) F_{pp}

will be:

$$F_{pp} = F\frac{A_{pp}}{4R^2}. \tag{2.24}$$

The total light intensity contribution each sensor observes (I_{pp}) will then also scale this way:

$$I_{pp} = I_s\frac{A_{pp}}{4R^2}. \tag{2.25}$$

It is well known, however, that the pressure distribution within a hemisphere is not uniform, and in fact varies with radius [8]. This will mean each element in the hemisphere $2\pi rdr$ will contribute a different intensity to the total amount of back-scattered light, depending on the strain distribution. The strain distribution ϵ_z between the contacting bodies, with a contact patch of radius a has a well known solution [10]:

$$\epsilon_z = \frac{1}{E}\left[(1-\nu)\sigma_z - 2\nu(1+\nu)\sigma_0\frac{z}{a}\left(tan^{-1}\left(\frac{a}{\sqrt{u}}\right) - \frac{a}{\sqrt{u}}\right)\right], \tag{2.26}$$

where E is the Young modulus and ν is the Poisson ratio of the asperity material. The contact patch radius a takes the form

$$a = \left(\frac{3FR(1-\nu^2)}{4E}\right)^{\frac{1}{3}}, \tag{2.27}$$

the relevant stress fields are

$$\sigma_0 = \frac{3F}{2\pi a^2}, \tag{2.28}$$

and

$$\sigma_z = \sigma_0\left(\frac{u}{\sqrt{u}}\right)^3\frac{a^2u}{u^2+a^2z^2}. \tag{2.29}$$

Finally, the displacement u is represented in the polar coordinate system by:

$$u = \frac{1}{2}\left(r^2+z^2-a^2+\sqrt{(r^2+z^2+a^2)^2+4a^2z^2}\right). \tag{2.30}$$

This shows how each volume element within the asperity, $2\pi rdrdz$, contributes to the back-scattered intensity dI_s. To find the total back-scattered intensity from each asperity, equation 2.26 must be substituted into equation 2.22, to get the density of scattering objects in the strained asperity, then this result and equation 2.19 substituted into equation 2.18. The final result gives the total scattered intensity from each asperity, when integrated over the contact

volume of the asperity [13]:

$$I_s = \frac{16 I_0 \pi^5 \phi_0 \alpha^2 (1 + cos^2\theta_s)}{\lambda^4 D^2} \int_0^a r \int_0^\infty exp\left(\frac{-4\pi n_0 cos\theta_r z}{\lambda}\right) \times \left(1 - \frac{(1-2\nu)}{E}\left\{(1-\nu)\sigma_z - 2\nu(1+\nu)\sigma_0 \frac{z}{a}\left[tan^{-1}\left(\frac{a}{\sqrt{u}}\right) - \frac{a}{\sqrt{u}}\right]\right\}\right)^{-1} dr dz. \tag{2.31}$$

This is the complete solution, however the integral has no known universal solution. In order to produce one, some approximations have to be made.

If the deformation is assumed to obey Hertzian contact theory, i.e. $a << R$, then the strain can be approximated as [8]:

$$\epsilon_z \approx \frac{3F(1-\nu^2)}{8ERa^3}(2a^2 - r^2). \tag{2.32}$$

Recomputing the expression in equation 2.31 gives a result with a known solution:

$$I_{pp} = \frac{\pi^4 A_{pp} I_0 \alpha^2 (1 + cos^2\theta_s)\phi_0}{2\lambda^3 D^2 n_0 cos\theta_r} \left[\frac{3F_{pp}(1-\nu^2)}{EA_{pp}}\right]^{\frac{2}{3}}. \tag{2.33}$$

Grouping parameters together gives a power law expression of

$$I_{pp} = \beta F_{pp}^a, \tag{2.34}$$

where β is a parameter which captures the material properties, and a is the power law. Expressions of this form should be valid for surface roughness values along the entire microscopic range, and have been experimentally verified down to an rms roughness of 8 µm [13]. It must be noted here that, according to the equation above, a should equal $\frac{2}{3}$. However, it has been shown experimentally that $\frac{1}{3}$ is also valid, at loads large enough that the Hertzian assumption breaks down [13]. It is this method of FTIR based force sensing that was applied in the contact imaging work detailed here.

The way all of this theory comes together to be used as a force sensor is as follows: On length scales of the order of the wavelength of light, The waveguide and contracting object appear as the two surfaces in figure 2.3, with an evanescent wave tunnelling between them. Scatterers, embedded in the object, backscatter the tunnelled light as long as they are close enough

that the light intensity has not decayed to zero. At the microscopic scale, where individual asperities are visible, they deform and scatter more light according to figure 2.4. Higher pressures increase the contact area and bring more scatterers close to the waveguide, this increases the amount of light scattered from each asperity. Finally, at the macroscopic level, where it appears the whole surface of the object is in contact, locally higher pressures lead to higher scattered light intensity. This can be used to produce higher resolution force maps than those in figure 2.2. This has been summarised in figure 2.5.

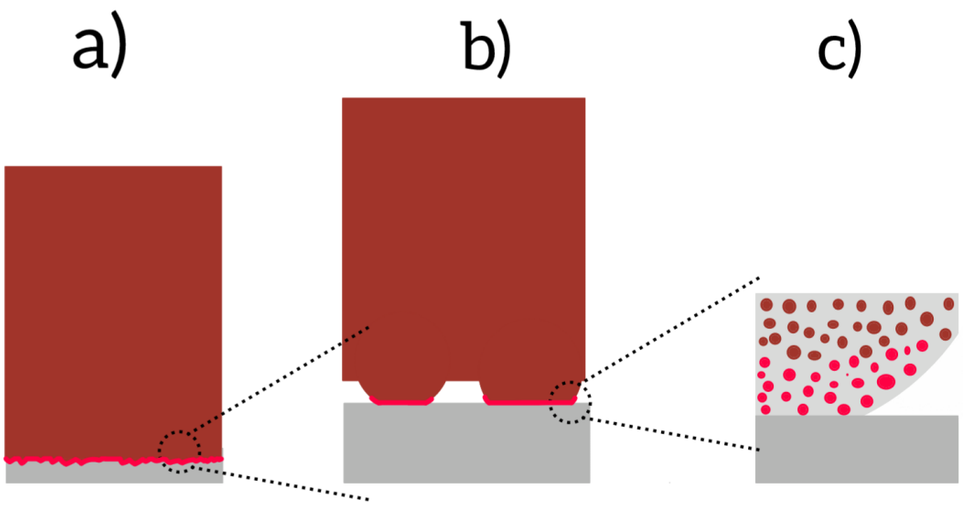

Figure 2.5: A summary of how the contact of an object (red) with an FTIR waveguide (grey) appears at different lengths scales. The regions which scatter light are highlighted in a brighter, "glowing", red. At the macroscopic level, the entirety of the rough face appears to be in contact with the waveguide. Scattered intensity increases as it is pressed harder into contact. At length scales where individual asperities can be observed, it is seen that the asperity deforms as the object is loaded, increasing the contact area and the net scattering. Finally, at the sub-asperity level, individual dye molecules in the transparent medium can be seen. Only those within a few wavelengths of the waveguide frustrate the internal reflection condition and scatter light. By pressing harder on the object and moving more dye molecules closer to the waveguide, scattering increases.

2.4 Frictional Forces and Traction Measurement

There is little concrete understanding in regard to the kinds of traction forces analysed here. Many objects require some understanding of the traction forces involved in order to function well, shoe soles and vehicle tyres are two extremely common examples [19]–[21]. However, it is also well known that these areas are of great commercial interest, and as a result the research is almost always publicly unavailable.

There is, however, much more study on the fundamental tribological theory for generic friction. These situations are, however, quite complex and it is worth explaining the origin of classical friction first. Classical friction is considered to be the case where Amontons' law applies [22]: $F = \mu W$. Here, F is the friction force, μ the coefficient of friction, and W the weight of the object. The standard argument for this is as follows. Consider two rigid surfaces, at rest, that are macroscopically smooth. On the microscopic scale, the surfaces are nolonger smooth but are made up of jagged peaks, termed asperities. It must be emphasised here that, as the surfaces are at rest, only static friction is being considered. Dynamic friction, when one object is moving (e.g. sliding/rolling), follows similar arguments, but with asperities which are pre-deformed. When pressed together by some normal force N, these asperities will press together and deform. Contacting asperities will have some interactive force between them, generally Van Der Waals forces, although this may change with the material. The force required to break this attractive force, and deform asperities so they may slide over each other, is the origin of friction. Hence, the frictional force between two surfaces is dependent on the contact area of all at the interface asperities which come into contact. The total (real) area of contact (A_r) is therefore not the overall size of the contacting interface (apparent area, A_n), but is the sum of the total areas of contact of all the individual asperities (A_i):

$$A_r = \sum_i A_i < A_n. \tag{2.35}$$

Two assumptions are now made: the first is that the asperities are approximately hemispherical. The second is that the area of contact between asperities is proportional to the contact load. This results in the standard friction equation for static friction.

It must be noted that Hertzian contact mechanics dictates that the contact area between spheres actually scales as $A^{\frac{1}{3}}$, not the assumed A^1, so this assumption is quite large and provides a base or more detailed theories explained later [10]. However, these arguments are commonplace and also used to understand kinetic friction. Therefore, for now, the simpler picture will be used for the sake of clarity.

Kinetic friction is the resistive force between two moving bodies, and is generally less than the static friction at the same interface. Consider again contacting asperities. When the surfaces are pressed together and moving, rather than forming two flat interfaces, peaks instead begin to glance off each other. As they move over each other, new interfaces are formed and broken, and breaking these interfaces requires some force. The area of the deformed interfaces are less than the area in the static case, so they require less energy to break, hence kinetic friction being lower than static friction.

These theoretical derivations are already somewhat ill-defined, but to be of use in real world situations they would need to be adjusted for even more complex features, like elastic objects (which deform macroscopically), or even dust (which would add additional layers of interfaces). This has necessitated empirical analysis of friction.

The simplest and oldest methods of experimentally measuring friction are still commonly used [23]–[25]. The first is to place an object on a movable incline and increase the angle of inclination (ϕ). The weight of the object, which normally acts vertically, will now have a horizontal component. As a result of balancing the inclined forces, the coefficient of static friction μ can be computed from the slip angle ϕ:

$$\mu = tan\phi. \tag{2.36}$$

The second method is to simply attach a strain gauge horizontally to an object resting on a flat surface and pull. The force required to pull the object will give measurements of both the static and kinetic friction coefficients. These same methods can be applied to materials that do not follow Amontons' law, such as adhesive or lubricated surfaces.

It is clear, however, that these measurements are total measurements: they give the coefficient of friction under an entire object and do not take into account surface variations. This is a significant limitation, especially with elastic surfaces, as it is known that shape has an effect on the traction distribution [26]. From a theoretical standpoint, this can be taken into account using finite element modelling (FEM) simulations. Assuming the bulk behaviour of the materials is well enough defined, the local forces can be approximated. Of course, comparing approximate simulations to experimental data is not necessarily ideal, and there are a few experimental methods that have previously been employed instead.

The most common method, when at least one of the contacting bodies is elastic, is to use photoelastic stress analysis.

2.5 Photoelastic Stress Analysis

Certain materials, while generally optically isotropic, become polarised when subject to a stress or strain. This is caused by the normally isotropic molecules in the material aligning to some uniformly twisted state, becoming a birefringent polariser. This is illustrated in figure 2.6.

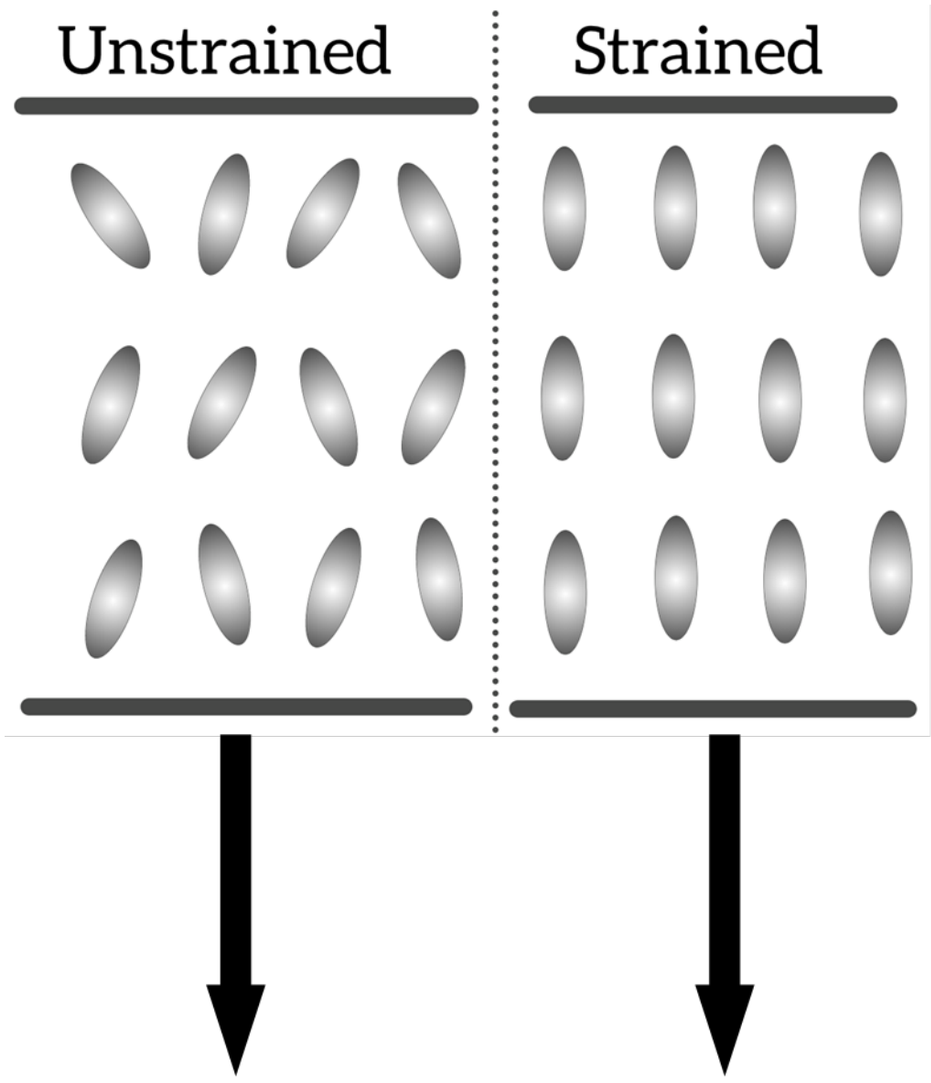

Figure 2.6: An example cross section of the strained and unstrained states of molecules in a birefringent material. When unstrained, the molecules are free to align randomly and there is no net polarisation. Applying a strain (indicated by the arrows) causes the molecules to align proportional to the shear displacement at that depth. The result is a net polarisation only along the axis perpendicular to the strain.

In this polarised state, an incident light ray experiences two refractive indices, as long as it is incident perpendicular to the optical axis - i.e. it travels perpendicular to the applied stress/strain. This ray will then split into two, with two different velocities, v_1 and v_2. These rays will then exit the material of thickness h at different times, which is referred to as the relative retardation δ. If the difference between the two refractive indices is Δn, then the relative retardation is expressed as

$$\delta = \frac{2\pi h}{\lambda}\Delta n, \tag{2.37}$$

where λ is the wavelength of the incident light [27]. These two waves, original and retarded, may now interfere with each other to give a new transmitted signal. The intensity of this transmitted signal (I_p), which is proportional to

the square of the wave amplitude, has been shown to take the form [27]

$$I_p = I_a sin^2 \frac{\delta}{2} sin^2 2\theta. \tag{2.38}$$

I_a is the intensity of the incident light and $sin^2 \frac{\delta}{2}$ term captures the interference between the original and retarded waves. The $sin^2 2\theta$ captures the polarisation state of the light, relative to the stress axis. That is to say, if the light is already polarised in one direction (say vertical), and the material is stressed in the opposite direction such that there is a $\frac{\pi}{2}$ phase difference and the polarisers are perfectly crossed (say horizontal), the transmitted signal will drop to 0.

The expression in equation 2.38 therefore gives two reasons for any apparent fringe patterns, what are known as isoclinics and isochromatics. Isochromatics are contours of constant colour, caused by the retardation. They are referred to as such because the colour and retardation in equation 2.37 are both wavelength dependent. This means the frequency of any fringe pattern, for a given stress (σ), varies with the wavelength of light passed through it. It is known that the stress in the material is linearly related to the refractive index by some material dependent coefficient (C), the stress-optic coefficient [27]:

$$\Delta n = C \Delta \sigma. \tag{2.39}$$

Therefore I_p can be related to the stress, by the stress-optic law:

$$I_p = I_a sin^2 \left(\frac{\pi h}{\lambda} C \Delta \sigma \right) sin^2 2\theta. \tag{2.40}$$

The $sin^2 2\theta$ is the isoclinic term; they are contours of constant alignment between the polarised light and the axis of the stress. As a result, these can be used to determine the angle of the applied stress, but obfuscate the stress-optic relation. Circularly polarising the initial light, so there can no longer be any axial alignment, removes isoclinics and allows the stress to be coupled purely to the intensity contours [15].

The ability to directly couple the intensity of optical contours to stress can be

taken advantage of to produce what is known as a polariscope. In a polariscope, polarised light is passed through a birefringent material and then through a second polariser, which is crossed with the first. The polarisation of the birefringent material can be induced in various ways: by an electric field (in the case of liquid-crystal displays [28]), stress frozen in during cooling (extruded plastics like poly-carbonate [29]), or strain in photoelastic materials. In the regions where the birefringent material alters the polarisation of the already polarised light passing through it, the light will no longer be completely crossed with the second polariser and some will pass through. The intensity of this light leakage will be dependent on the induced polarisation of the birefringent material by equation 2.40. The resultant image will be a set of constant intensity contours, the isoclinics and isochromatics (depending on their source).

These polariscopes have then been used to analyse the stress fields under sliding elastic objects. A common arrangement is to have a sliding block, and photoelastic surface, and image the surface perpendicular to the direction of motion [23]. This then allows a 2D slice of the stress fields under the sliding object to be imaged, although the object obviously has to be symmetric in this axis in order to have a consistent cross section to image. This arrangement is illustrated in 2.7.

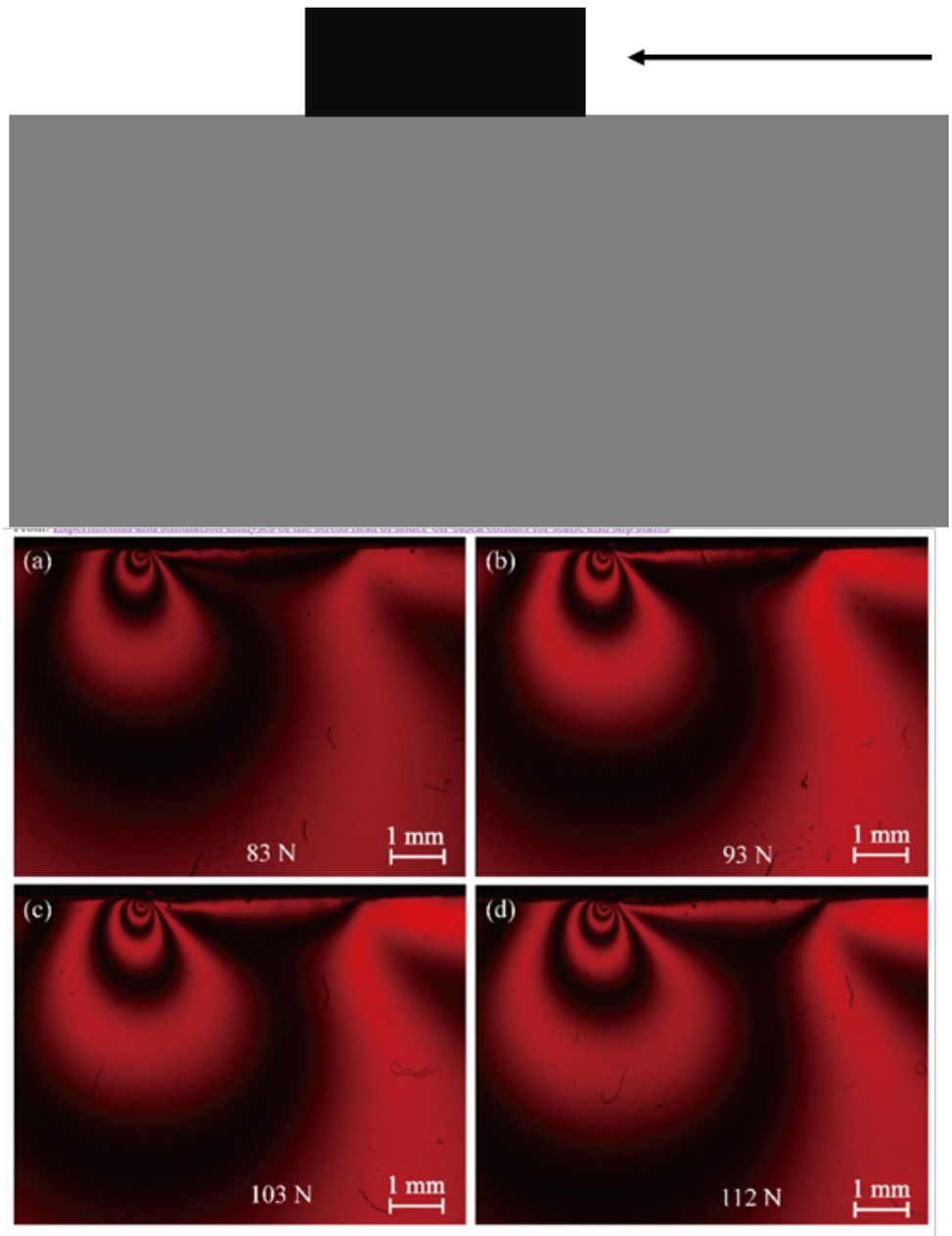

Figure 2.7: An example of the standard photoelastic stress analysis setup under sliding objects, as viewed through a polariscope. A phtotoelastic plane (grey) is viewed side on, while a symmetric object (black), is pressed into contact and moved in the direction of the arrow. This orientation is chosen due to the requirement of the two polarisers and birefringent material all having to be in sight of each other and the camera. The light source is therefore out of view, behind the camera. The strain fields imaged in this case are a cross section of an object that must be uniform into the page. These still provide valuable information about where the strain is focused under these shapes of object, as the experimental image taken from [23] shows. Contours of constant stress are shown, with the highest stress concentrated at the front of the sliding object, as a "leading edge" effect causes buckling in the surface.

Although this arrangements limits the analysis to one fixed orientation, there have been numerous studies of the tribology of elastic objects which use it [23], [26], [30]. These experiments have concluded that the elasticity also plays an important role in the friction and wearing of the surfaces. Photoelastic images

like those in figure 2.7 show that the regions of highest surface stress are at the front of the sliding interface. Simulations predict that this is caused by a "leading edge" effect.

Simulated analysis of sliding elastic blocks has shown that the strain of sliding causes the leading edge of the block to buckle and curl over, changing the physical contact area and the strain distribution at the interface between the contacting bodies. An example of this is shown in figure 2.8.

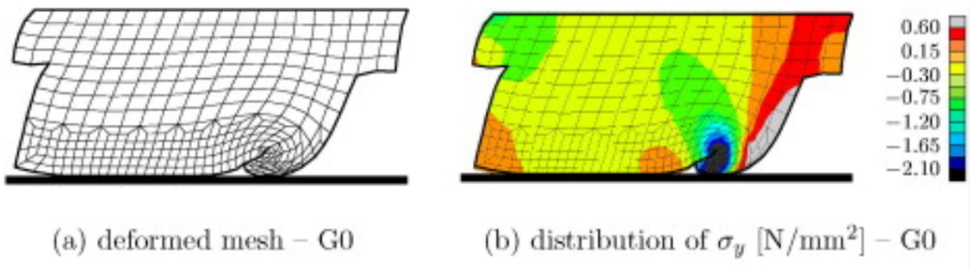

Figure 2.8: A simulation of an elastic block sliding against a ridged half space, made by Hofstetter et al [30]. In a), the shape of the deformed object, due to a shearing force acting left to right, is shown. In b), the distribution of stress is shown. It can be seen that the curling of the interface gives a build up of stress at the front of the interface, termed a leading edge effect. In particularly soft materials, this curling effect causes distinctly shaped wear patterns on the sides of the object.

This leading edge effect has been supported by experimental observations of the distribution of wear patterns on physical objects. These have been qualitative observations of where the highest points of wear are on a contacting elastic object. The distinctive buckling should lead to a distinctive tail-like wear pattern at the front of the sliding object, which has been observed experimentally [30]. However, this is as far as this analysis has progressed thus far.

It has also been noted that the apparent width of the leading edge changes the measured coefficient of friction [26]. This is notable as it shows a shape dependence on the frictional forces, which is not classically the case. Although, to the author's knowledge, there has yet to be any further attempt to physically quantify the effect on the overall coefficient of friction or the distribution of shear at the interface. Nor has the influence of more complex shapes on the leading edge been studied, which is not possible because of the required experimental geometry.

The fact that this setup can only image a single cross section of an object with symmetry perpendicular to the imaging plane, with one dimensional motion along the imaging plane, has naturally driven attempts to change the imaging axis. Ideally, the photoelastic stress pattern would be imaged perpendicular to the contact axis. This would allow two dimensions of the interface to be imaged, and greatly increase the available studies.

A setup which begins to realise this desire to observe stress patterns perpendicular to the contact axis was built by Driscoll et al [31]. This kind of altered setup has had more success in imaging the stresses under the entire 2D plane of a contacting object, and has been applied to cleated shoes [31]. This was achieved by adding mirrors and a mirrored coating to the surface of the photoelastic layer, so that the polarised light would be reflected back to the camera. Although a useful first step in analysing stress fields in this orientation, the additional layers between the contacting interface and complexity of the stress contours meant only estimates of the stress distributions between the shoe and birefringent layer could be calculated from the photoelastic stress contours, and not in real time. This setup, and an example of the images it produced, are shown in figure 2.9.

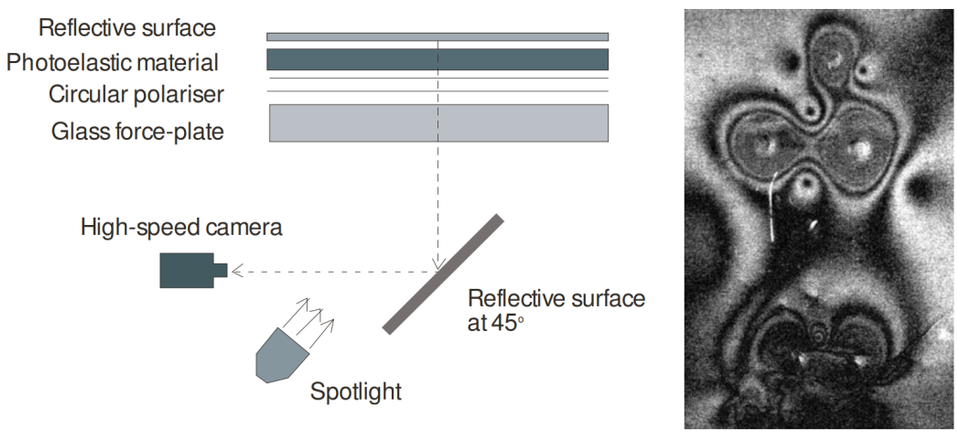

Figure 2.9: The setup and an example of the isochromatic photoelastic contour images produced from a pair of cleated shoes used in [31]. The polariscope setup can be seen to only use one polariser, because the light is reflected and passing through it twice. The reflection adds a π phase change, so light will only pass through the second time if a further phase change is introduced by the photoelastic layer. The photoelastic contours in the example image are induced by contact forces only, and would have to be calibrated away in order to extract the in-plane strain.

2.6 The Greenwood model and other advanced models of friction

It was previously mentioned that more advanced models of the frictional interaction between surfaces exist, than the simple assumption that contact area is proportional to load, and these are worth looking at separately. Although none fully explain macroscopic frictional effects in all materials, they provide more accuracy in their specific applications than the case explained previously.

An early detailed attempt to more accurately model a rough surface was realized in 1966 by Greenwood and Williamson [32]. Their argument was that the two contacting bodies could be modelled by an infinitely flat plane, and a single rough plane. Like simpler models, the rough plane is modelled as a series of hemispheres, with a constant radius of curvature β. Further, the asperities are considered far enough apart that they cannot interact with each other, and there is no interaction with the bulk of the object below the asperities. The difference from the simpler assumption of hemispherical asperities previously mentioned is that each hemisphere is positioned at a different height, and so is deformed by different amounts as the surfaces are pressed together. These heights vary according to a Gaussian probability distribution:

$$\phi(z) = \frac{1}{\sqrt{2\pi}} \frac{1}{\sigma_s} e^{-z^2/(2\sigma_s^2)}. \tag{2.41}$$

Here, σ_s is the standard deviation of the asperity heights z. If the two surfaces are pressed together, such that they are separated by some distance d, then the probability an asperity will contact the second surface will be

$$P(z > d) = \int_d^\infty \phi(z) dz. \tag{2.42}$$

As the asperities are microscopic, then any macroscopic surface will have a large enough number of asperities (N) such that the number of contacts (n) can be predicted by the probability distribution

$$n = NP = N \int_d^\infty \phi(z) dz. \tag{2.43}$$

According to Hertzian contact theory, the area of contact for a single asperity with a radius of curvature β will be $\pi\beta(z-d)$, and the contact load will be $\frac{4}{3}E\beta^{\frac{1}{2}}(z-d)^{\frac{3}{2}}$ [10], where E is the Young modulus of the asperity. Using these expressions and evaluating it over all contacts gives the Greenwood expression of the total force:

$$F = \frac{2}{3\sqrt{2\pi}}\beta^{\frac{1}{2}}NE\int_{d}^{\infty}(z-d)^{\frac{3}{2}}\phi(z)dz. \tag{2.44}$$

Although commonly accepted and used, various attempts to make this more physically representative of real surfaces have been attempted. These include deterministically modelling the asperity heights [33], or what is known as the 3-point model [34]. In this model, instead of a single hemisphere, asperities are modelled as three interconnected hemispheres. This is an attempt to simulate the jagged peaks present in real asperities, while still being mathematically solvable. Although seemingly a more accurate way to model asperities at first, this model is contentious (even by its own authors [35]), as the number and distribution of asperity curvatures required to model a surface do not match the distribution in measured surfaces. The way these approximations map to a real surface is shown in figure 2.10.

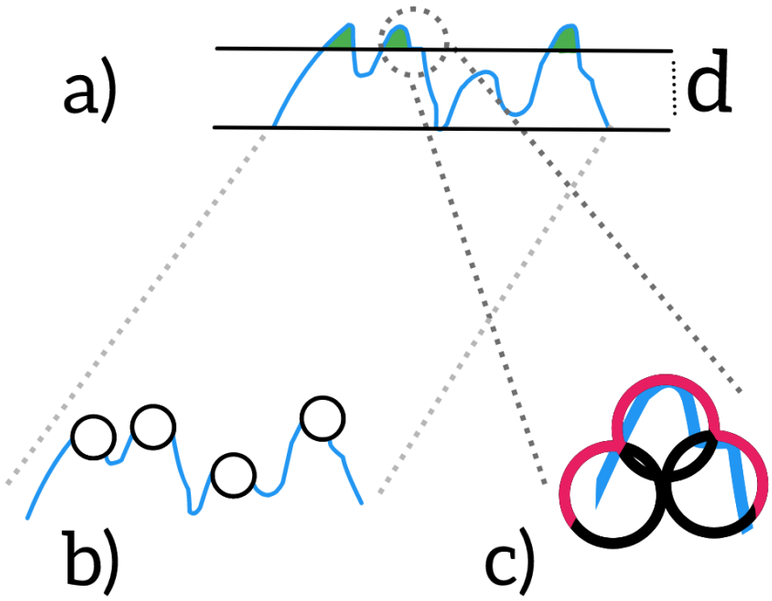

Figure 2.10: An example of how a real interface between a smooth plane and rough surface is approximated in the Greenwood and 3-point models. In a), the rough surface is highlighted in blue, and brought within a distance d to a smooth plane. The areas which deform and form the interface are highlighted in green. In b), the Greenwood model is shown. Each contacting asperity is approximated by a single hemisphere of identical size, but different height. In c) the 3-point model is shown for a single asperity. It is now approximated by three overlapping hemispheres, which more accurately map the asperity profile than a single hemisphere. The combined shape is shown in red. The position at which to centre a hemisphere is chosen based on a material dependant threshold. This threshold is a measure of the separation between the tip of a peak and the bulk of the material.

So far, all of these models have assumed the surfaces never change, however rubbing two surfaces together will eventually cause some form of wearing and the shape of the asperities will have to be adjusted. A common simple correction for this is Archard's wear law [36]:

$$V = \frac{sKF}{H}. \tag{2.45}$$

This law adjusts the volume V of the asperities based on the distance the interface has slid s, the hardness H of the softest material (the only one assumed to wear), a wear coefficient K, and the normal force F [37], [38]. However, again, other models have been proposed that both compete with this [36], [39], or capture different regimes. For example, this model can begin to break down at speeds above a few hundred to a few thousand metres per second [40] or below $1\,\mathrm{m\,s^{-1}}$[26], depending on the material .

It is therefore easy to see that there is plenty remaining to study in the field of

friction, and why it would be desirable to gain a more detailed experimental understanding of what physics is involved.

Bibliography

[1] C. Majidi, R. F. Shepherd, R. K. Kramer, G. M. Whitesides, and R. J. Wood, "Influence of surface traction on soft robot undulation," *The International journal of robotics research*, vol. 32, 2013.

[2] T. Nishimura, K. Shimizu, S. Nojiri, *et al.*, "Soft robotic hand with finger-bending/friction-reduction switching mechanism through 1-degree-of-freedom flow control," *IEEE Robotics and Automation Letters*, vol. 7, 2022. DOI: 10.1109/LRA.2022.3157964.

[3] R. Garcıa and R. Pérez, "Dynamic atomic force microscopy methods," *Surface Science Reports*, vol. 47, 2002. DOI: https://doi.org/10.1016/S0167-5729(02)00077-8.

[4] M. E. Fernando, R. G. Crowther, P. A. Lazzarini, *et al.*, "Plantar pressures are elevated in people with longstanding diabetes-related foot ulcers during follow-up," *PLOS ONE*, vol. 12, 2017. DOI: 10.1371/journal.pone.0181916.

[5] M. A. Feger, J. M. Hart, S. Saliba, M. F. Abel, and J. Hertel, "Gait training for chronic ankle instability improves neuromechanics during walking," *Journal of Orthopaedic Research*, vol. 36, 2018. DOI: https://doi.org/10.1002/jor.23639.

[6] K. Nakajima, E. Anzai, Y. Iwakami, S. Ino, K. Yamashita, and Y. Ohta, "Measuring gait pattern in elderly individuals by using a plantar pressure measurement device," vol. 22, 2014.

[7] A. E. H. (E. H. Love, *A treatise on the mathematical theory of elasticity*, 4th rev., enlarged ed. Dover, 1944, ISBN: 0486601749.

[8] 1. Johnson K. L. (Kenneth Langstreth), *Contact mechanics [electronic resource] / K.L. Johnson.* eng. Cambridge, 1985, ISBN: 9781615832187.

[9] S. Timoshenko, *Theory of elasticity*, 3rd ed. McGraw-Hill, 1970, ISBN: 0070647208.

[10] A. C. Fischer-Cripps, *Introduction to Contact Mechanics*, Second Edition. Springer, 2007, ISBN: 978-0-387-68187-0.

[11] *COMSOL Multiphysics Cyclopedia*, Ninth Edition. COMSOL, 2017.

[12] M. Ostaszewski, J. Pauk, J. Eberhardsteiner, and K. Lesniewski, "A portable plantar pressure system: Specifications, design, and preliminary results," *Technology and Health Care*, vol. 28, 2020. DOI: 10.3233/THC-208001.

[13] J. S. Sharp, S. F. Poole, and B. W. Kleiman, "Optical Measurement of Contact Forces Using Frustrated Total InternalReflection," *PHYSICAL REVIEW APPLIED*, vol. 10, 2018. DOI: 0.1103/PhysRevApplied.10.034051.

[14] C. G. Tompkins and J. S. Sharp, "Dual optical force plate for time resolved measurement of forces and pressure distributions beneath shoes and feet," *Scientific reports*, vol. 9, 2019. DOI: 10.1038/s41598-019-45287-9.

[15] E. Hecht, *Optics*, 5th Edition. Harlow : Pearson Education, 2017, ISBN: 9781292096933.

[16] T. B. A. Senior and J. L. Volakis, *Approximate Boundary Conditions in Electromagnetics*, Ninth Edition. The Institution of Electrical Engineers, 1995, ISBN: 0-85296-849-3.

[17] H. J. M. Brockbank R. and B. R., "Contact force distribution beneath a three-dimensional granular pile," *Journal de Physique II*, vol. 7, 1997. DOI: 10.1051/jp2:1997200.

[18] T. Duckworth, A. J. Boulton, R. P. Betts, C. I. Franks, and J. D. Ward, "Plantar pressure measurements and the prevention of ulceration in the diabetic foot," *Journal of bone and joint surgery. British volume*, vol. 67, 1985.

[19] K.-S. Shih, S.-Y. Jhou, W.-C. Hsu, *et al.*, "A biomechanical investigation of athletic footwear traction performance: Integration of gait analysis with computational simulation," *Applied Sciences*, vol. 10, 2020. DOI: 10.3390/app10051672.

[20] S. N. Srihari and Y. Tang, "Computational methods for the analysis of footwear impression evidence," in *Computational Intelligence in Digital Forensics: Forensic Investigation and Applications*. Springer International Publishing, 2014, vol. 555. DOI: 10.1007/978-3-319-05885-6_15.

[21] T. Edeskär, "Technical and environmental properties of tyre shreds focusing on ground engineering applications," 2004.

[22] G. Amontons, *Hist. Acad. R. Sci.*, 1699.

[23] V. C. Hoang, W. Zhan, Y. Fang, and P. Huang, "Experimental and simulation analyses of the stress field of slider-on-block contact for static and slip states," *SN Applied Sciences*, vol. 2, 2020.

[24] P. Fino and T. E. Lockhart, "Required coefficient of friction during turning at self-selected slow, normal, and fast walking speeds," *Journal of biomechanics*, vol. 47, 2014.

[25] P. Papagiannis, P. Azariadis, and P. Papanikos, "Evaluation and optimization of footwear comfort parameters using finite element analysis and a discrete optimization algorithm," *IOP Conference Series: Materials Science and Engineering*, vol. 254, 2017. DOI: 10.1088/1757-899X/254/16/162010.

[26] J. Hale, R. Lewis, and M. J. Carré, "Rubber friction and the effect of shape," *Tribology International*, vol. 141, 2020. DOI: https://doi.org/10.1016/j.triboint.2019.105911.

[27] K. Ramesh and G. Lewis, "Digital photoelasticity: Advanced techniques and applications," *Applied Mechanics Reviews*, vol. 55, 2002, ISSN: 00036900.

[28] S. Ishihara and M. Mizusaki, "Alignment control technology of liquid crystal molecules," *Journal of the Society for Information Display*, vol. 28, 2020.

[29] C. C. Ibeh, *Thermoplastic Materials: Properties, Manufacturing Methods, and Applications*, Ninth Edition. CRC Press, 2011, ISBN: 978-1-4200-9383-4.

[30] K. Hofstetter, C. Grohs, J. Eberhardsteiner, and H. Mang, "Sliding behaviour of simplified tire tread patterns investigated by means of fem," *Computers Structures*, vol. 84, 2006. DOI: https://doi.org/10.1016/j.compstruc.2006.01.010.

[31] H. Driscoll, H. Koerger, T. Senior, and S. Haake, "The use of photoelasticity to identify surface shear stresses during running," *Procedia Engineering*, vol. 2, 2010. DOI: https://doi.org/10.1016/j.proeng.2010.04.109.

[32] J. A. Greenwood and J. B. P. Williamson, "Contact of nominally flat surfaces," *Proceedings of the Royal Society of London. Series A, Mathematical and Physical Sciences*, vol. 295, 1966.

[33] I. Faraon, "Mixed lubricated line conacts. phd thesis," *University of Twente*, 2005.

[34] A. K. Waghmare and P. Sahoo, "A study of elastic-plastic contact of rough surfaces using n-point asperity model," *Procedia Materials Science*, 2014. DOI: https://doi.org/10.1016/j.mspro.2014.07.361.

[35] J. Greenwood and J. J. Wu, "Surface roughness and contact: An apology," eng, *Meccanica (Milan)*, vol. 36, 2002.

[36] S. Andersson, A. Söderberg, and U. Olofsson, "A random wear model for the interaction between a rough and a smooth surface," *Wear*, vol. 264, 2008. DOI: https://doi.org/10.1016/j.wear.2006.12.075.

[37] J. Archard, "Wear theory and mechanisms," *Wear Control Handbook, ASME*, 1980.

[38] R. Holm, "Electric contacts," *Almqvist Wiksells Boktryckeri AB*, 1946.

[39] S. Andersson and B. Eriksson, "Prediction of the sliding wear of spur gears," *Proceedings of Nordtrib '90, Hirtshals, Denmark*, 1990.

[40] S. Eder, P. Grützmacher, M. Rodríguez Ripoll, C. Gachot, and D. Dini, "Does speed kill or make friction better?—designing materials for high velocity sliding," *Applied Materials Today*, vol. 29, 2022. DOI: https://doi.org/10.1016/j.apmt.2022.101588.

Chapter 3

Experimental methods

There are numerous methods that must be detailed here, but they can be categorised into four main experiments: The design and use of a contact imaging platform that was used to image the contact forces under shoes and feet; a photoelastic platform that was designed to image the in-plane traction forces under the same situations (which was not applied); a prototype traction platform which used a matrix of dye-doped dots to measure the traction distribution under various rotated and translated objects; and finally a dual contact-traction imaging platform, which was a more refined version of the first and third devices. The initial device was the contact imaging platform.

3.1 Contact Platform Design

The key component of the contact imaging device was a pair of FTIR imaging waveguides, which consisted of sheets of 600 mm×300 mm×25 mm perspex with strips of red (632 nm emission peak) LEDs wrapped around their perimeter. A thin layer of two-part Sylgard-184 PDMS was cast on top of these waveguides to protect them from scratches and general wear. This was achieved by manually levelling them and pouring the mixed (but uncured) silicone on top, in a mix ratio of 1:10 monomer to cross-linker [1]. The liquid spread over the surface of the waveguide and resulted in a thin ($\leq$0.1 mm) protective layer that could be peeled away and replaced if needed. This was covered with a protective box, to eliminate dust/debris, allowed to cure at ambient temperature and pressure, over 48 hours. The resulting waveguides were held in place by an aluminium sheath, which also acted to mask and reflect the emitted LED light, so that only light emitted at angles that met the internal reflection condition

($\theta_c \sim 43°$ [2]) could propagate through the waveguide and reach the camera. The waveguides were allowed to move freely and mounted in a raised platform that allowed easy and safe access by participants. Each waveguide rested on a set of four load cells (one positioned at each corner), arranged in a Wheatstone Bridge, which measured the total load under each platform. The outputs from these were amplified and fed into the analogue input channels of a National Instruments USB-6008 DAQ. Below the platform was a Basler AC800-510uc USB camera, which simultaneously imaged each waveguide. These images were captured concurrently with the load cell data, using software written in LabVIEW. This setup is shown in figure 3.1.

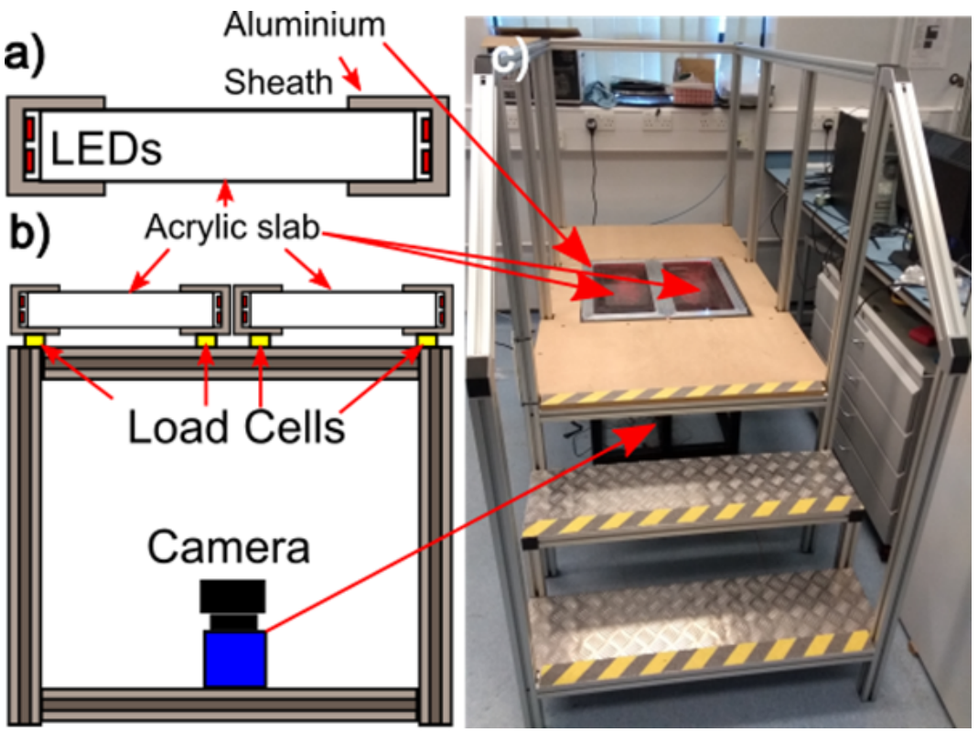

Figure 3.1: A schematic diagram of the contact imaging platform, with a picture of the device included in c). The FTIR waveguides consisted of acrylic slabs wrapped with 632 nm red LEDs and sheathed in aluminium, shown in a). These were mounted on top of calibrated load cells, and set into a raised aluminium platform for the participants' safety. Below the waveguides, a camera was fixed in place, to image the FTIR response. This is shown in b), image from [3].

The red LEDs were chosen simply for convenience: the objects used in the analysis (white/red shoe soles and bare feet) and calibration (red and white dyed silicone) all scattered this wavelength well. Two waveguides were used for two reasons: Firstly, the forces from each waveguide and set of load cells were easily separable, which made it simpler to track the individual loads under each foot of a participant. Secondly, these waveguides needed to withstand large forces (in excess of 3 kN in some cases), so using waveguides with a

smaller surface area meant thinner and lighter sheets of perspex could be used without an increased risk of cracking. A single camera was chosen to simplify acquisition, as it was one fewer device to both include in the physical design and to control concurrently with the remaining hardware. Once the device was assembled, the next step was calibration. There were a number of steps required to calibrate the contact platform. To begin with, the load cells under each platform needed to be calibrated, to convert their voltage into a load measurement. This was accomplished by piling a large number of lead bricks (of known mass) onto each platform and measuring the average voltage acquired by a National Instruments USB-6008 DAQ, using software written in labVIEW. Each platform in the setup was calibrated separately, with the resulting mass-voltage conversions shown in figure 3.2.

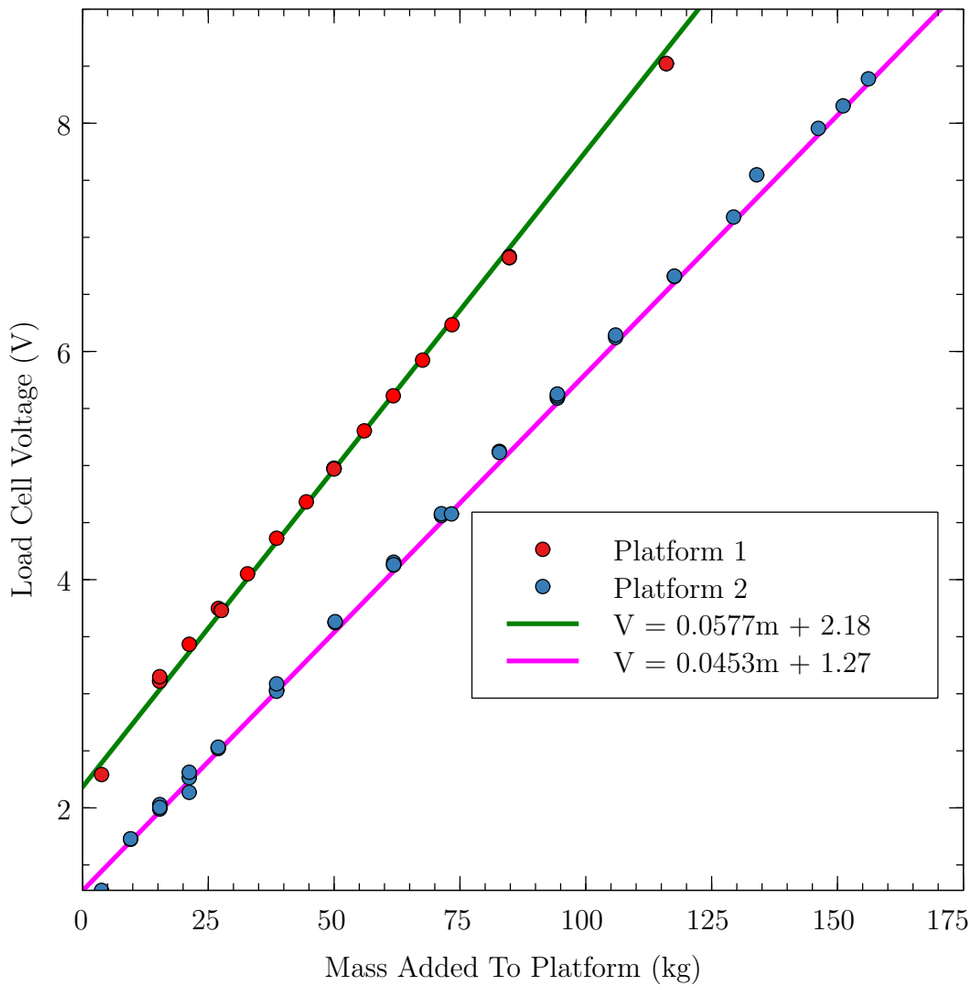

Figure 3.2: The calibration data used to convert the load cell voltages (V) back to the masses (m) placed on top of each contact imaging platform. The data was obtained by loading lead bricks onto each platform and measuring the voltage response using software written in LabVIEW. The green fit and red data correspond to one platform, while the blue data and magenta fit correspond to the second. Errors are too small to plot, measured as $\pm 5\,\mathrm{g}$ on the masses, and $\pm 0.01\,\mathrm{V}$ on the voltages. Each data set is linear over the range of masses, which was chosen to mimic the forces the load cells and the platform would have to experience (up to $\sim 3\,\mathrm{kN}$). This made sure the amplifier circuitry would not saturate at the forces the platform would experience, as well as made sure the platform was structurally sound.

This was a simple linear fit over the range of forces the platform was expected to experience. This meant the load cells were well behaved, and the amplifier circuit was able to convert even the most extreme voltages the platform was expected to experience without saturating. The next component that needed to be calibrated was the waveguide itself.

The intensity of the LED light varied across the waveguide, due to how densely the LEDs were wrapped around the waveguide, and how far a point on the surface was from them. Therefore, this needed to be accounted for, to give a consistent FTIR response. This normalisation was achieved by bringing an

object into intimate contact with the surface, to measure the local intensity response. A liquid with uniform optical properties was initially tested: milk. Even though the fatty particles suspended in the milk fall outside size range [4] of the scatterers (e.g. dye particles) suspended in elastomeric materials, this was determined to be irrelevant in this case. This was because only the relative scattering from one position of the waveguide to the next was important, not the intensity of the scattering itself. As they are within a liquid, these particles are distributed uniformly throughout the milk and provide it with uniform optical properties, while also maintaining conformal contact with the entire waveguide. However, it was found that bringing an object into intimate contact with the entire waveguide introduced interference patterns that were not present when any other method was used. As such, a solid object with a size small enough to assume the variation in scattering under it was negligible was used instead. This object needed to be uniform in colour, be deformable, and could not be noticeably smooth (otherwise there would be no change in microscopic interfacial area as the load was increased). This object was a small cylinder of PDMS (1cm diameter), doped with white silicone dye. The front face of the cylinder was cast in contact with dry 300-grit emery paper, giving it the required surface roughness. As long as the object was pressed uniformly into the surface (ie perfectly normal loading), then the average intensity of back-scattered light under the cylinder as a function of the applied load would follow equation 2.34, with a varying pre-factor β. Again, this would be due to the intensity of the light sources varying with position. Taking multiple measurements at different points on each waveguide gave curves with different scale factors, these could then be normalised to each other, giving the intensity scaling factor at these points of contact. The fit that resulted from this calibration phase is shown in figure 3.3.

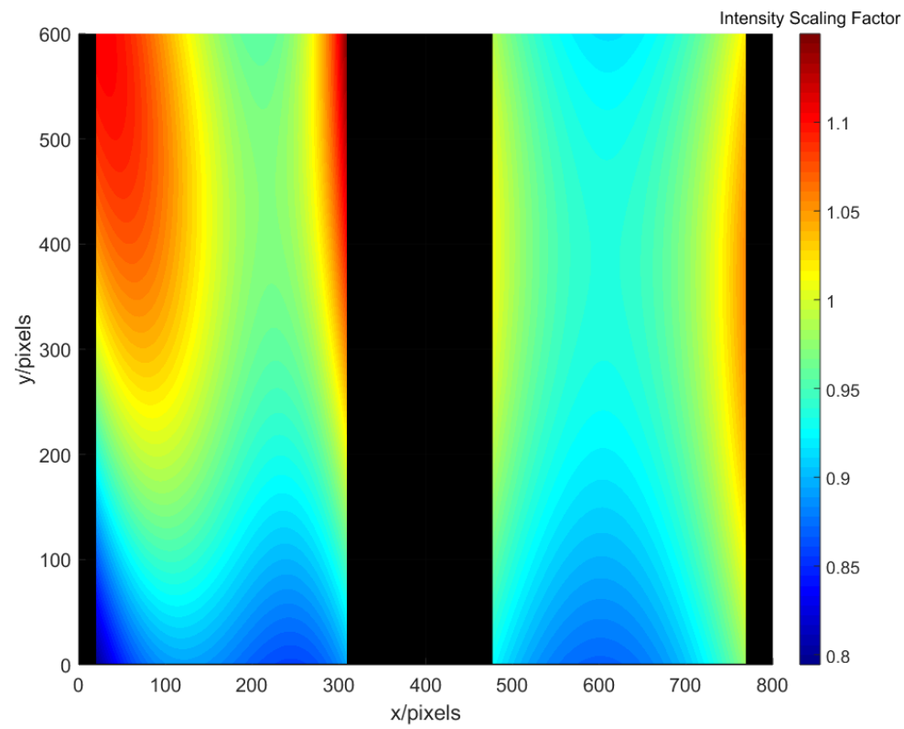

Figure 3.3: The pair of poly 2-2 fits used to scale the LED intensity across the two FTIR waveguides used in the contact imaging device, calculated from a set of sample points taken across both waveguides. Black corresponds to the areas that have been masked, as the camera is viewing the metal mounting brackets holding the waveguides in place. Variations in intensity were primarily due to varying intensity of the light sources, either due to physical differences in the LEDs, or their angle and wrapping density around the waveguide.

It was found that a poly 2-2 fit was required to accurately capture the variation, which is not unexpected as light intensity will decay as distance squared from the source. The black regions of the fit correspond to the intensity scaling factor, highlighted in the legend. The black regions are a mask: the camera was also pointed at the metal frame holding the waveguides in place, and this had to be removed from the images. The background intensity will understandably decrease as the internal reflection condition is broken at points on the waveguide. However, as has already been explained, a rough contacting object has a real contact area much smaller than the apparent contact area (for any reasonable contact load) and it is this contact area which breaks the internal reflection condition. The proportion of scattered vs background light must then also be equally small, and therefore the background can be assumed independent of both the physical size of the contacting object, and the applied load. Now that the light intensity was calibrated, it was possible to find a fit to the intensity-force curves previously used [5]. Again, the form was known to follow equation 2.34 ($F = \beta I^a$), so this was a simple matter of finding factors a and

β. This could be achieved by plotting various (now normalised) intensity-force curves on the same graph and fitting the power law equation. This is shown in figure 3.4.

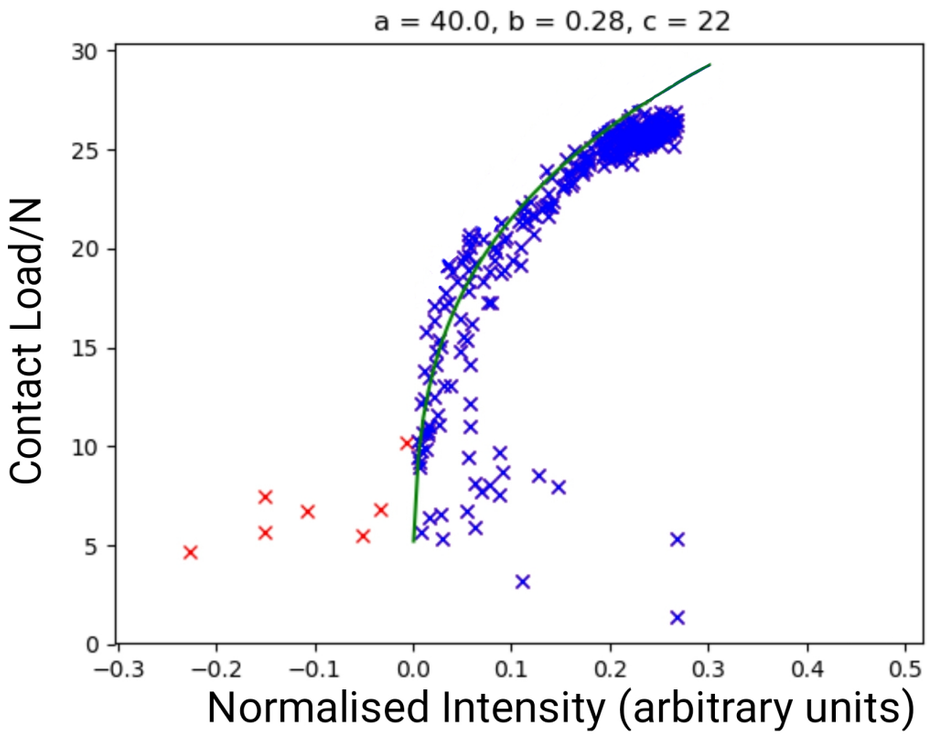

Figure 3.4: A fit of the form $F = aI^b + c$ used to calculate the intensity I and contact force F relationship in the FTIR contact waveguide. These data were collected from the uniform normal loading of a white cylindrical PDMS puck, taken from multiple positions across the waveguides. The intensity had been normalised by the fit in figure 3.3. The offset c is due to the point at which the signal is indistinguishable from background noise. Excluded (red) data are caused by this. Originally there appeared to be two curves of experimental data, which did not properly line up. This is due to there being a slight offset between when the camera began recording and data was captured by the DAQ (the top curve should move down to match the bottom curve), which occurred on every second acquisition. This was corrected for manually in the graph shown here, but later corrected in software. The fit was calculated from the corrected data, but the uncorrected data have been plotted, to illustrate the problem.

The fit was $F = aI^b + c$, with values $a = 40$ N, $b = 0.28$, and $c = 22$ N. The values expected from the theory outlined in section 2.3 would be $a =$ material dependent, $b \approx \frac{1}{3}$, and $c = 0$. The standout factor is the inclusion of c, corresponding to a pixel value offset of 22. This was the limit at which the signal became distinguishable from noise, i.e this was the sensitivity limit of the camera at the exposure time used (5 ms).

Another notable property here is that the experimental results originally

had two apparent sets of curves. This was due to a delay in the software used to capture the camera and DAQ data concurrently. It is likely that a buffer in the camera was not being flushed at the end of every second acquisition, causing a consistent delay time of 2 frames ($\sim$10 ms). This was initially fixed by hand, as was the case with the data presented in figure 3.4. However, a different LabVIEW camera acquisition function was later discovered, which did not have this bug and therefore eliminated the need for manual correction. The final consideration that needed to be made was for the material dependent prefactor. Without some way to account for this, manual re-calibration would be needed for each material or colour used on the platform.

The prefactor in equation 2.34 captures the amount of incident light the contacting material back-scatters, and is therefore colour dependent. This means that the above calibrations only hold for the exact contacting object used in the calibrations, and the prefactor needs to be recalculated for each new contacting object. This was accounted for automatically in code, as the total load cell force (W) under each platform should always equal the sum of all the local intensity forces (F_i). Hence, for each platform the factor β needed to be adjusted by ($\delta\beta$) would be

$$\delta\beta = \frac{\sum_i F_i}{W}. \tag{3.1}$$

It should be noted that this meant the contacting object had to be monochromatic, as there was no provision made for multiple simultaneous values of $\delta\beta$. Otherwise, the exact colour was not important, except for colours/hues that would not back-scatter the red light of the waveguide (ie black). This then allowed various different contacting objects to be analysed.

It was now possible to convert an intensity image to a pressure map, the process of which is outlined in figure 3.5 below. In this figure, a raw image of a foot pressed into the contacting platform is shown. In the next step, the image was decomposed into its separate RGB colour channels. The red channel contained the contact force image, the other channels contained artefacts caused by external light sources. These could be subtracted from the red channel, to give a clean image of the contact patches [5]. Finally, the fit calculated in

figure 3.4 was applied, to convert the image to a pressure map.

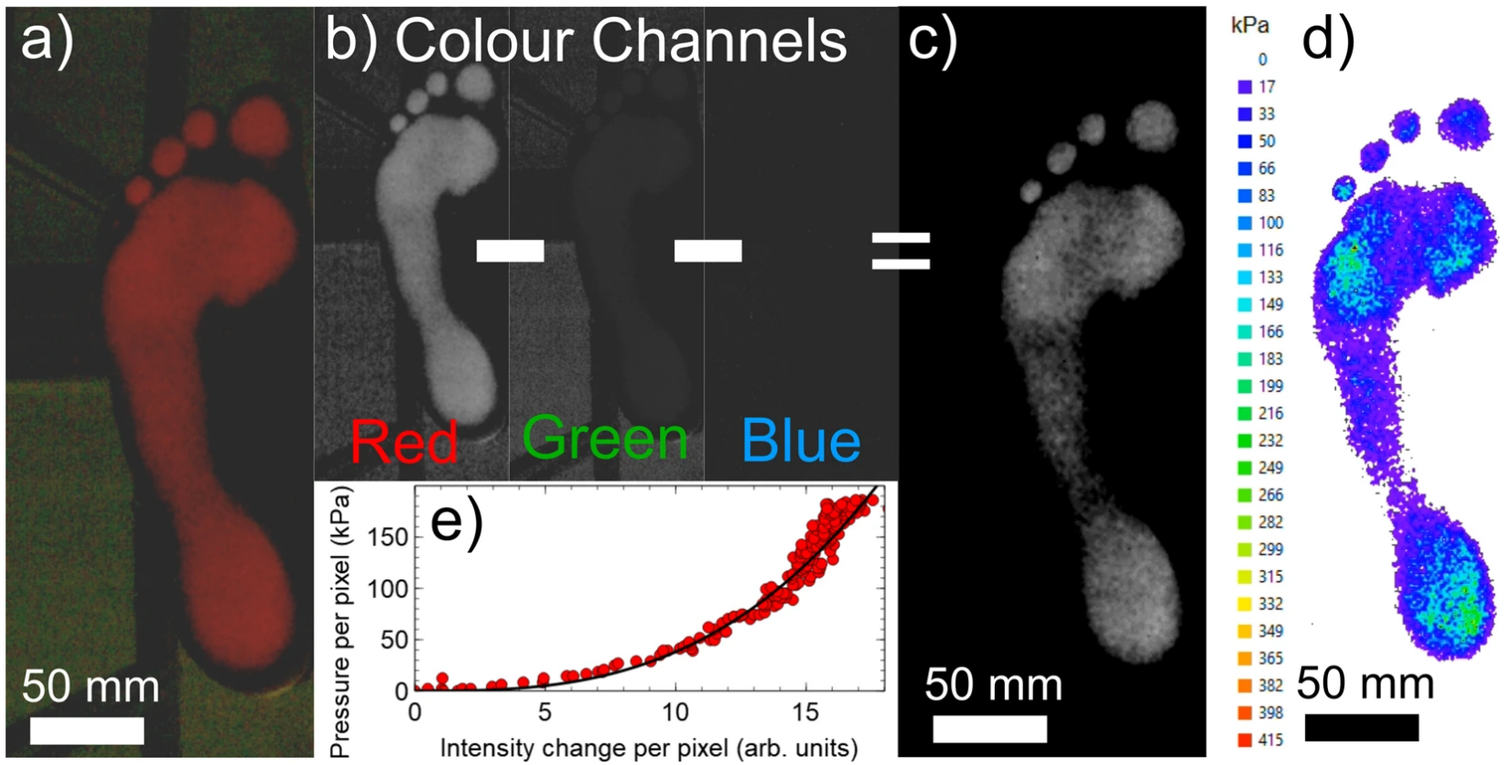

Figure 3.5: An example of the process of converting an image of a soft object, pressed into contact with the contact imaging platform, to a pressure map. The raw image obtained by the camera of a foot is shown in a). In b), the image is decomposed into its separate colour channels. The red channel contains the contact information, while the remaining channels are only background noise. Subtracting these channels from the red channel gives a clear contact image, shown in c). Using the previously calculated fit, the intensity values are converted to pressures, shown in d). An example of the fit, as the axes have now been inverted to convert intensity to pressure, is shown in e). [3]

3.2 Object Design for Traction Imaging

The purpose of the traction force devices was to analyse the shape dependence of friction. As such, various shapes of contacting objects had to be designed. A large number of the use cases (e.g shoes and tyres) for analysing traction load involve soft contacting objects, ie with Young's moduli around (or much less than) that of the contacting surface. Generally, these are of the order 1-10 MPa [6], [7]. However, this was not the arrangement chosen for the contacting pucks used in this work. As the study was in how the traction pattern affects the load distribution, any deformation of the contacting object would be undesirable. As such, a material with a Young's modulus much greater than that of the tread/traction surface was required. To simplify the design process, these pucks were 3D printed, and so the thermoplastic poly(lactic acid) (PLA) was chosen. PLA has a Young's modulus of around 4.1 GPa [8], which is 3 orders of magnitude higher than that of the material used for the contacting layer in the traction device (PDMS - Young's modulus $\sim$1.2 MPa [1], [9]), and can therefore be considered effectively rigid.

Each puck was designed in the 3D modelling software Autodesk 3DS Max, and printed on a Flashforge Finder FDM printer, with a resolution of 0.4 mm in the x and y axes, and 0.12 mm in height. There were multiple variations of the pucks, as the design changed over time. The most commonly used version was a cylinder with 4 arms and an inset on one face, with a tread pattern on the other face. The tread patterned face was placed in contact with the traction platform. The inset allowed a metal rod to be centred on top of the cylinder, providing a uniform contact load by adding weights to the platform shown later in figure 3.17. In larger versions, the "handle" and face with the traction pattern were two pieces, with keyed faces that mated together. This was simply to save the amount of PLA used, and lower the print time. An example of this design is shown in figure 3.6. Multiple kinds of traction patterns were also used. As the intention was to build a device that could fully image the 2D in-plane traction forces, it was natural to choose patterns which would take the most advantage of this. As such, rotational motion was a natural draw.

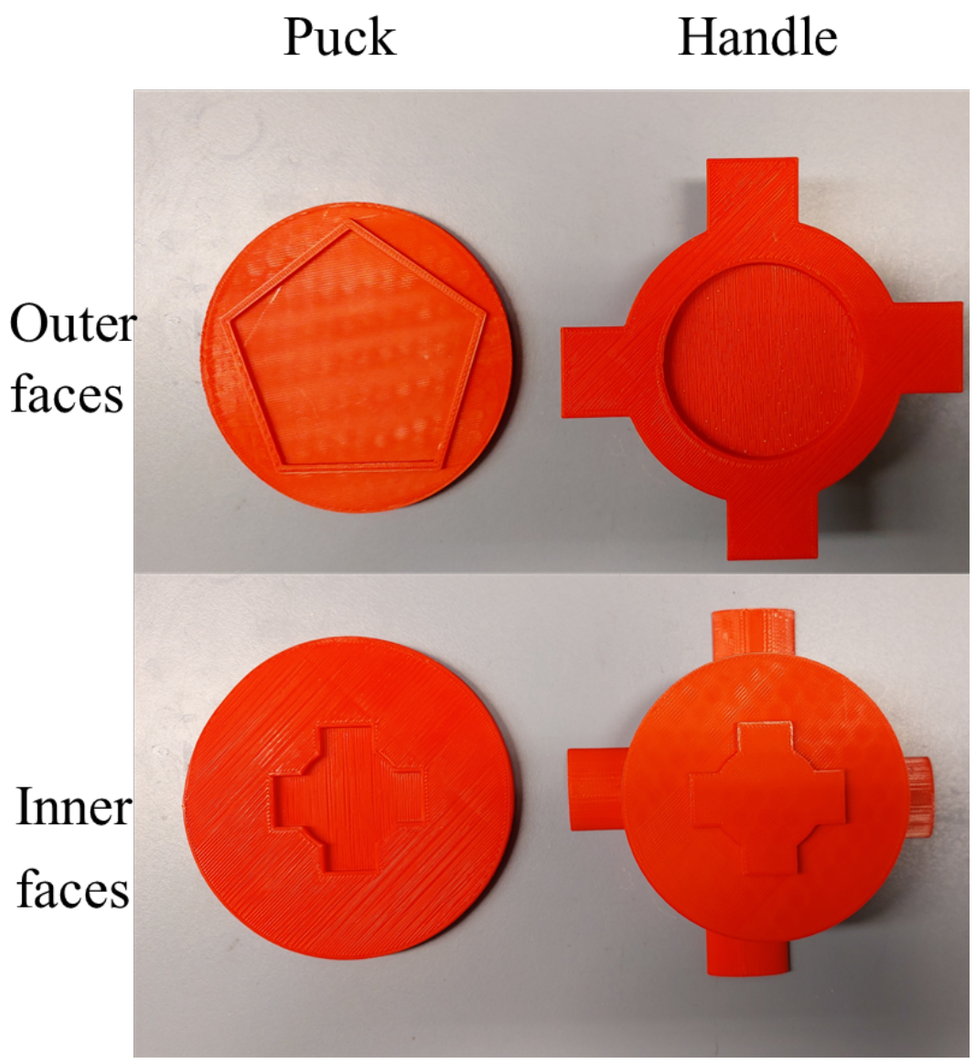

Figure 3.6: An example of the final design of contacting pucks used for rotation and traction measurements. Each puck was 4.5 mm thick and had a raised pattern a further 2 mm thick. The red colour was chosen to take advantage of the lithophane effect in the only remaining colour channel of the camera (red), allowing tracking of the points of contact between the puck and the traction surface. The lithophane effect is where light is passed through a material which attenuates that wavelength, leaving a transmitted signal which varies in intensity with material thickness. A groove around the circumference allowed a steel wire to be looped around the puck, so an evenly distributed translational load could be applied to the puck, without risking the cable slipping. A contact load could be seated in the circular depression on the back, or the keyed handle slotted in place, to allow a rotational load to be evenly applied. The shape and size of the keying allowed for minimal play or warping in the connection points, transferring torque to the puck instead of to deforming the plastic. In this example, red PLA was specifically chosen because of the imaging setup explained later on.

Shoes often have specific patterns positioned at key pressure points which allow a person to freely rotate (for example on the ball of their foot during sport), while still preventing slip [10]. These are generally shaped like hollow regular polygons (polygonal shells) of varying numbers of sides. A set of polygonal pucks was therefore designed, in order to mimic this. Each puck consisted of a

2 mm raised polygon, with a maximum radius of 22.5 mm. The polygon was hollow, with an inner radius of 21.5 mm. The thickness of each shell was chosen to be 8% of the maximum radius, so the shells could be approximated as two-dimensional (within the limits of the traction device), simplifying analysis. Examples of these pucks are given in figure 3.7. Two dimensional motion is not the only interesting arrangement, however. Linear motion is mechanically simpler and its study has already provided insight into various friction features [11], [12], but were limited to objects with a uniform cross section. It was therefore reasonable to conclude that repeating linear motion measurements with varying cross section, would also provide new insight, and this inspired the next set of pucks.

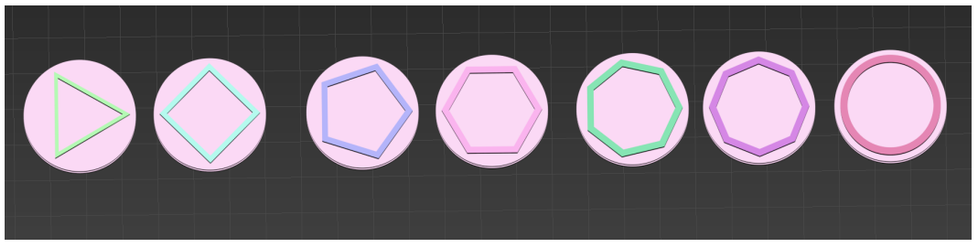

Figure 3.7: All patterns used in rotational measurements. The traction pattern consists of various polygonal shells, with increasing numbers of sides. For the pucks with 22.5 mm radii, the shell thickness was 1 mm and the radius of the polygons were 21 mm. The shell thickness was chosen so that they could be approximated as infinitely thin. For some experiments, explained later on, these pucks were also up-scaled to a 45 mm total radius, with a polygon radius of 42 mm and shell thickness 2 mm, respectively.

As such, the next set of pucks to be designed were based on taking a cuboid with a uniform cross section and bending it to various degrees: a 3 mm thick chevron. These also mimic the various angles of herringbone patterns commonly found on shoes or tyres [6], [10], [13]. It is generally assumed that a 45° angle provides the highest coefficient of friction in elastic materials, but the exact detail is unknown. This is a twofold problem: the research is generally proprietary due to commercial interest, and the geometry is often too complex to determine a clear influencing factor with current imaging methods [11]. As such, the herringbone patterns were kept as their smallest repeating unit (a chevron), rather than attempting more complex geometries at this time. The angle varied between 15° and 90°. Smaller angles were impractical, as the arms began to merge together, and larger angles were simply reversed versions of other pucks. Examples of these pucks are shown in 3.8.

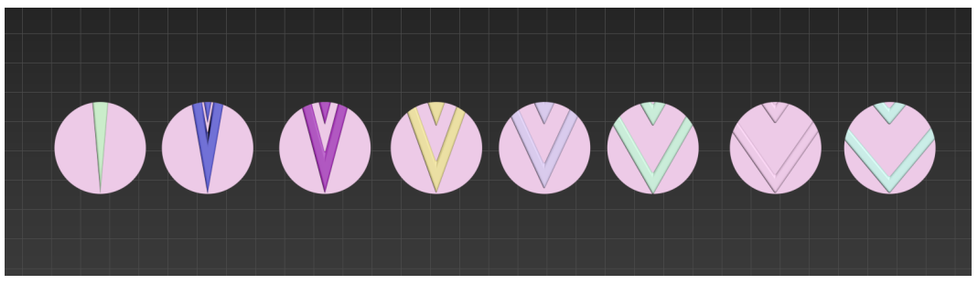

Figure 3.8: The chevron patterns used in translation measurements. Each puck had a radii of 22.5 mm and had two 3 mm thick chevrons, with a peak separation of 40 mm. The angle of each chevron varied between 15° and 90°. Smaller angles were not possible, as the arms of the chevrons began to merge together. Larger angles would effectively be the same as the puck/its motion being reflected along the y-axis, which was an easier way to study these effects.

The third and final pattern was a "digitised" version of the previous pucks, inspired by a set of tread patterns supplied by Adidas. These consisted of a matrix of 1 mm cubic polygons arranged in a 22.5 mm grid pattern, with zero spacing. Each polygon was then stretched in z by a pseudo-random amount between 0-100%, using Max Script in 3DS Max. Only the polygons within the desired chevron shape were kept, using a Boolean operation, resulting in patterns like the example given in figure 3.9.

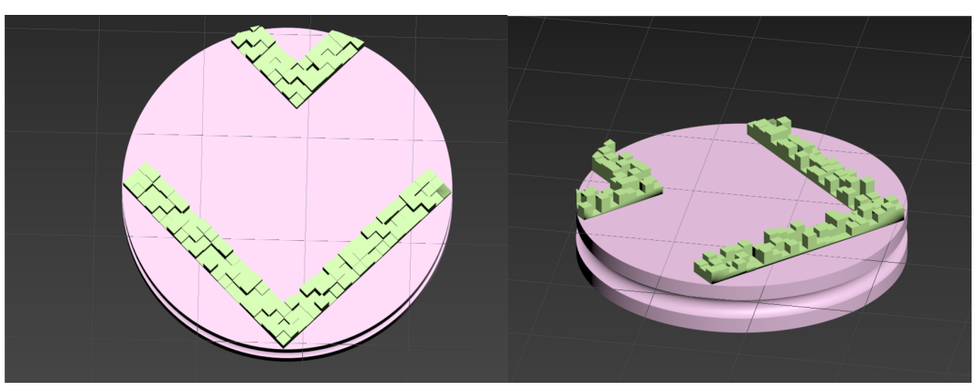

Figure 3.9: The digital chevron pattern used in translation measurements. Each puck had a radii of 22.5 mm and had two 3 mm thick chevrons, and each chevron was made up of 1 mm diameter cubes randomly stretched in the z-axis by varying amounts (between 0-100%). Two angles are shown, to illustrate this variation. These patterns were attempts to simulate near-identical patterns supplied by Adidas.

Having selected a group of objects that would offer insight into the various shape dependence of friction, a device to actually image these local forces needed to be designed. The initial design built on previous work [11], [12], [14] and attempted to use photoelasticity.

3.3 Photoelastic Traction Platform Design

Previous advanced work on measuring the traction forces between a sliding/sheared object and a surface has generally taken advantage of photoelasticity [12], [14], so this was a natural starting point for the analysis done here. The intention was to eventually combine this platform with a contact imaging platform and directly measure both the contact and traction force distributions between an object and a surface (a setup that was achieved with the matrix-based device instead). As such, a number of limitations were present. Mainly, this meant that the waveguide needed to be completely optically transparent, and there could be no layer between the contacting object and waveguide. So a mirrored sheet, like that used in previous work [14] was not feasible. This also limited the positions of the other stages of the polariscope setup to outside of the axis of the waveguide. Ideally, the material thickness also had to be calibrated so that the intensity and strain could be directly correlated - i.e the material was not so thick that a greater than π phase change in equation 2.40 was introduced, which would produce multiple orders of fringes. The setup in figure 3.10 was designed based on these considerations.

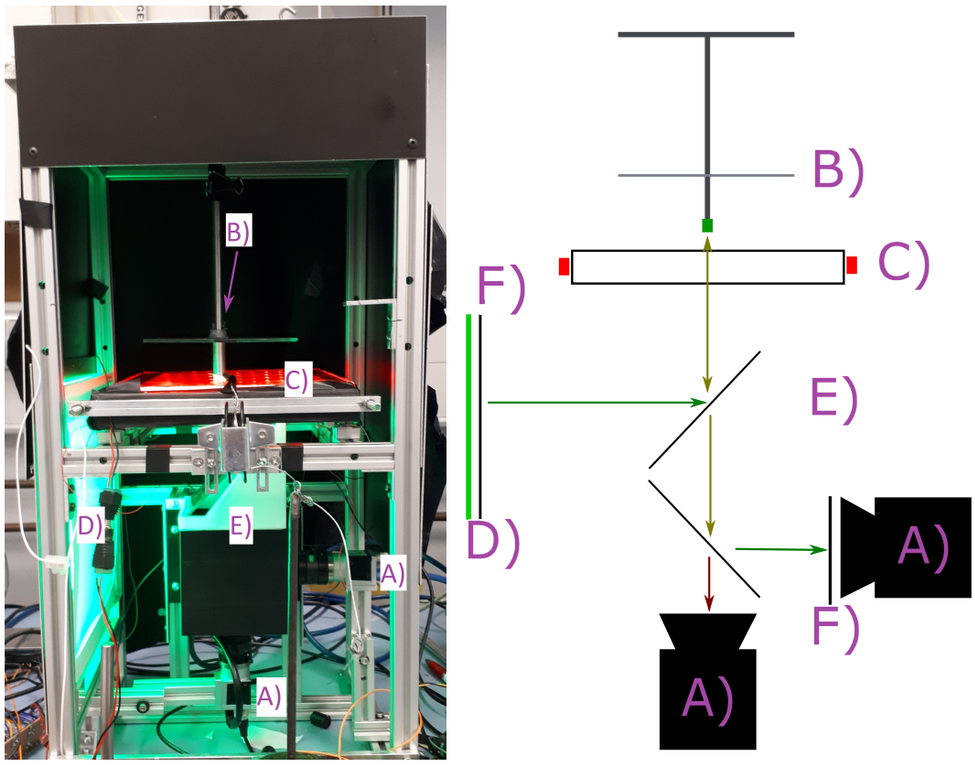

Figure 3.10: The benchtop design of the photoelastic traction imaging device, using a birefringent polariscope setup for traction imaging and designed to eventually include an FTIR contact imaging waveguide. There are two cameras, A), which are positioned such that they receive the same images. Both have colour filters over the lenses, so different colour channels can be separated out (red was intended for contact imaging, and green for photoelastic measurements.). The one intended for photoelastic measurements has a circular polarising filter over it, to form part of a polariscope. The second polariser needed to complete the polariscope is over the uniform light source, D). Light reaches the waveguide C) via beam splitters E), which also allows light to reach both cameras equally. Circular polarisers F) are black lines shown in front of the photoelastic light source and camera. A contacting object could be placed under the weighted platform, B).

In this design, the illumination source and first circular polariser was kept off-axis from the waveguide and the light was reflected into the plane using a 50-50 beam splitter angled at 45°. The back-reflected light, having passed through the birefringent material, would then pass through both beam splitters and reach the cameras. One camera had a circular polariser over it, completing a polariscope, and a colour filter to filter out only the polarised light (green). The second camera had a colour filter over it that would filter out FTIR measurements (red light). Both cameras were manually aligned, so they were viewing identical areas of surface, with an identical orientation, and then bolted in place. The waveguide was a sheet of 310 mm× 220 mm×25 mm acrylic coated with a thin photoelastic layer. The material used was Clear Flex 50 Polyurethane (PU), by Smooth-On. This was mixed in a ratio of 2:1 monomer

solution to cross-linker, and allowed to cure at room temperature and pressure for 5 days, at which point maximum mechanical strength was achieved [15]. Before this, the mixed solution was degassed in a vacuum oven under negative pressure for 15 minutes, in an attempt to remove any dissolved air introduced during mixing, to prevent bubbles.

In order for this setup to work as a traction force sensor, it was necessary to know the phase change that is introduced when the PU layer is strained, and how this varies with thickness. It is also necessary to know this under back reflection, where the light is reflected and then passes through the strained layer a second time. This would introduce an additional phase change of π from the reflection, plus the phase change from passing through the birefringent material a second time. As such, a small rig was built that allowed different samples of polyurethane to be strained and the corresponding optical response measured. This setup is shown in figure 3.11.

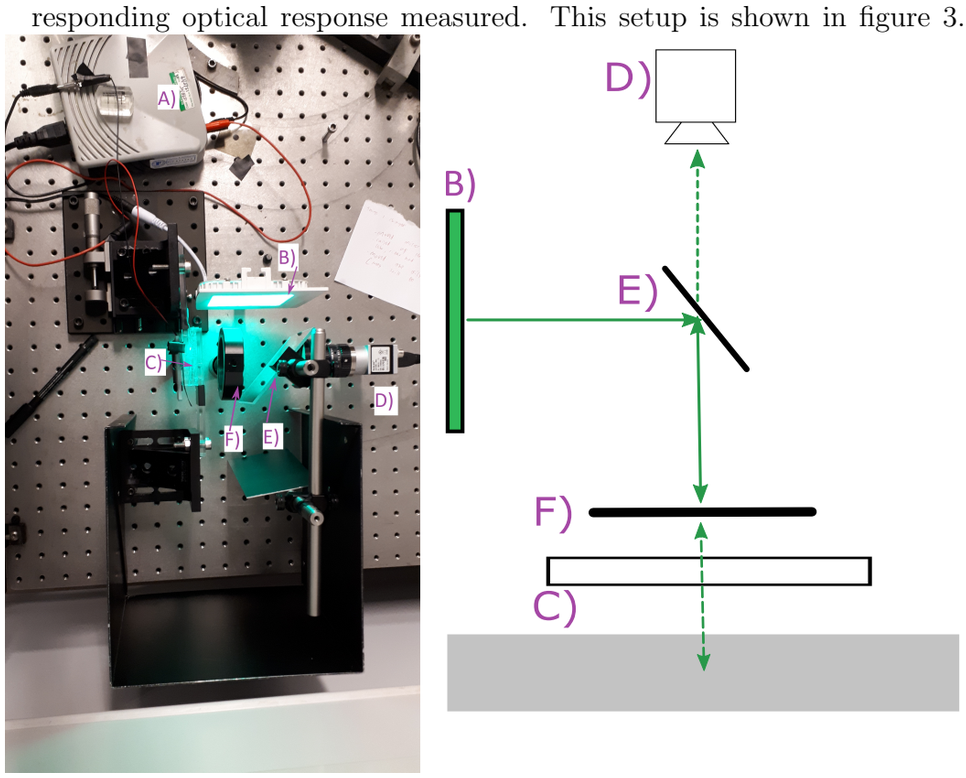

Figure 3.11: The apparatus used to characterise the strain-optic response of Clear flex 50 polyurethane. Light from B) passes through beam splitter E), which is angled at 45° with respect to the light source and camera D). This light then passes through a circular polariser mounted in F) and through the sample, C). The sample is mounted to a translation stage by PMMA slides and backed by a mirror, reflecting the light back through the polariser and to the camera, via the beam splitter. A) is simply a power supply. Various thicknesses of polyurethane samples were bolted between the optical mounts that stretched them. The displacement was then tracked by a small light mounted on the slides.

This mimicked the entire optical path of the device in figure 3.10, but on a smaller scale. Instead of a fixed waveguide, there was a set of mounting brackets to attach and strain various thicknesses of polyurethane. The mounting brackets were attached to a micrometer stage, to allow the sample to be stretched. The strain in the samples caused noticeable backlash and, as such, the micrometer gauge on the pictured translation stage did not provide an accurate measure of strain. Instead, an LED of known size and distance from the camera was also attached to the mounting bracket and this tracked the displacement.

Various thicknesses of polyurethane, between 2 mm and 5 mm, were cast between two sheets of perspex which had mounting holes drilled into them. These were spaced using custom made PTFE spacers, and the polyurethane poured in-between, after being prepared in an identical way to above. An example of the photoelastic images produced when one of these slides was mounted in the strain rig is given in figure 3.12.

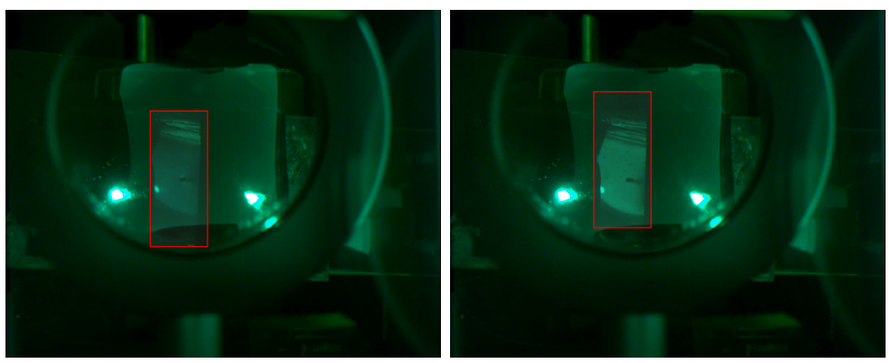

(a) 0% shear strain (b) $20 \pm 1\%$ shear strain

Figure 3.12: Examples of the photoelastic images, at two different strains, used to find the strain-optic relation of polyurethane and determine the appropriate thickness for the traction platform. The red highlighted region indicates the visible region of the sample fully aligned with the circular polarises, light source, and mirror - i.e the region of the complete polariscope path. A section of the sample area was averaged over, to give the mean intensity. The strain was found by tracking the positions of the two green LEDs visible in the bottom left and right corners of the sample. It is noteworthy that the zero applied strain example is not completely dark. This is likely due to stresses in the sample being bolted in place and bowing slightly. Discontinuities in the top of the highlighted region are due to tearing when removing the sample from the mould, and were excluded from the region of interest.

A few important features of this setup must be noted. Firstly, only the region of the image within the red highlight was viewing the complete polariscope path (both circular polarisers and the sample), and a section of this was averaged

over to find the mean intensity within each sample, at a given strain. The strain was found by tracking the relative displacement of the green LEDs mounted in the bottom left and right corners of the sample. The unstrained sample is also not completely dark. This was not the case when the sample was simply held in front of the camera, or when only the mirror was observed. This meant there was no observable intrinsic stress in the mirror, perspex slides, or polyurethane. The likely cause of this was instead a slight mismatch in the thickness of the samples and the gap between the rails they were bolted to, causing the sample to bow imperceptibly and produce a stress. This did not alter the results, as it could be subtracted from the initial state.

There are also some discontinuities in the sample area. Fringe patterns are observable in the top of the highlighted area. This is a region where the polyurethane was torn when removing it from the mould, and was not included in the averaging. Bubbles in the samples did, however, affect the averaging. These were unavoidable as the mould was sealed on all sides, so they could not be manually popped, and there was no way to provide sufficient positive pressure to dissolve them (which is the recommended method [15]). These bubbles therefore decreased the amplitude of the results but, as their volume was minimal, did not alter the strain-optic frequency from equation 2.40 (which was the key value here). The amplitude was naturally unimportant, as this depended on the intensity of the light source, which would be different in the final device. The strain-optic results of various thicknesses are shown in figure 3.13.

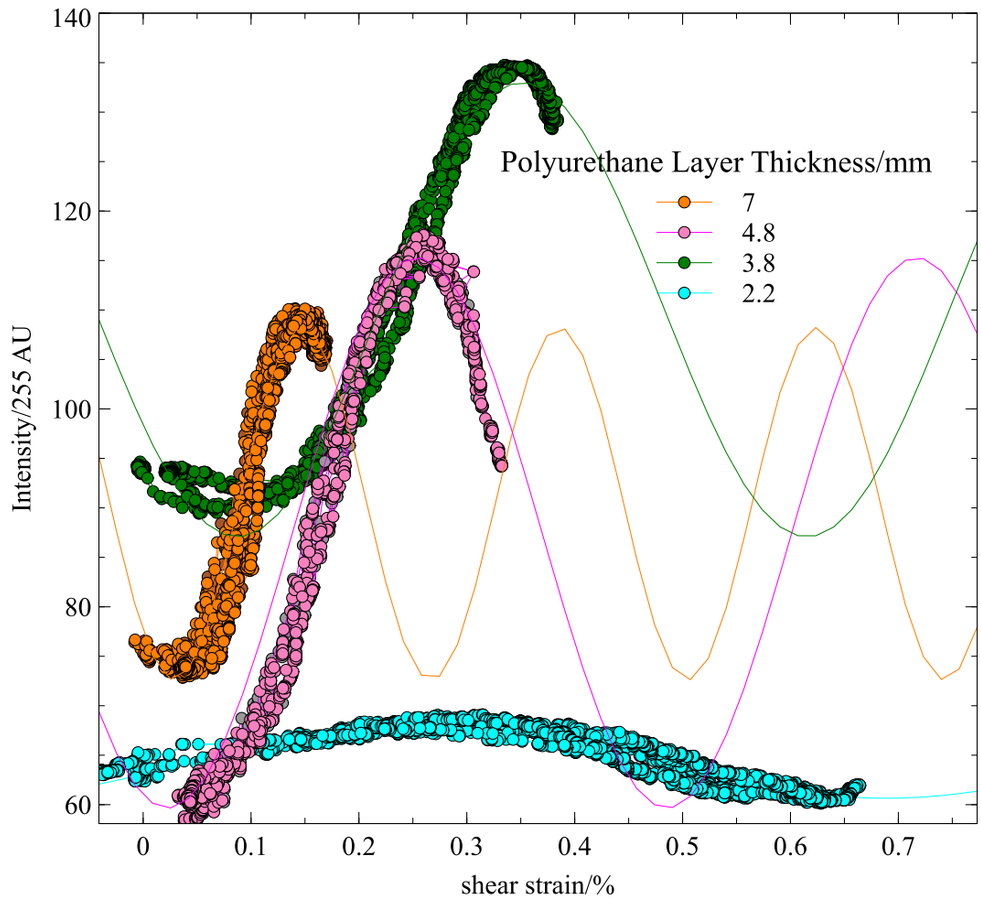

Figure 3.13: The birefringent intensity of various thicknesses of polyurethane samples, as a function of shear strain in the samples. The value of the intensity is arbitrary, as observed by a Basler AC800-510uc USB camera. The frequency of the intensity changes increases with the thickness of the sample, so this can be used to find the ideal thickness for the range of forces expected in the traction platform. Variations in amplitude are independent of this and are instead due to bubbles in the sample region affecting the averaging.

From this, the relation between the thickness of the sample (t) and strain-optic frequency f was found to be $f = 1.9t - 1.4$. Based on the expected range of traction forces experienced while undergoing various activities [16], and the elastic modulus of polyurethane [15], it was determined that a thickness of approximately 3.5 mm would be ideal for the traction platform. After casting, the actual thickness of the polyurethane layer on the traction platform was measured as 3.3 mm±0.1 mm.

It was now possible to complete some basic testing of the photoelastic device, using the setup in figure 3.10. The chosen contacting object was a small (6 mm diameter) cylinder with a flat white face. This was picked for two reasons: Firstly, it mimicked the reflectivity of the objects the device would be used on, so the strain-optic amplitude was similar, which would simplify converting intensities to strains and help determine what modifications would be needed

if the surface reflectivity was low. Secondly, a cylinder was chosen because the strain field caused by a hard cylinder contacting a soft semi-infinite plane is well understood [17], so it would be simple to remove any strain induced by contact pressure. For a cylinder of radius a, with a contact pressure p_m, then the strain fields σ_r can be calculated as a function of the radial distance from the centre of contact r, from equations 2.7 and 2.8:

$$\sigma_r = -\frac{1}{2}(1+2\nu)p_m, \quad r \leq a \tag{3.2}$$

$$\sigma_r = -\frac{1}{2}(1+2\nu)p_m\frac{a^2}{r^2}, \quad r > a. \tag{3.3}$$

When a contact mass of 60 N was applied, with and without a 50 N horizontal load, the fringe patterns in figure 3.14 were produced. Two things are obvious here: Multiple orders of fringes are present outside of the contact area. Although these could be converted back into strains, and then used to attempt to scale the intensities inside the contact area (as the strains must be continuous at the boundary), the multiple fringe orders mean this is non-trivial. It would be programatically complex to identify each fringe order for an arbitrary pattern, and work inwards to the maximum strain value. Secondly, the area under the contact patch is dark. This is sufficiently dark ($(37 \pm 1)/255$ with an exposure time of 10 000 µs) that no detail can be discerned even though the light source is very bright. This adds further complication, as it means unreasonably high exposure times would be necessary to image surfaces which were not specifically designed for the device. On top of the complex image recognition required to identify each fringe contour, this would make the analysis very slow and impossible to do in real-time. It was determined that a second method for measuring strains would be a more viable approach instead. This method was the matrix-based traction platform, which sacrificed resolution for ease of analysis and speed.

It should be noted that, once the results which are expected are well characterised, it would be possible to use machine learning on this kind of setup to produce highly detailed images from contours and contact patches such as these. This was, however, not the avenue of research undertaken here and why the device was abandoned. It would ideally require much more fundamental knowledge of the expected intensity-force response than is currently available

before this was attempted.

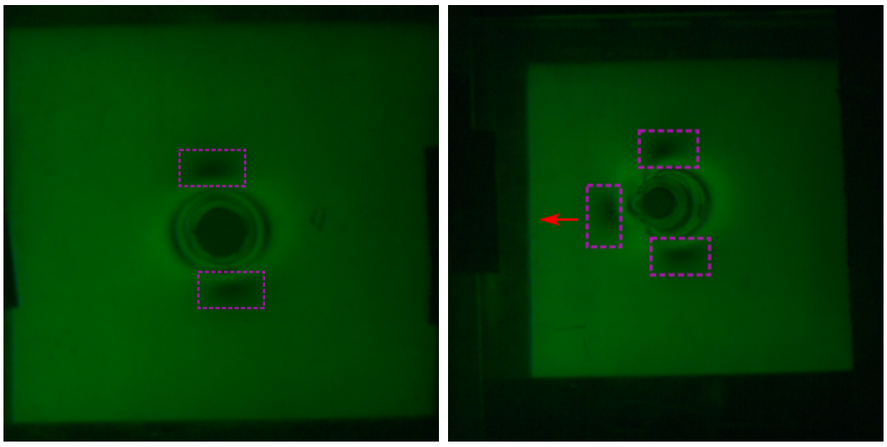

(a) Unstrained (b) Strained

Figure 3.14: An example of the photoelastic fringe patterns produced by vertically and horizontally loading a 6 mm white rubber puck in the photoelastic traction imaging device, viewed from below the contacting plane. In (a) there is a contact load of 60 N and a horizontal load of 0 N. In (b) the contact load is identical at 60 N but there is now a horizontal load of 50 N, applied in the direction of the red arrow. The difference in the fringe patterns is clear. In (b), there is a clear compression of the fringe pattern in front of the puck and an extension behind it. Additional fringes are also present, due to the overall higher levels of strain in the sample. A maximum of three dark lobes (highlighted in magenta) are also present in the images, which also correspond to a compression of the photoelastic fringes along their centre axis. These have been found to be due to a slight polarisation effect of the PMMA. This is likely due to the PMMA being extruded, resulting in a net alignment of the polymer chains [18].

3.4 Matrix-Based Traction Platform Design

The key component of the matrix-based traction platform was a layer of uniformly spaced fluorescent dye doped hemispherical dots, suspended in a layer of elastomer. This matrix of dots allowed the displacement of the elastomer film to be tracked, which could be converted into a map of the local shear. The intention was that the dye doped regions be made of the same elastomer, and doped with a low enough concentration of dye, such that the elastic properties remained constant. Firstly, the desired materials had to be selected.

There were two choices of materials for this elastomer layer, based on what could be easily sourced: The elastomeric materials available were Sylgard 184 PDMS (by Dow) or Clear-Flex 50 polyurethane (by Smooth-On). Polyurethane cured too quickly, and it was not possible to reliably make a large layer without imperfections, due to trapped air created by mixing. This resulted in PDMS

being the material of choice. Further, there was only one fluorescent dye that could be sourced that did not aggregate in PDMS when tested, which therefore dictated what the doped regions were dyed with: Rhodamine-B.

The first step in creating this traction layer was CNC machining a matrix of debosssed hemispherical depressions into a sheet of aluminium to act as a mould. Each dot had a centre-to-centre separation of 2 mm, and a depth of 0.25 mm This was then coated in a mixture of carnauba wax dissolved in chloroform, and the solvent was allowed to evaporate so the remaining wax could act as a mould release. A layer of liquid PDMS doped with 0.8%wt Rhodamine B dye (also dissolved in chloroform) was then poured on top and scraped off, so only the PDMS in the recesses remained. 0.8%wt was chosen as it had been determined this was a safe limit at which the physical properties of the elastomer would be negligibly affected while still maximising fluorescence [1]. This was allowed to cure, and a 2 mm thick layer of transparent PDMS was poured on top and allowed to cure, bonding with the dots. Next, this sheet was removed from the mould and flipped. A thin layer of PDMS, just thick enough to cover the dots, was then poured on top. In the traction-only device, a thin layer of PDMS doped with black silicone dye was also added, as this device did not need to be fully transparent. This black layer helped to block passive light sources (e.g. room lights and computer monitors) and gave the dots a uniform background. All curing steps were undertaken at room temperature and pressure, over 48 hours, to ensure maximum physical strength [1]. This was undertaken in an air-tight box, to prevent contamination from airborne dust/debris. This design process is illustrated in figure 3.15.

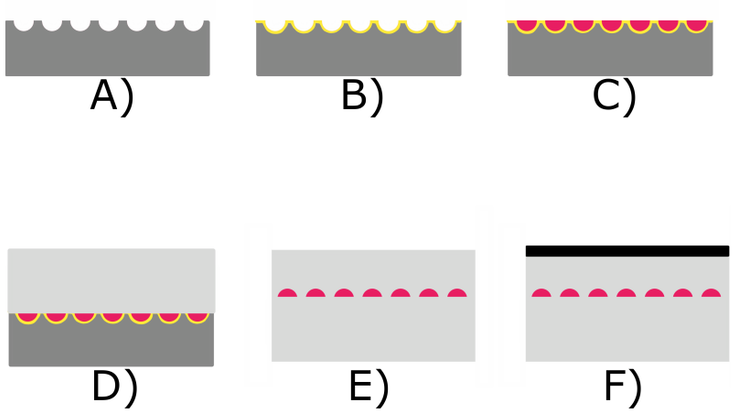

Figure 3.15: An illustration of the steps involved in forming the traction layer. Step A) shows a two-dimensional cross section of the 220 mm×300 mm CNC machined mould used to form the layer, with a fine coating of wax deposited in step B). In step C), Rhodamine-B doped polydimethylsiloxane has been poured over the mould to fill the debossed hemispheres and the excess elastomer scraped away, so that only these regions contain elastomer. After curing, a 2 mm layer of clear PDMS was then placed over the top in D). The sheet was then carefully removed from the mould, and another clear layer added over the top, to seal in the dots, in E). Finally, in F), a thin (<0.1 mm) layer of PDMS doped with black silicone dye was poured over the top, to block passive light sources and give the dots a uniform background for imaging. All curing steps were undertaken at room temperature and pressure, over 48 hours, and sealed in an air-tight box to prevent contamination from dust/debris.

A few additional considerations had to be made when using this layer as a traction sensor. There were multiple different layers of cast PDMS, which may have varying properties, due to variations in preparing each uncured polymer solution. For the most part this would not have mattered, as the layers were stacked vertically, out of plane of the shear, so each in-plane position would act identically and a net Young's modulus could still be calculated. The dots, however, were cast at a different time to their surrounding material, which may lead to regions where the Young's modulus of the layer is discontinuous along the boundary between the dots and surrounding in-plane material. That is to say, the shear of the dots may not match the shear of the surrounding material, for the same load. The mix ratio of the PDMS did not vary more than ±1%. Based on experimental data [9], this would only change the Young's modulus (and hence any linear displacement) by ±0.6%. This is well below the resolution of the imaging device and would not affect the results. Secondly, the dots were hemispherical and not at the exact surface of the waveguide, they were approximately 0.1 mm into the surface, based on the volume of PDMS added on top of them. The point of measured shear was based on the circular profile of the dots at their largest radius, which is a further 0.25 mm into the surface.

This means that the actual values of shear measured are only approximately at the surface (15% into the depth). As the shear should behaved linearly with depth, and the load was directly measured at the surface, then the measured shear modulus will presumably also be linearly scaled from the actual shear modulus. This could not have been avoided with the available equipment, as changing the orientation of the dots so that the largest radial cross section sat at/facing the top of the surface would mean that the second cast layer would not be thick enough to peel the whole sheet out of the mould.

The choice of Rhodamine B as the fluorescent dye obviously also dictated the illumination source for this layer. Rhodamine B has the emission and absorption spectra shown in figure 3.16. The choice of illumination became more complex in the dual traction-contact imaging platform, as interference with the FTIR back-scatter needed to be avoided in order to keep the two signals separable. Looking at the Rhodamine spectra, a clear absorption peak can be seen around 540nm. From a machine vision perspective (where the RGB value of the colour is important) this peak is strongly green, with secondary peaks throughout the bluer end of the spectrum. The emission spectrum peaks around 570nm, which is a yellow digitally represented in the RGB colour space with strong red and green components. Hence, the maximum overall quantum efficiency of the dye could be achieved by illuminating with blue light. This then leaves the blue channel washed out by the light source, so the dye emission can only be clearly seen in the red or green channels.

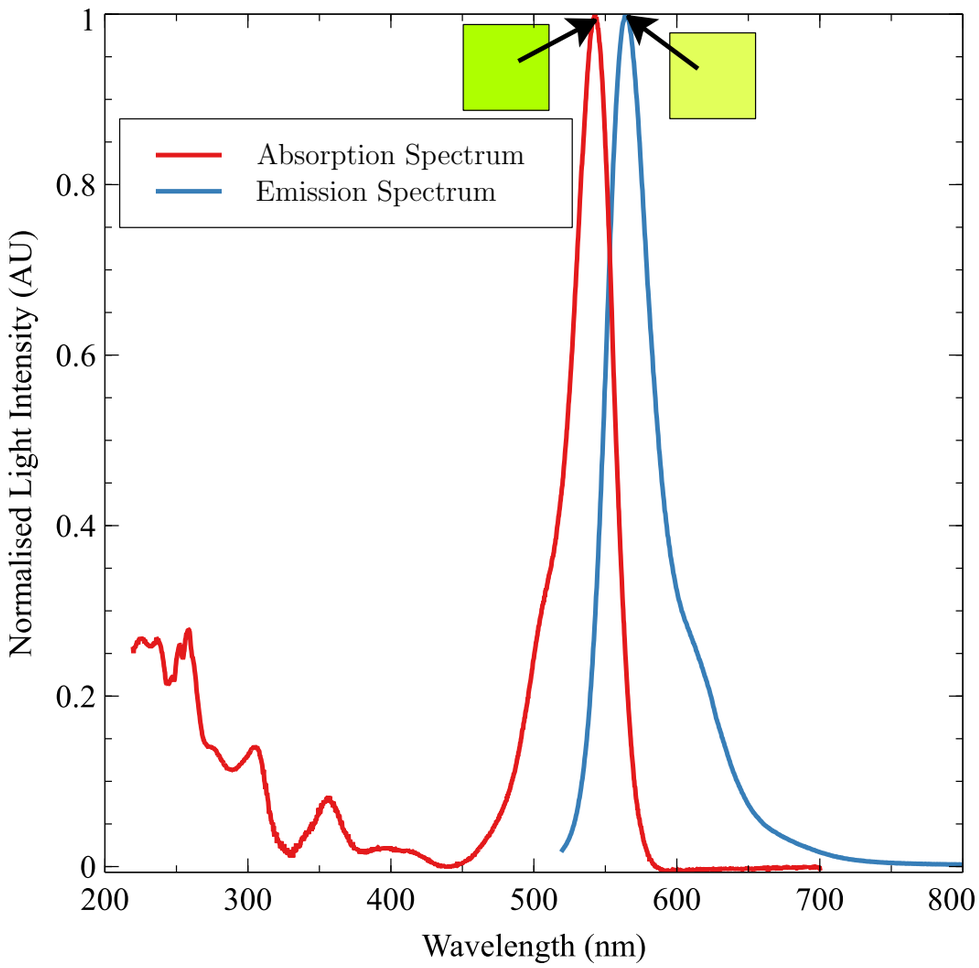

Figure 3.16: The absorption and emission spectra of Rhodamine-B, respectively highlighted in red and blue. The emission peak is centred at 570 nm and the absorption peak at 540 nm. The colour of the light emitted at each peak has been added to the plot. These colours can also be represented in the RGB255 colour format as RGB(174,255,0) and RGB(226,255,90), for emission and absorption respectively. Both spectra fully saturate the green channel of the spectra, and at least partly saturate the red, but the blue channel is only used by the absorption spectra. From a machine vision perspective, this means it is possible to excite the dye with narrow-band blue LED light, and have strong emission in the green channel of the camera. It is also worthy of note here that the quantum yield of the dye drops to effectively zero in the infrared region, at around 800 nm. This makes the dye effectively transparent to infrared light, a property that was necessary for the dual contact-traction device. Data was collected from a solution of Rhodamine B dissolved in ethanol [19].

When building a traction-only device, this was of little consequence. The dye was excited with blue light, around the fluorescence peak, and the broad emission peak could be detected in the green channel of the camera. This layer now needed mounting so that it could have a set of loads applied, and be imaged.

In this device, the traction layer was mounted on a 210 mm×300 mm×25 mm sheet of perspex, which was then wrapped around its circumference with blue

LEDs. These LEDs were held in place with black polymer masking. This essentially made an FTIR waveguide similar to those used for contact imaging, however the waveguiding effect was not used for any direct sensing, but as a way of indirectly giving all of the dots an approximately equal and consistent illumination. The waveguiding provided two distinct advantages to other methods of illumination (like a standard light panel - which was also attempted): namely, it was more compact and needed a lower light intensity. The lack of a large external light panel and beam splitters (as in the arrangement used previously in the photoelastic device) was beneficial and allowed for lower light intensity to be used, for two reasons: Firstly, 75% of the light would be lost to two passes through a 50-50 beam splitter. Secondly, as most of the light was totally internally reflected, a lower intensity of LEDs was needed, as multiple reflection events would eventually lead all (ideal) ray paths to the dye doped regions, instead of just those rays with a direct line of sight to them. The net result was a significantly lower required intensity of light source: $27\,\mathrm{W\,m^{-2}}$ vs $112\,\mathrm{W\,m^{-2}}$.

This waveguide was then clamped along its entire circumference by an aluminium bracket, which was then bolted to a rigid aluminium frame. This served to hold the waveguide in place, with the stiffness being important, as any flexation of the frame would shift the dots and make measurement impossible if they were moved more than $\sim$1 mm. This setup is shown in figure 3.17. Even bolted in place, this was a notable source of error in linear traction measurements. Above this was a solid 20 mm thick steel plate, with a 5mm hole drilled through its centre, this allowed a steel rod, with a small platform on top, to be passed through to the exterior of the device, to place contact loads onto the objects placed on the platform.

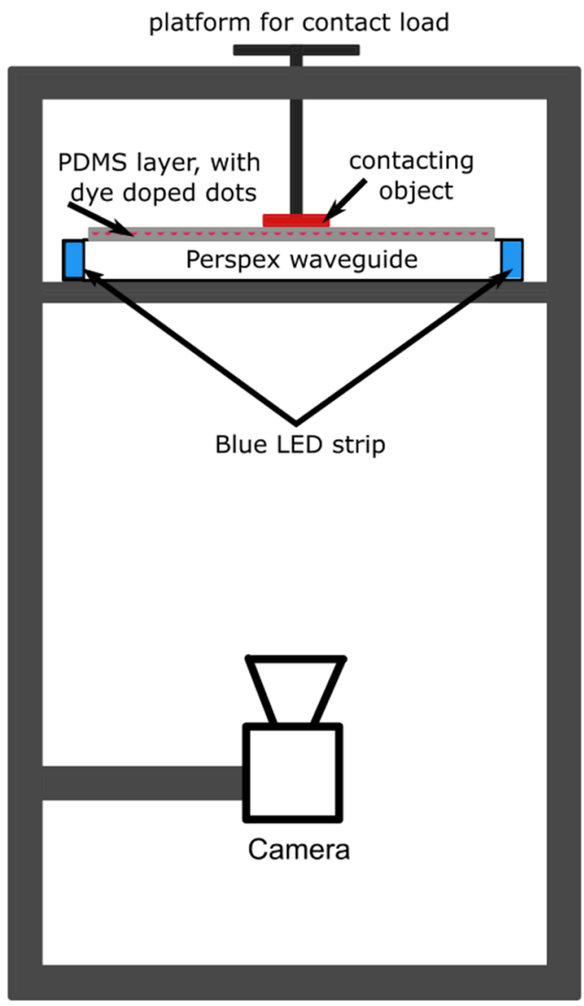

Figure 3.17: A schematic diagram of the experimental setup of the matrix-based traction device. Blue LEDs are wrapped around a Perspex sheet, with a layer of polydimethylsiloxane (PDMS) cast on top, to create a deformable waveguide surface. A uniform grid of Rhodamine B doped dots are suspended within the PDMS, which absorbs the blue light from the LEDs and emits in the green, creating a network of points that track in-plane shear. The displacements from the undeformed state can be used to convert these to local forces. A uniform contact load is provided by adding masses to the platform resting on the contacting object.

One further addition was made, as it was desirable to know where the tread patterns in the puck were in relation to the observed traction map, especially for more complex patterns. Integrating a contact imaging device into the setup would be insufficient, as not all of the patterns made full contact with the surface (for example, the digitised chevrons in chapter 3.2). Instead, the lithophane effect was used. This is where light is passed through a material which attenuates that wavelength, leaving a transmitted signal which varies in intensity with material thickness. The intensity of the light is chosen such that

there is sufficient contrast over the desired thickness. Here, a set of red LEDs were attached to the steel plate above the traction platform, facing downwards. The colour was chosen simply because it was the only unused channel of the camera. The thickest regions (which would therefore be the contact regions) would appear black, and the thinnest regions bright red. The images of this were then inverted, for ease of viewing. The dots in the waveguide absorbed red light, so also left dark patches in the images, but this was minimal and did not affect qualitative viewing. An example image is shown in figure 3.18.

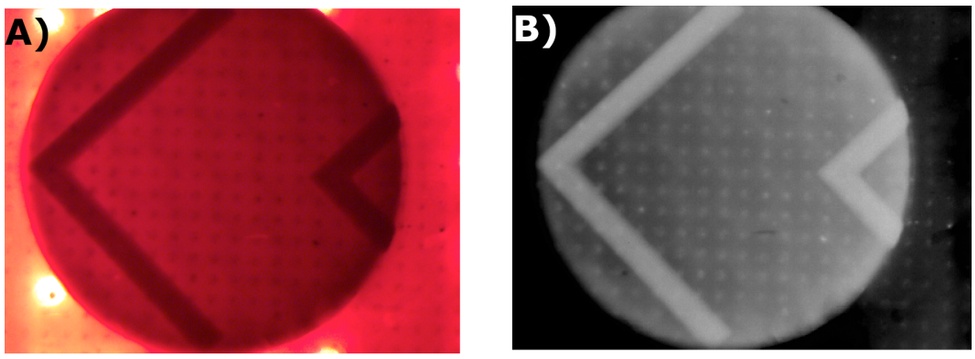

Figure 3.18: An example of the lithophane images used in aligning the pucks with the camera and choosing their orientation when setting up the device, as well as determining where the pucks made contact with the device. Image A) is the raw image, and image B) is the processed and inverted image used for alignment/processing. The brightest regions in B) are those in contact with the waveguide (the thickest material). Note the dots in the waveguide are visible as small patches which are brighter than their surroundings. This is because the dye is florescent and was emitting red light after absorbing ambient light from the room. As long as the difference in thickness between the chevrons and the rest of the puck provided enough contrast, this did not alter the results.

3.4.1 Traction Platform Calibration

Once the traction platform had been built, the in-plane displacement of each dot in the sheet needed to be calibrated for the applied inplane loads. If each dot is considered to be the centre of a square unit cell (i) of length (l) = 2mm, then the average shear stress in the unit cell (τ,where τ can be either τ_{zx} or τ_{zy}) is dependent on the local force. If this force is low enough that the material stays within the linear elastic limit, then the total shear stress is simply related to the displacement of the centre of mass of each dot within its cell (d_i) by

$$\tau = \sum_i \tau_i = \sum_i \frac{\mu d_i}{l}, \tag{3.4}$$

where μ is the experimentally determined shear modulus of the traction layer. This had to be experimentally determined because the exact proportion of monomer solution to crosslinker was not known precisely enough to use any known values. Secondly, the elastomer was sheared via an applied contact load. It was not necessarily the case that varying compression of the elastomer would translate to the same shear modulus, especially as friction should vary with the applied normal load.

As such, the value of μ needed to be determined for a contacting object which would both give a uniform shear under a constant contact load, and measure how this would vary with the contact load. It has been known for some time that the shear under a cylinder, with one of the faces in contact with an infinite plane, produces uniform shear under the face [20], so this was a natural starting point. In order to get a wide range of shear, while keeping the shearing force reasonably in the range that could be applied by hand, cylinders of radius 5 mm were used. These cylinders also had a height of 5 mm. So that the contacting puck was stable, three of these legs were attached to a puck of radius 22.5 mm.

Each leg was identical within the layer height of 0.12mm, which was small enough to assume that the contact load was uniformly distributed to each leg, and small enough that the average load under each 2 mm square of surface would be identical, when properly centred. To actually calibrate the traction surface, this puck was placed in the centre of the waveguide, and a set of known masses added on top. A load cell was attached horizontally to the puck, using a rigid steel cable. This setup is shown in figure 3.19. The voltage-mass response of the load cell needed to be measured before this, simply by hanging known masses from it, while it was attached to a National Instruments USB-6008 DAQ. The signal from the load cell first had to be amplified, using a simple amplifier circuit.

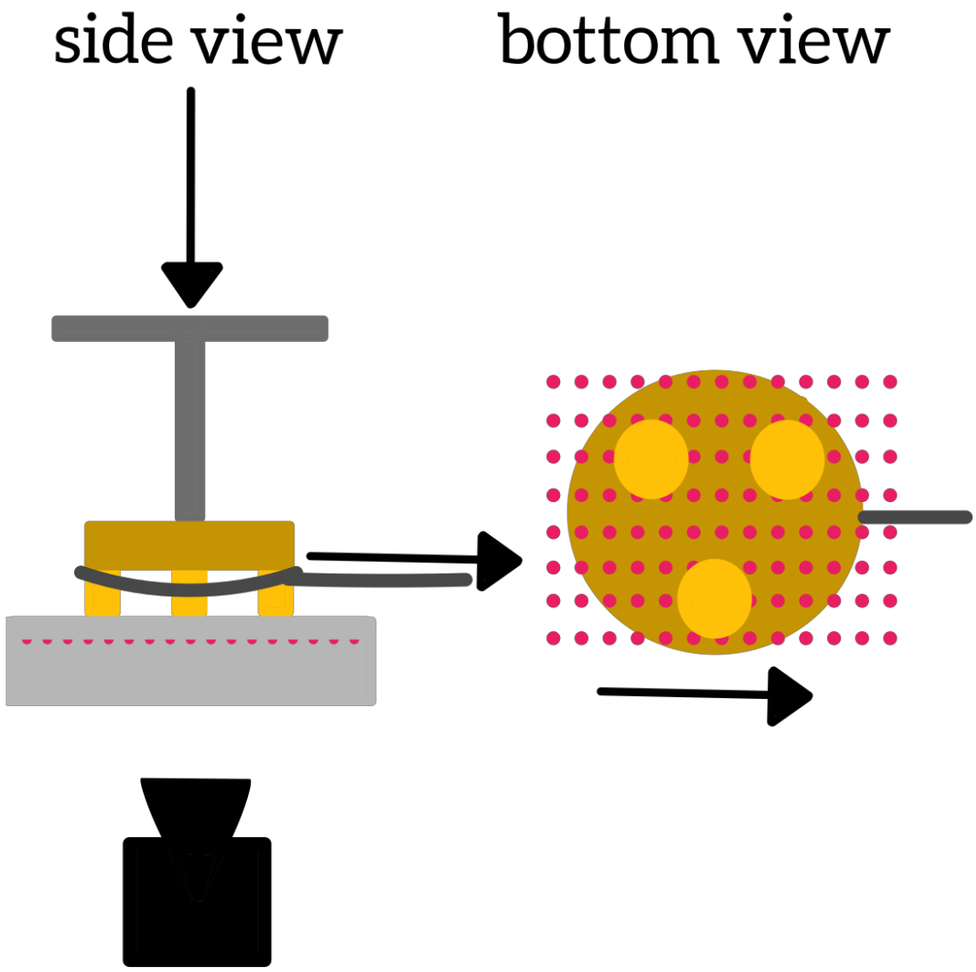

Figure 3.19: A schematic diagram of the setup used to calibrate the traction device. The contacting puck consisted of a 22.5 mm radius cylinder with three cylindrical legs, each with a radius of 5 mm. Various contacting loads were added to the platform above, and the puck was translated by pulling on the load cell, which was attached via a rigid steel cable looped around the puck. Data from the load cell and camera was captured concurrently, and used to map the uniform shear of the dots to the applied horizontal strain, for varying contact loads.

The calibration data for the traction platform was then undertaken by connecting the load cell to the same DAQ card and simultaneously recording the voltage and a video of the dots in the traction layer using software written in MATLAB. The sample and load cell were pulled on, with various contact masses between 1.6 kg and 4.5 kg, which caused it to be translated along the surface. Using tracking software written in MATLAB, the displacement of the dots in the contact area was measured, and the displacement per unit cell plotted vs the load per unit cell measured from the load cell. The results of the calibration steps are outlined below

The results for the load cell calibration are shown in figure 3.20 below. Here, the value of the total mass added to the load cell is plotted vs the amplified voltage it produced, where mass was measured in kilograms and voltage in volts. This resulted in a voltage (v) to mass (m) conversion of $m = 0.5054v + 0.01621$. The voltage was averaged over 150 data points collected over 3 seconds, resulting in a standard error of $\pm 1\,\mu V$, while the masses were measured with an electronic scale with an error of $\pm 5\,g$. Both of these could effectively be treated as zero for the scale of forces used in later calibrations. Only a small number of masses were available in the desired range, however more were not necessary as it was clear that the load cell did not saturate and therefore this load cell and calibration were suitable for later experiments.

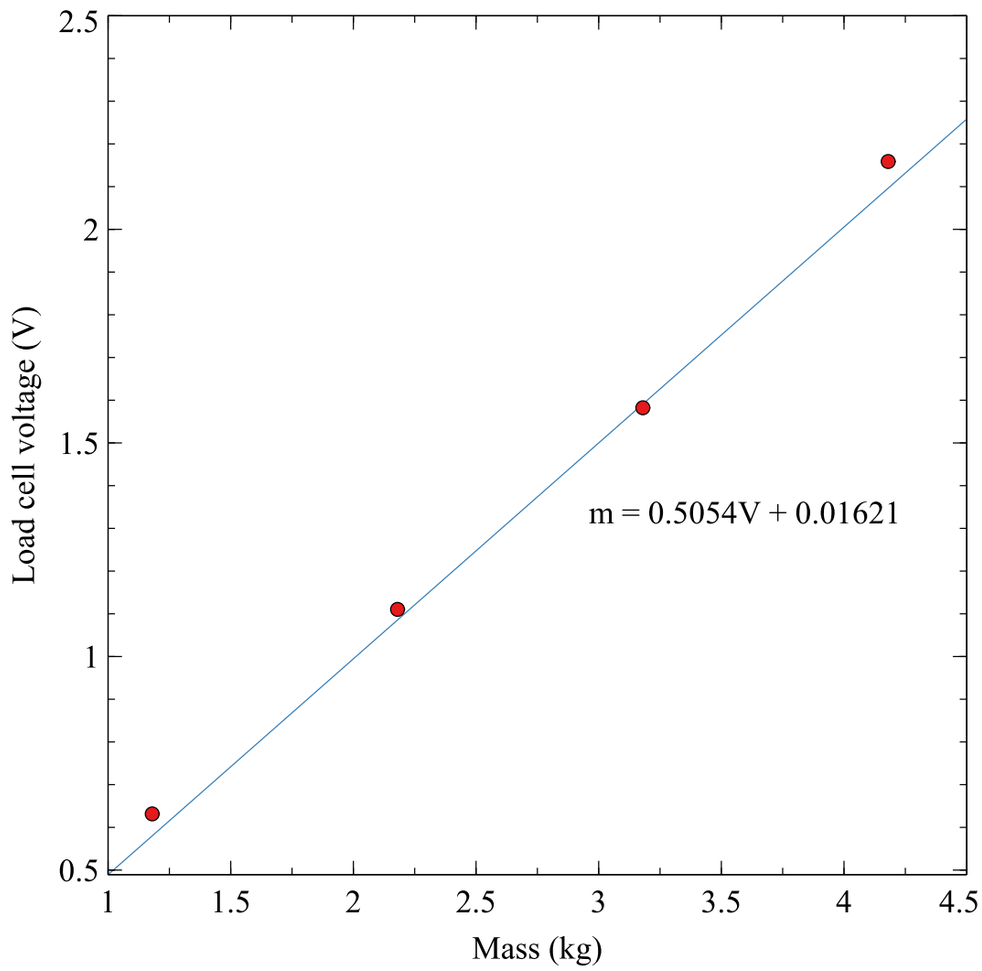

Figure 3.20: The voltage-force conversion used to calibrate the load cell used in the traction platform to take measurements of the total horizontal force. This was achieved by hanging masses off the load cell, using the same steel cable used to pull the masses, so any elastic deformation of the cable is consistently accounted for. The masses used approximated the force range used in these experiments, giving a linear fit of $m = 0.5054V + 0.01621$. m is mass and V is the load cell voltage.

The next step was calibrating the shear of the dots, based on the force measured by the load cell. The dots were tracked using the software written in the following section. When calibrating the displacement of the dots, 3 different contact masses were used: 1.6kg, 3.2kg, and 4.5kg. These were chosen to mimic the approximate contact pressure under the pucks (which was also chosen to mimic the contact pressure under a shoe when the average person is standing). For each of these contact masses, 3 recordings were taken. In each video, the load cell was pulled horizontally, shearing the traction layer under the tripod, and allowed to relax back to the original position. This was also repeated 3 times, over 3 seconds, with the collective results being shown in figure 3.21.

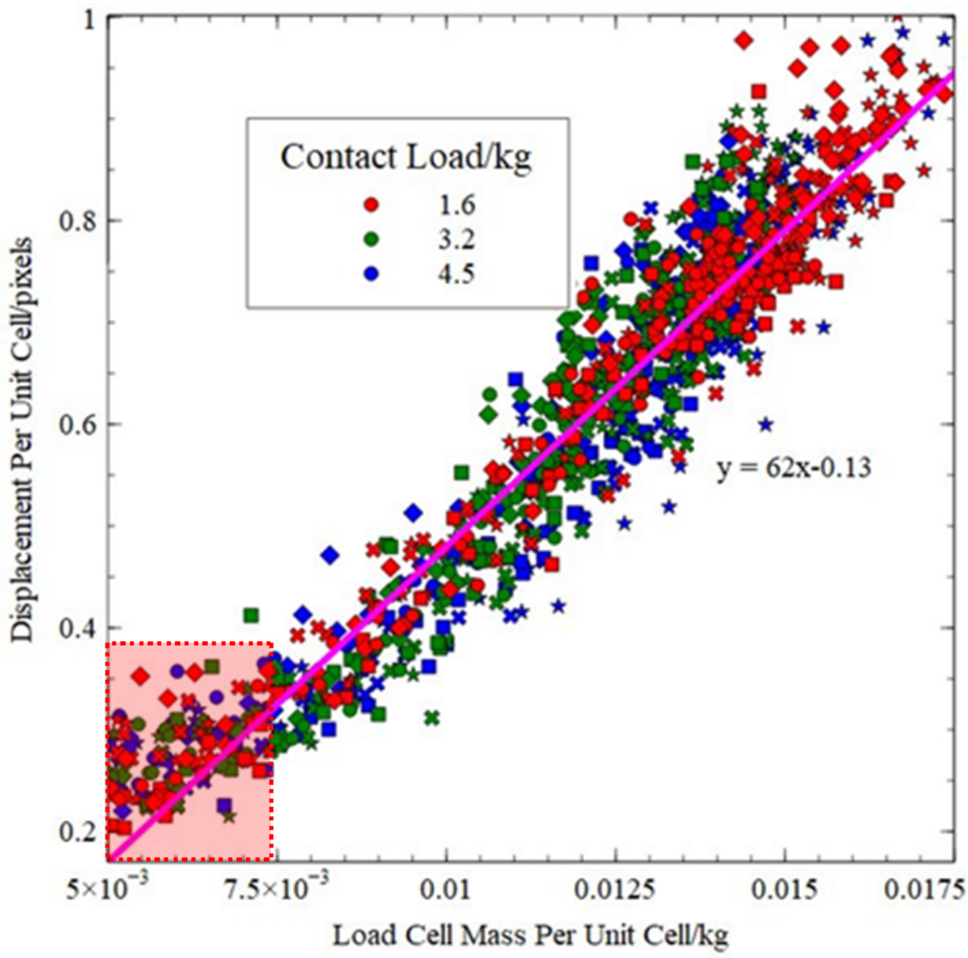

Figure 3.21: The calibration data used to find the force experienced on each unit cell, for the traction platform. A tripod with three cylindrical legs was pulled along the surface, attached to a calibrated load cell. Each colour represents a different contact load, shown in the key. Each shape (circle, star, diamond, and square) represents a single recording. In each recording, a cylindrical puck was translated horizontally, and allowed to relax back to its original position three times. All data collapse on the same line, independent of contact load. The resulting fit, $y = 62x - 0.13$, was then used to convert the displacement of dots to the corresponding shearing force in each unit cell. As the shear of the dots was measured approximately 0.35mm below the contact plane, there was an offset between the measured displacement and the load cell measurement, where low shear values could not be tracked by the camera. These data were excluded from the fit and highlighted in the red region.

The first observation here is that there is no obvious backlash, i.e the straining and relaxation portions are related to the voltage in the same way. This means that the relaxation time of the PDMS layer is lower than the frame rate of the camera and therefore each regime did not need to be independently identified to avoid hysteresis effects. Secondly, within the range tested, all data collapse onto the same line, independent of contact load. In most situations, the friction force (F) should depend on the normal load (N) by $F = \mu N$, and therefore the different contact masses should not collapse onto the same curve without an additional corrective factor. To reiterate: this is due to the surfaces

being rough, and therefore the actual area of contact is much smaller than the apparent contact area. Increasing the contact load deforms the surfaces so that the actual contact area increases, increasing the friction. In this situation, the surfaces must be sufficiently smooth and incompressible that the actual contact area does not increase in the range tested. This also means that the fit calculated here is not applicable for very low contact loads, and the value of the shear modulus will decrease. An experimental test for this is to simply place one of these objects onto one of the FTIR contact platforms. If the puck makes intimate contact with the layer of elastomer at the top of the waveguide and the intensity is fixed, then the actual contact area is not appreciably changing. This was indeed the case, which also means these objects would not be suitable for use in a dual contact-traction imaging setup under these loading conditions.

It is now worth detailing how the software that was written to track the dots and covert their displacement to shear maps worked. This software was used during all experiments involving the traction platform.

3.4.2 Traction Platform Analysis

To convert the images of the displacements to a meaningful traction map, some analysis code had to be written to both identify the dots and account for image noise from the camera. This was also the way in which the effective resolution was determined. The dots needed to have a large enough pixel-wise area to be cleanly resolved, and there needed to be a large number of blank pixels between them, that they can be displaced into. i.e., if a dot only had three blank pixels between it and its neighbour, then only up to two possible values of its displacement could be measured (before they merge into one body).

The result of various tests with different camera lenses was that a minimum of 6 pixels/mm was needed to cleanly resolve the $2.5mm$ objects. The background illumination from the LEDs also varied slightly throughout the waveguide, and a calibration fit was needed to normalise the intensity for thresholding. By selecting values from the background (not under the dye-doped dots), the linear fit found in figure 3.22 was found to be appropriate. This was used as a position-dependant, "rolling", threshold for background subtraction.

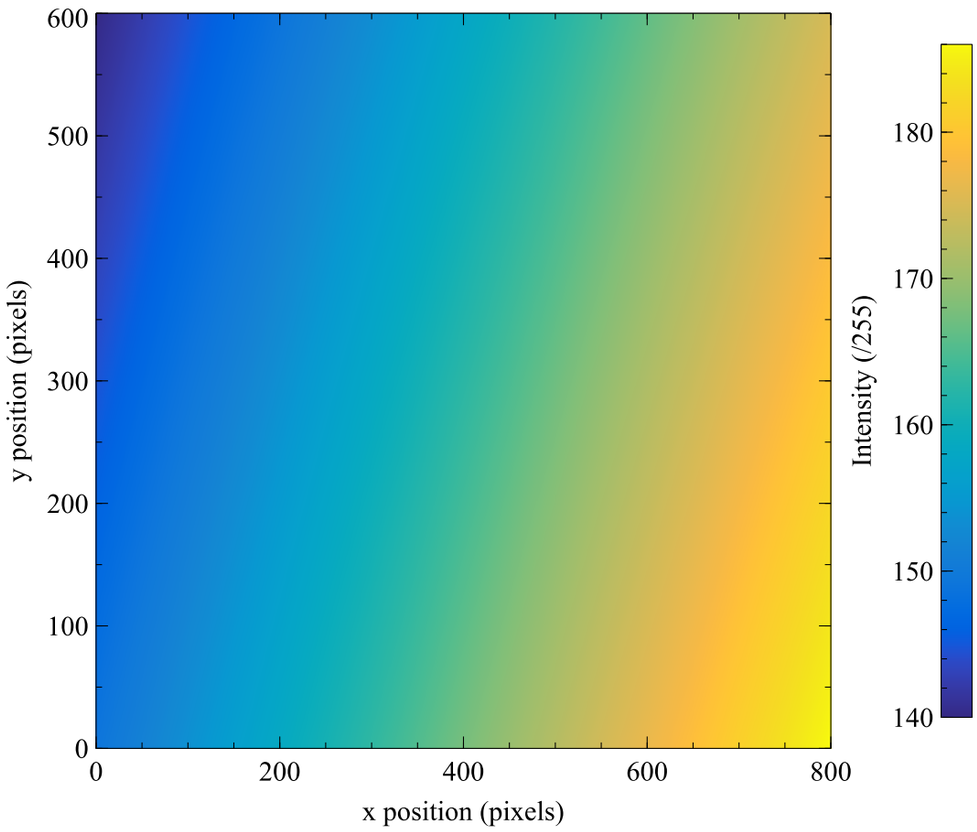

Figure 3.22: The linear fit used for background subtraction in the traction device, due to variations in the LED waveguide intensity. The fit was calculated by automatically taking samples of the background under various points in the waveguide and interpolating. This allowed the background to be uniformly subtracted across the whole device, which was necessary to maintain a consistent radius of dye-doped dots, as perceived by the camera.

The next step involved taking each individual frame of the captured video, extracting the appropriate colour channel used to track the displacements of the dots (usually blue), and binarising it. To remove any small hairline imperfections that may join the dots together, the perimeter of all objects was computed and then removed. Finally, any objects smaller than the volume of the dots (calculated as a minimum 50 pixels) was filtered out, leaving only the dots remaining.

Each dot in each ith frame was then identified and compared to all positions in the original frame. A dot was considered to be the same dot as one of the dots in the initial frame simply based on which has the smallest difference in position, i.e where

$$(x_1 - x_i)^2 + (y_1 - y_i)^2 \tag{3.5}$$

was minimised. x and y denote the positions in each respective axis, for each subscript frame. Using the fits given in figures 3.21 and 3.22, the displacement

from the original position could then be converted to a local strain. Example images of the output at each key step are shown in figure 3.23. When an object was only being translated in one direction, an additional step was also required.

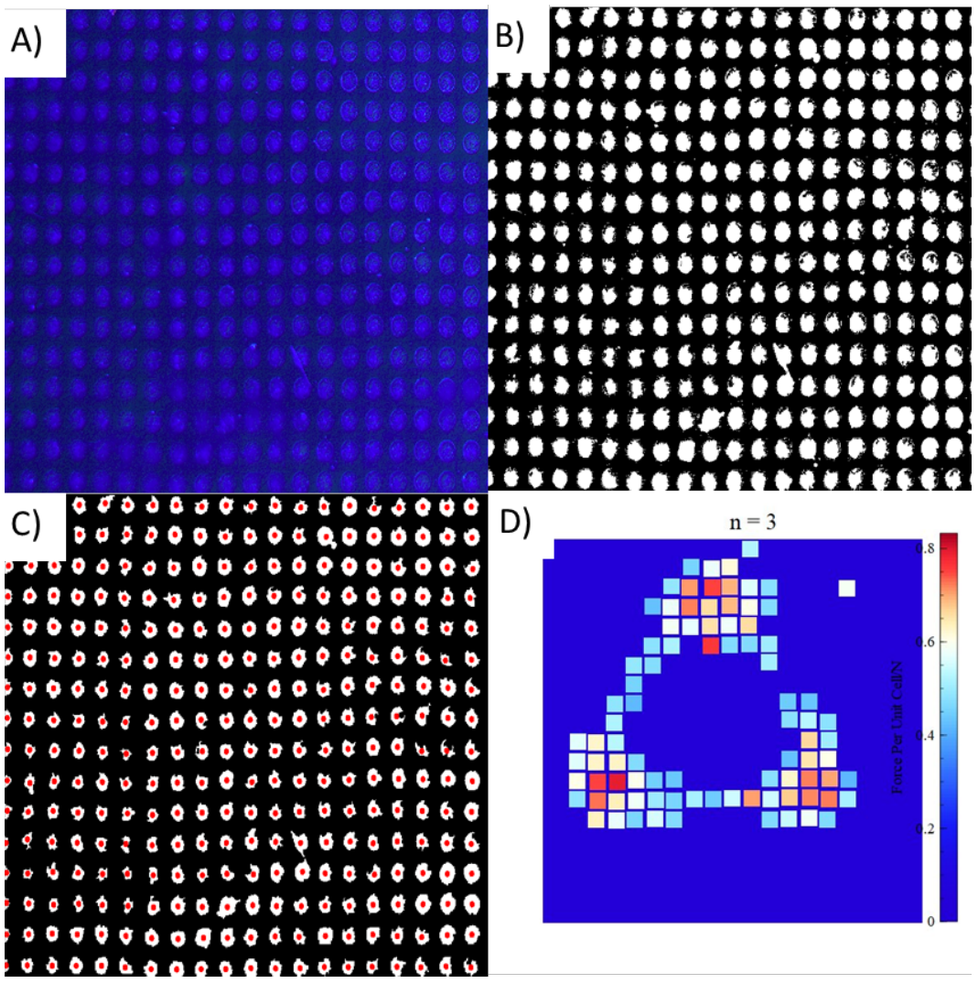

Figure 3.23: The digital output at each stage in the code used to convert images of the traction waveguide to maps of local shear. A) is the blue channel of the original image: the dots can clearly be seen, but there is an obvious background and various imperfections in the surface. In B), the background subtraction has been applied, and the remaining image binarised. Various imperfections and small scratches can still be seen. By first removing the perimeter of all remaining white objects and then removing objects with a volume of less than 50 pixels, small imperfections and thin scratches that used to join the dots have been removed. This is shown in C) The centres of mass of each dot have been added as a set of red markers. D) shows the output traction map, computed by comparing the centres of mass in a deformed state, to the un-deformed state. In this example image, a 22.5 mm puck with an $n = 3$ polygon was rotated. The final image has an effective resolution of 20-by-20 unit cells/dots.

The platform was originally held in place by raised metal brackets, which kept it from moving horizontally but allowed for vertical movement. This meant contact loads could be easily measured with load cells positioned below the waveguide. However, this design had to be revised, as the strength of the brackets was not sufficient to keep the waveguide in place. The frame that

held it in place above the camera consisted of extruded aluminium rail, held together with T-nuts. This metal frame could twist considerably, displacing the waveguide with respect to the camera. Figure 3.24 gives evidence of this. Instead, the waveguide was fully clamped in place with a metal bracket, which was then bolted directly to the frame. This bracket was thick enough to prevent the frame from twisting, but meant load cells could no longer measure the contact force, as the platform was clamped in place. If a contacting object was translated, a small amount of platform displacement was still observed, but no torque. Neither displacement nor torque was observed during rotational measurements. To account for this motion, the displacement of a small selection of dots far from the contacting body was averaged, and subtracted from all points in the output image.

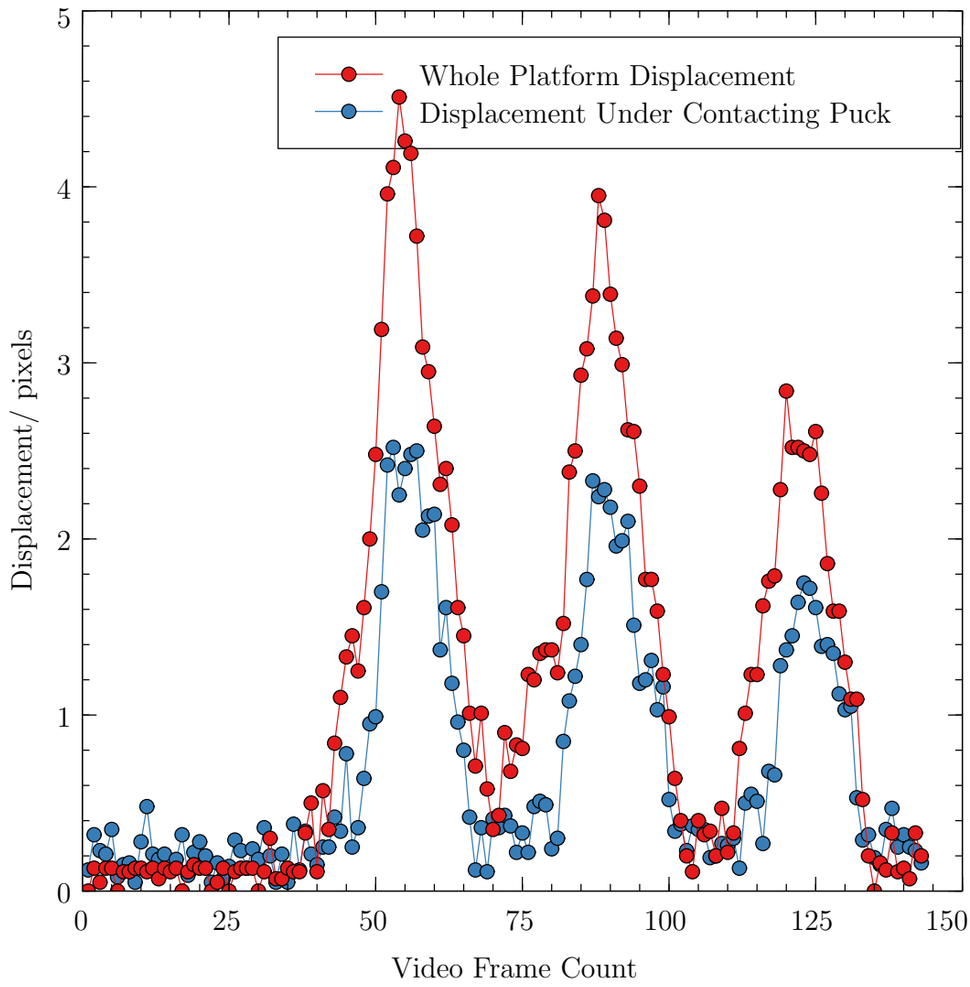

Figure 3.24: An example of the initial problems with recovering information on shear from the traction device, before the frame was adapted to have the platform fully bolted to it. Here, a set of dots are being traced below a contacting object that is translated (blue). Another set of dots, far from the contacting object and therefore not experiencing shear, are being tracked in red. The average displacements of these sets of dots are plotted, recorded over 150 frames of video in 3 seconds. It can clearly be seen that most of the applied load goes into moving the platform rather than shearing the dots. The displacement is in fact lower under the dots under the contacting object, due to this being the centre of rotation for any applied torque. This means the platform displacement could not be easily subtracted, and a redesign was needed.

Two main kinds of experiments were then undertaken: translation and rotation. These involved various patterned pucks, with their designs described in chapter 3.2.

3.5 Setting Up a Traction Simulation

As the rotational traction problem analysed has no known quantitative solution, a numerical one was needed to compare the experimental results to. As such, a simulation of the problem was made in the finite element analysis software ABAQUS. This required some non-standard setup, which was repeated throughout the various experiments, so is detailed here as reference.

Firstly, a plane mimicking the size of the traction surface was defined. This was given the same Young's modulus as the real traction surface, but a Poisson ratio of 0.49 (as close to 0.5 as the software would allow). To easily define the rotational problem, the coordinate system was then manually redefined from Cartesian (x, y, and z) to polar coordinates ($r = \sqrt{x^2 + y^2}$, $\theta = arctan\left(\frac{y}{x}\right)$, and z). The contact area, traction force, and contact load then needed to be defined in these units, with the equations developed to do so as follows.

The contact area was defined by a function in r which determined the inner (r_1) and outer (r_2) radii of the thin polygonal shells, which needed to return 1 within the desired contact region, and 0 elsewhere :

$$f(r) = \frac{\left(1 + \frac{|r_2 - r|}{r_2 - r}\right)\left(1 + \frac{|r - r_1|}{r - r_1}\right)}{4}. \tag{3.6}$$

This expression contains a pair of absolute functions, which are then normalised. Each of these ratios is a step function with the step centred either on r_1 or r_2, which returns ± 0.5 depending on whether r is between r_1 and r or not. This is then normalised to give a step between 0 and 1, and the two are multiplied into a top-hat function, to act as a radial mask. These are illustrated in figure 3.25, for clarity.

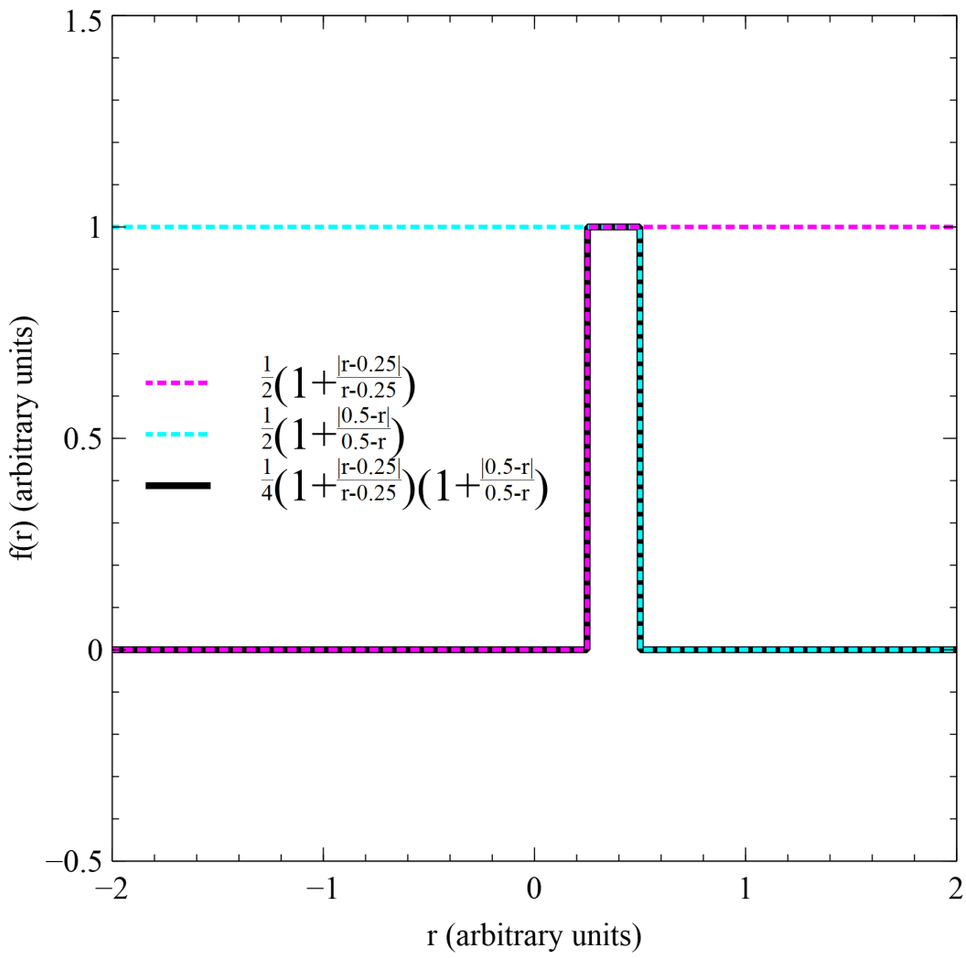

Figure 3.25: A visual representation of how a set of floor functions determines the contact area under a polygon, in the radial direction. Here, the minimum radius $r_1 = 0.25$ and the maximum radius $r_2 = 0.5$. The two step functions transition between 0 and 1 at 0.25 (magenta), and 0.5 (cyan). The combined top hat function is only non-zero in the desired contact region (black).

A regular polygon of n number of sides can be defined in the θ direction by

$$f(\theta) = \frac{cos(\frac{\pi}{n})}{cos(\theta - \frac{2\pi}{n}\left\lfloor\frac{n\theta+\pi}{2\pi}\right\rfloor)}, \tag{3.7}$$

and combining these two gives the complete expression for a polygonal shell in polar coordinates:

$$f(r,\theta) = \frac{\left(1+\frac{|r_2-r|}{r_2-r}\right)\left(1+\frac{|r-r_1|}{r-r_1}\right)}{4}\frac{cos(\frac{\pi}{n})}{cos(\theta - \frac{2\pi}{n}\left\lfloor\frac{n\theta+\pi}{2\pi}\right\rfloor)}. \tag{3.8}$$

However, r_1 and r_2 also need to scale according to θ, as the maximum and minimum radii are also functions of this. Therefore $r_1 \to r_1 f(\theta)$ and $r_2 \to r_2 f(\theta)$. The final expression is cumbersome, so is best simplified as

$$f(r,\theta)\frac{1}{4}\left(1+\frac{|r_2 f(\theta)-r|}{r_2 f(\theta)-r}\right)\left(1+\frac{|r-r_1 f(\theta)|}{r-r_1 f(\theta)}\right)f(\theta). \tag{3.9}$$

This gave the contact region to apply the uniformly distributed loads within, and applying them was simply a matter of specifying a contact load in $\hat{z}$, and a rotational force in $\hat{\theta}$. The software was then able to calculate stress maps from the defined problem. However, it must be noted that the loads were applied directly to the surface as if the contacting object was affixed to it, i.e. there was no provision for slip. The solutions computed were for loads in the same range as the experimental setup, and for the same values of n, for otherwise direct comparison. To keep them further comparable to the experimental case, the simulation was kept course-grained. The experimental case produced 20×20 unit cell images, so the simulation was limited to the same number of nodes in each plane.

Bibliography

[1] *Technical data sheet - sylgard™ 184 silicone elastomer*, Form №11-3184-01 C, Dow, 2017.

[2] *Tables of physical and chemical constants / originally compiled by G.W.C. Kaye and T.H. Laby ; now prepared under the direction of an editorial committee.* 16th ed. 1995, ISBN: 0582226295.

[3] C. G. Tompkins and J. S. Sharp, "Dual optical force plate for time resolved measurement of forces and pressure distributions beneath shoes and feet," *Scientific reports*, vol. 9, 2019. DOI: 10.1038/s41598-019-45287-9.

[4] R. Attaie and R. Richter, "Size distribution of fat globules in goat milk," *Journal of Dairy Science*, vol. 83, 2000. DOI: 10.3168/jds.S0022-0302(00)74957-5.

[5] J. S. Sharp, S. F. Poole, and B. W. Kleiman, "Optical Measurement of Contact Forces Using Frustrated Total InternalReflection," *PHYSICAL REVIEW APPLIED*, vol. 10, 2018. DOI: 0.1103/PhysRevApplied.10.034051.

[6] T. Edeskär, "Technical and environmental properties of tyre shreds focusing on ground engineering applications," 2004.

[7] P. Papagiannis, P. Azariadis, and P. Papanikos, "Evaluation and optimization of footwear comfort parameters using finite element analysis and a discrete optimization algorithm," *IOP Conference Series: Materials Science and Engineering*, vol. 254, 2017. DOI: 10.1088/1757-899X/254/16/162010.

[8] V. Pinto, T. Ramos, S. Alves, *et al.*, "Comparative failure analysis of pla, pla/gnp and pla/cnt-cooh biodegradable nanocomposites thin films," *Procedia Engineering*, vol. 114, 2015. DOI: https://doi.org/10.1016/j.proeng.2015.08.004.

[9] J. Y. Park, S. J. Yoo, E.-J. Lee, D. H. Lee, J. Y. Kim, and S.-H. Lee, "Increased poly(dimethylsiloxane) stiffness improves viability and morphology of mouse fibroblast cells," *BioChip Journal*, vol. 4, 2010. DOI: https://doi.org/10.1007/s13206-010-4311-9.

[10] S. N. Srihari and Y. Tang, "Computational methods for the analysis of footwear impression evidence," in *Computational Intelligence in Digital Forensics: Forensic Investigation and Applications*. Springer International Publishing, 2014, vol. 555. DOI: 10.1007/978-3-319-05885-6_15.

[11] J. Hale, R. Lewis, and M. J. Carré, "Rubber friction and the effect of shape," *Tribology International*, vol. 141, 2020. DOI: https://doi.org/10.1016/j.triboint.2019.105911.

[12] V. C. Hoang, W. Zhan, Y. Fang, and P. Huang, "Experimental and simulation analyses of the stress field of slider-on-block contact for static and slip states," *SN Applied Sciences*, vol. 2, 2020.

[13] K.-S. Shih, S.-Y. Jhou, W.-C. Hsu, *et al.*, "A biomechanical investigation of athletic footwear traction performance: Integration of gait analysis with computational simulation," *Applied Sciences*, vol. 10, 2020. DOI: 10.3390/app10051672.

[14] H. Driscoll, H. Koerger, T. Senior, and S. Haake, "The use of photoelasticity to identify surface shear stresses during running," *Procedia Engineering*, vol. 2, 2010. DOI: https://doi.org/10.1016/j.proeng.2010.04.109.

[15] Smooth-On, "Clear flex™ series technical overview," 2019.

[16] P. Fino and T. E. Lockhart, "Required coefficient of friction during turning at self-selected slow, normal, and fast walking speeds," *Journal of biomechanics*, vol. 47, 2014.

[17] A. C. Fischer-Cripps, *Introduction to Contact Mechanics*, Second Edition. Springer, 2007, ISBN: 978-0-387-68187-0.

[18] C. C. Ibeh, *Thermoplastic Materials: Properties, Manufacturing Methods, and Applications*, Ninth Edition. CRC Press, 2011, ISBN: 978-1-4200-9383-4.

[19] H. Du, R. A. Fuh, J. Li, A. Corkan, and J. S. Lindsey, "Photochemcad 2. a refined program with accompanying spectral databases for photochemical calculations," *Photochem. Photobiol.*, vol. 81, 2005.

[20] 1. Johnson K. L. (Kenneth Langstreth), *Contact mechanics [electronic resource] / K.L. Johnson.* eng. Cambridge, 1985, ISBN: 9781615832187.

Chapter 4

Contact Imaging Of Shoes And Feet

4.1 Experimental Methods

After the calibration steps outlined in chapter 3.1, the contact imaging platform was ready for use. The intent was to demonstrate its use as a real-time and high resolution contact pressure sensor for both biomechanical and product design applications. As such, various training exercises were performed by a pair of participants. These exercises were completed both barefoot and with various shoe tread patterns. This allowed the lower-body biomechanics of the subject to be observed, based on how they distributed force into the platform. It also allowed the mechanics of the shapes in the shoe tread patterns to be studied.

The exercises chosen were standard plyometric training exercises which are often used by sports scientists to assess the strengths of athletes [1]. These included jogging on the spot, counter-movement jumps, and drop jumps. These were repeated prior to collecting the data, to allow the participant to get used to the exercises and then captured at a sample rate of 200Hz. It must be noted that no special arrangements had to be made to allow this platform to work: the overhead room lights could remain on above the platform and the individual surfaces did not have to be overly clean in order to gain an accurate FTIR response (i.e. small amounts of dirt and dust from regular wear were allowable), so no additional training or setup phase was required, and it could therefore be easily applied outside of a lab environment.

A description of each motion will be repeated in the appropriate section, however a summary will also be given here, for the sake of reference.

Jogging

A simple biomechanical motion where the subject moves on the spot in such a way that they push off on one foot, then push off on the second a moment before the first foot lands. The gap between the first landing and second push off phases is simply related to the speed of the subject.

Countermovement Jump

A kind of training exercise used to determine the lower-body power generation of a subject. The participant initially starts from a full standing position, with their knees straight and their feet shoulder-width apart. Their hands must remain on their hips, so their upper body cannot contribute to upward power generation. In the push-off phase, the participant rapidly moves downwards, until their knees form a 90° angle. The participant then pushes off with their feet with as much effort as possible, and must jump so that their legs are fully extended. They must then land so that both feet land at the same time, identically, and with knees fully extended [2].

Drop Jump

Another training exercise designed to determine instantaneous lower-body power generation of a subject. The subject begins by standing on a raised platform, a few 10s of centimetres above ground level. They must then drop (not jump) off the raised platform and land on the ground. In the same motion, they must then push back off the ground and land on the raised platform with both feet [1].

4.2 Contact Platform Results

The various training exercises were performed by a pair of participants, under different interfacial conditions (e.g. barefoot, shoes of various tread patterns and colour). These were performed with one foot on each waveguide, to allow data from the load cells to be collected for each foot separately, and compared to the two portions of the FTIR image. Each exercise was recorded for only a few seconds, under ambient lighting, with pressure data collected every 5 ms. Exercises were repeated multiple times before data collection began, to ensure the participants were used to the setup (i.e. performing exercises on a transparent platform approximately 0.5 m from ground level). Otherwise, there was a tendency for the participant to do one of two things. First, they would often not plant their feet completely on the waveguides, partly landing on the surrounding metal brackets instead. This obviously meant the FTIR images would be incomplete, but the load cells would still pick up this weight, so both results would not be comparable. Secondly, the participants would not necessarily perform the exercises correctly (both from lack of practice and being unnerved by the platform). For example, during a counter movement jump, the participant may brace outwards when they land, or simply not jump very high on the clear platform. It must be noted that, as the platforms are being viewed from below, the subjects left and right feet appear on the right and left of the images, respectively. The first simple exercise that was performed was to have the subject jogging barefoot on the spot.

Jogging

In this case, the subject simply jogged on the spot, with one foot on each platform. The data was collected over 5 seconds, with a sample rate of 200Hz. A 0.8 s section of this data is shown in figure 4.1.

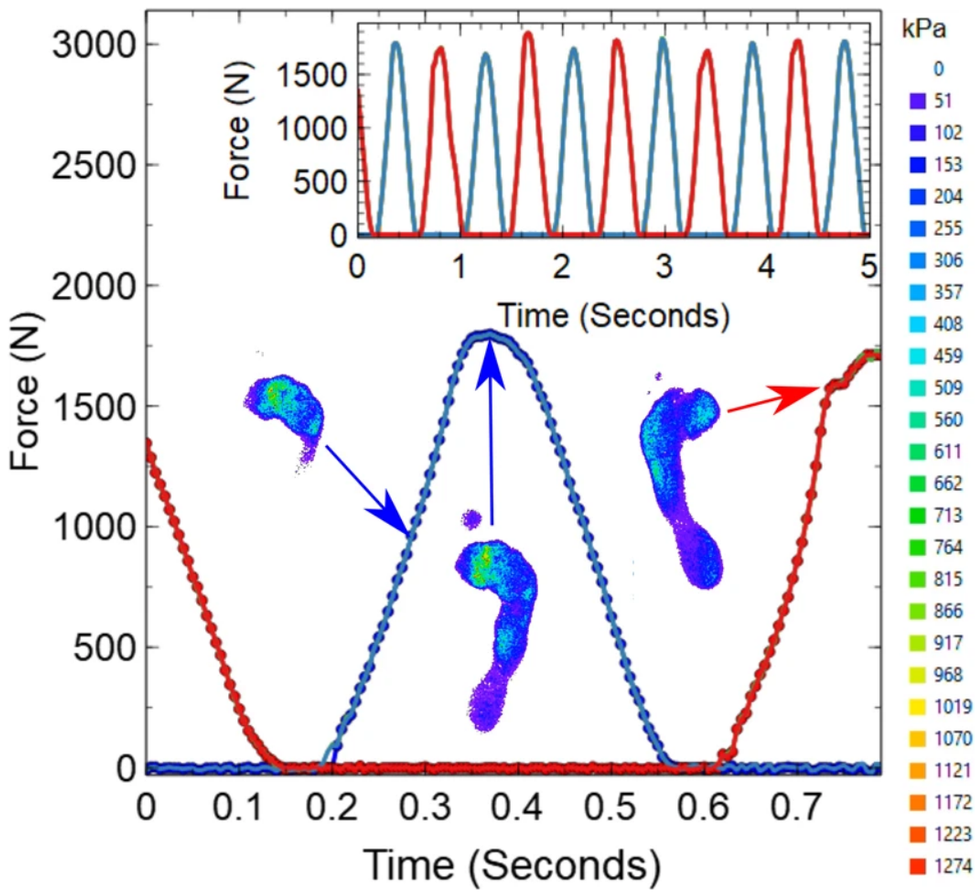

Figure 4.1: The FTIR force data collected from a subject jogging on the spot over a time period of 0.8 s. The FTIR force data from the left foot has been summed to give the blue dotted line, and the red dotted line is the right foot FTIR data. Inset is the load cell data for each platform, with the red and blue solid lines corresponding to the same platforms as the FTIR data. Also inset are some examples of the FTIR images, with the period they were extracted from indicated. The pressures the colours indicate are highlighted in the legend. [3]

The first obvious observation is that the load cell and summed FTIR data match under both platforms. The more interesting observations come from analysing the FTIR pressure maps themselves. The participant clearly favours their right foot, as this foot had the higher total force associated with it. However, this actually leads to higher pressures under the left foot. The participant is pushing off their left foot with less force, but is also not being planted as evenly, evidenced by the higher pressures around the ball of their left foot. The load cell data alone would only indicate that the left leg is weaker than the right, the difference in the loading mechanics is only visible with the FTIR pressure maps. After this, the next exercise to be analysed is from a counter-movement jump.

Counter-movement Jumps

A counter-movement jump is a kind of training exercise used to determine the power generation (and uniformity of its distribution) of a persons lower body muscles [1], as well as their ability to generate power quickly. The participant initially starts from a full standing position, with their knees straight and their feet shoulder-width apart. Their hands must remain on their hips, so their upper body cannot contribute to upward power generation. In the push-off phase, the participant rapidly moves downwards, until their knees form a 90° angle. The participant then pushes off with their feet with as much effort as possible, and must jump so that their legs are fully extended. They must then land so that both feet land at the same time, identically, and with knees fully extended [2]. Two comparisons are analysed here: one barefoot, and one wearing sports shoes.

The barefoot counter-movement jump data is shown in figure 4.2, following the same experimental procedure as before.

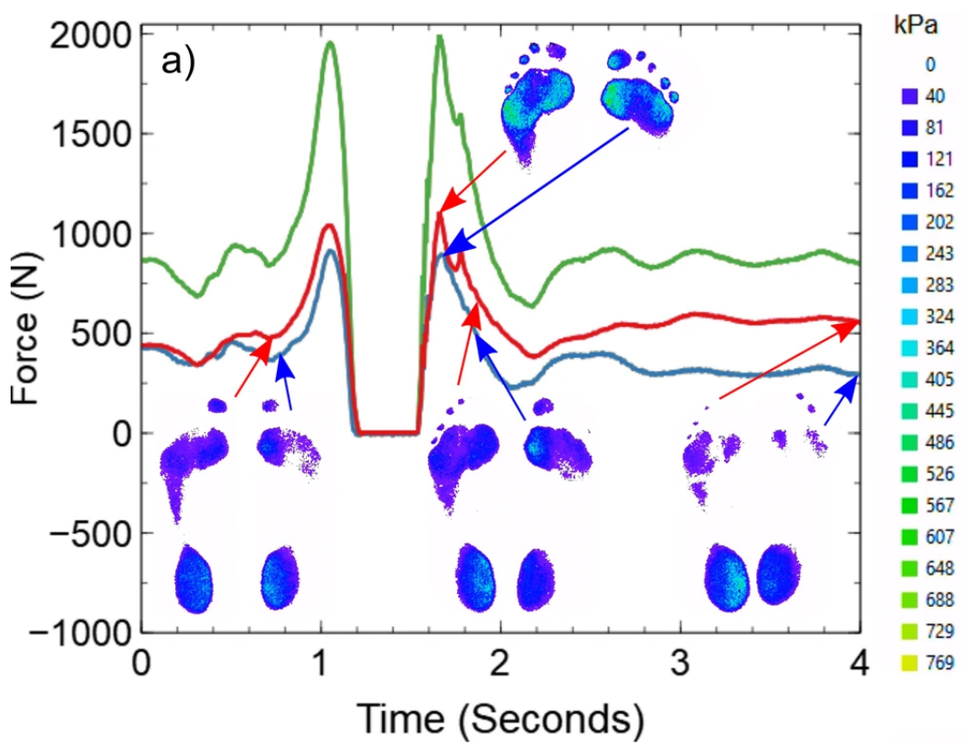

Figure 4.2: The FTIR derived forces collected from a barefoot counter-movement jump, collected over a period of 4 s. The red data corresponds to the total FTIR-derived load under the left foot/platform, with the blue data being the equivalent for the right. The green data is the sum total load on both platforms. Example FTIR images, at various key stages of the movement, are included and the arrows indicate their origin in the curve. The pressures indicated by the colours of the FTIR images are highlighted in the legend. [3]

The summed data, showing the total forces exerted on each platform, demon-

strate a generally uniform loading phase, although the participant produces slightly more power ($\sim$100 N) with their right foot. This is unsurprising, as it is the same participant as the jogging data in figure 4.1. There is, however, greater instability in the landing phase. This can be observed simply by the red and blue lines deviating from each other after the landing at $\sim$ 1.8s - the red line is consistently higher, so the participant is taking more weight onto their right foot. However the FTIR images also show they are rocking back and forth: they initially land on the ball of their foot, quickly planting their feet firmly, and then rocking onto their heel. In order to safely land high jumps and prevent muscle/joint injury (either instantaneously or over time), it has been determined that this is the ideal technique for distributing the load through the muscles in the legs [4]. Landing on the balls of the feet cushions the initial blow without shocking the knee joints, and rolling backwards onto the heels allows the forces to be absorbed by the large muscles at the back of the legs. Landing flat footed would cause potential injury to the joints by compressing them instead of allowing the muscles to absorb the forces, and any unevenness or twisting in the feet would also potentially cause joint/ligament damage through torque. Both of these are often present in inexperienced individuals [4]. Thankfully for the participant, there is minimal evidence of this and they are unlikely to injure themselves. There are, however, few sports where the participant is barefoot, and shoes are well known to restrict movement, so it is worth analysing the same situation in these conditions.

The same experiment was performed identically, including with the same participant, with the only difference being they were wearing a pair of sports shoes. These were their size, so the shoe would not overly restrict motion or allow the foot to slide inside it and potentially affect the way the participant had to balance their weight. They were also new, as wear patterns would potentially change the results (indeed, they are known to substantially change the traction results under shoes [5]), and it would also have had to be considered if wearing of the sole from the participants' weight distribution would affect the results compared to unnatural wear or the weight distribution of another person/person analogue. The results of this situation are shown in figure 4.3.

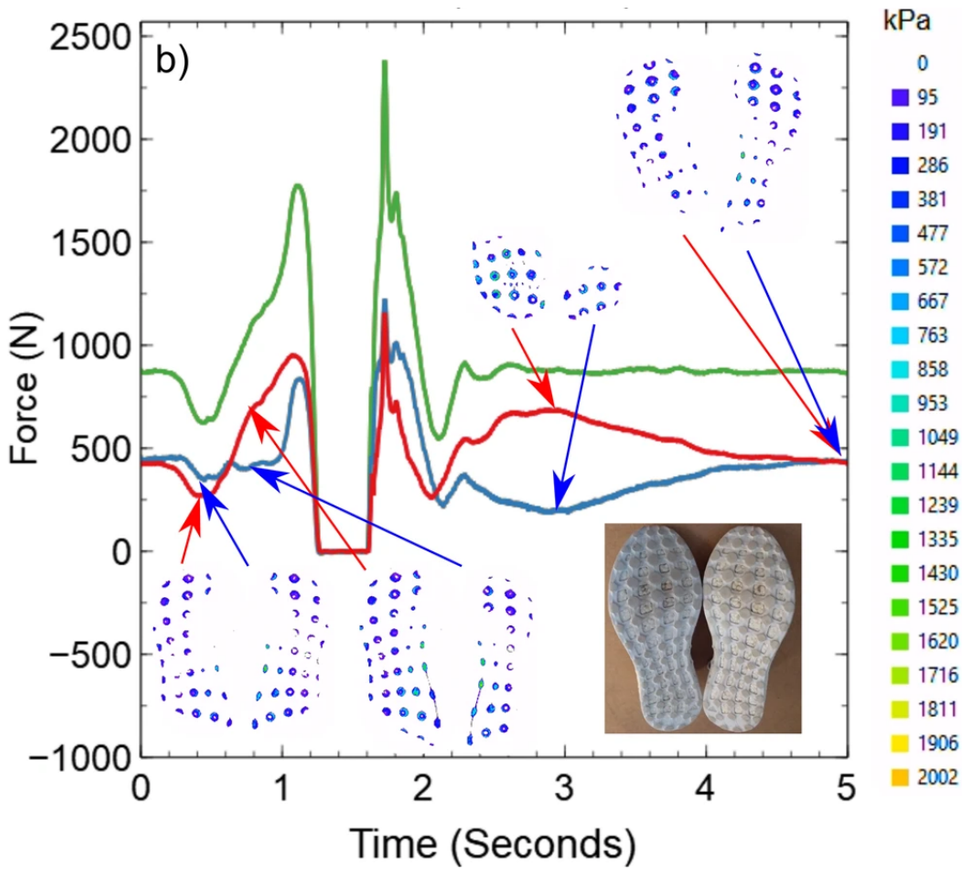

Figure 4.3: The FTIR derived forces collected from a counter-movement jump with shoes on, collected over a period of 5s. The red data corresponds to the total FTIR-derived load under the left foot/platform, with the blue data being the equivalent for the right. The green data is the sum total load on both platforms. Example FTIR images, at various key stages of the movement, are included and the arrows indicate their origin in the curve. The pressures indicated by the colours of the FTIR images are highlighted in the legend. The shoes used are shown in the bottom right corner. [3]

There are a number of notable differences in this case, compared to the barefoot case. The first is in the push-off phase: $\sim 0-1$s. The red and blue lines do not match as well as in the barefoot case, the participant is both pushing off their right foot first, and with greater force. There does not appear to be any large difference in the way the load is being distributed, however. A potential reason for this is the shoes themselves, specifically the pattern on the bottom, which has been enlarged in figure 4.4 for clarity. The pattern consists of an array of deformable cylinders. The pressure distribution through them is ring shaped - decreasing radially as it reaches the centre, with is then not in contact with the smooth platform. There is no break in the circular region, so loading them vertically would compress the ring and push out the air from the centre. This would create a negative pressure and would resist separation from the platform through suction. This would likely add extra resistance to the push-off phase and cause the participant to alter their jump. As they are already intending to

produce as much instantaneous vertical force as possible, this would explain why they are pushing off for longer and have lower power at the end of the push off phase: the broad 700N peak before the 900N peak at 1s is the participant separating their shoes from the platform, with their remaining (and now lower) energy being transmitted into their jump. This is consistent, as the broad peak is 200N above the resting load, and the peak is 200N lower than in figure 4.2.

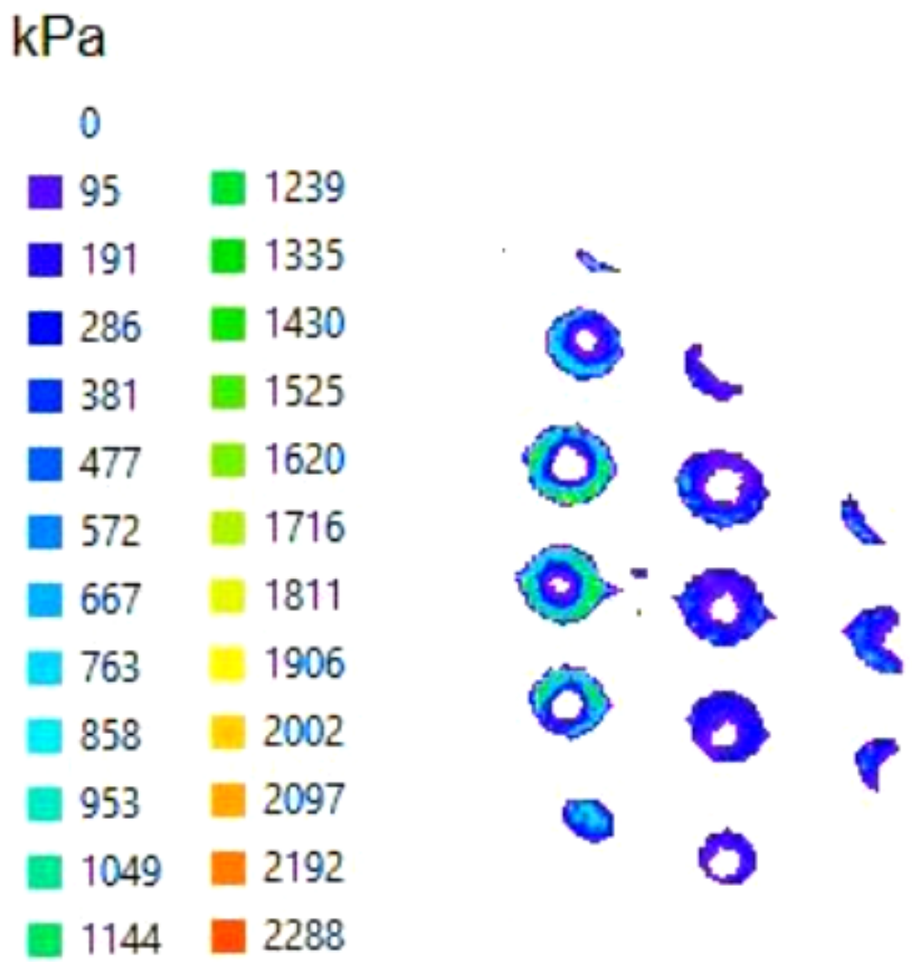

Figure 4.4: A closeup example of the pressure distribution under the white shoes, with the corresponding tread pattern also shown. The corresponding pressures are highlighted in the legend on the left. A ring shaped pressure distribution is evident, with decreasing pressure heading towards the centre and a hollow where the tread is not in contact with the surface, acting like a suction cup. This distribution is not evident in the shape of the tread pattern an indicates a manufacturing flaw - the circular tread is not perfectly flat. This suction cup-like effect would add resistance when pushing off a surface, wasting energy.

In the landing phase, the participant has yet to recover their balance. They have landed with both feet identically, but pass an extra 500N through their right foot and were not rocking as evenly - they were rolling back further on their left foot.

The final exercise that was performed was a drop jump, and was performed by two different participants.

Drop Jumps

In a drop jump, the participant does not initially start standing on the force platform, but on a raised platform just behind it (a further 0.2m above the force plate in this case). They must then drop off the raised platform, avoiding *jumping* off it, and land on the force plate [1]. In the same motion, they must then push back off the force plate and land on the raised platform with both feet. These participants then repeat the first movement and drop back onto the platform, so their final landing state is visible. It must also be noted here that, although it was not performed, a second (further raised) force platform could replace the raised platform and allow all landing phases to be visible with little added complexity. The same process as the previous experiments were again applied, multiple repeats were practised so the participants could get used to the movement and experimental setup (even more important here as they started further in the air) and data was sampled concurrently with a frequency of 200Hz. The same participant as the previous experiments was the initial subject, and results of their drop jump are shown in figure 4.5.

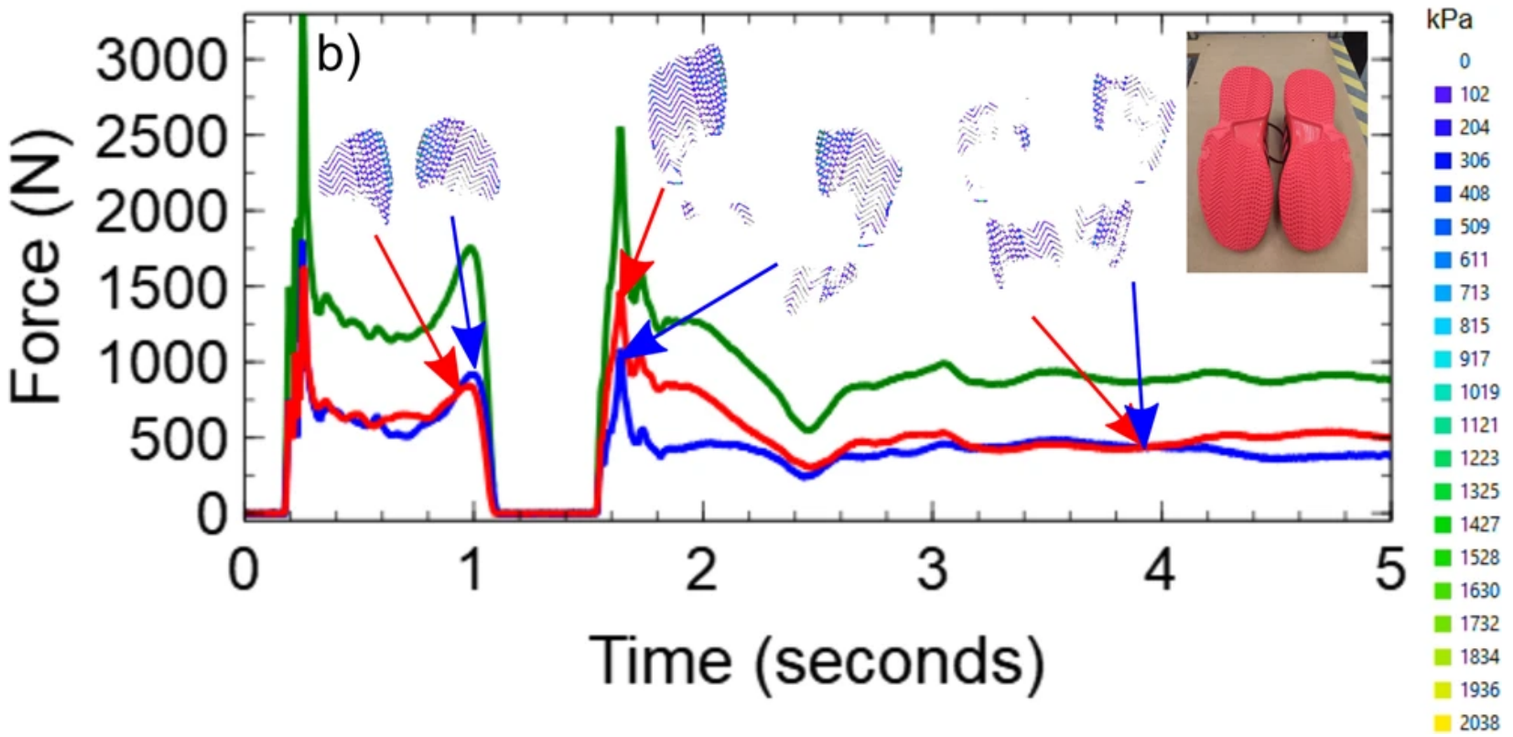

Figure 4.5: The FTIR derived forces for a drop jump performed by a participant wearing red soled shoes. The red data corresponds to the total FTIR-derived load under the left foot/platform, with the blue data being the equivalent for the right. The green data is the sum total load on both platforms. Example FTIR images, at various key stages of the movement, are included and the arrows indicate their origin in the curve. The pressures indicated by the colours of the FTIR images are highlighted in the legend. The shoes used are shown in the top right corner. [3]

In this movement, the participant is not initially stood on the platform, so 0 load is initially registered. The combined landing and push off phase is then observed at $0.2 - 1$s. The summed data once again indicated the participant is able to land and push-off with both feet evenly, unlike when they were wearing the previous shoes. The FTIR pressure maps also show they are managing to evenly distribute the force they are generating through both feet. It is in the secondary landing phase ($1.6s+$) that they are once again leading with their right foot and rocking back on their left. The effect is much less pronounced in these shoes, which could indicate they are helping to distribute the load more evenly and lower the possibility of injury, although lack of practice on the side of the participant cannot be discounted. This data can also be compared to the drop jump data for a second participant, this time wearing blue soled shoes and shown in figure 4.6.

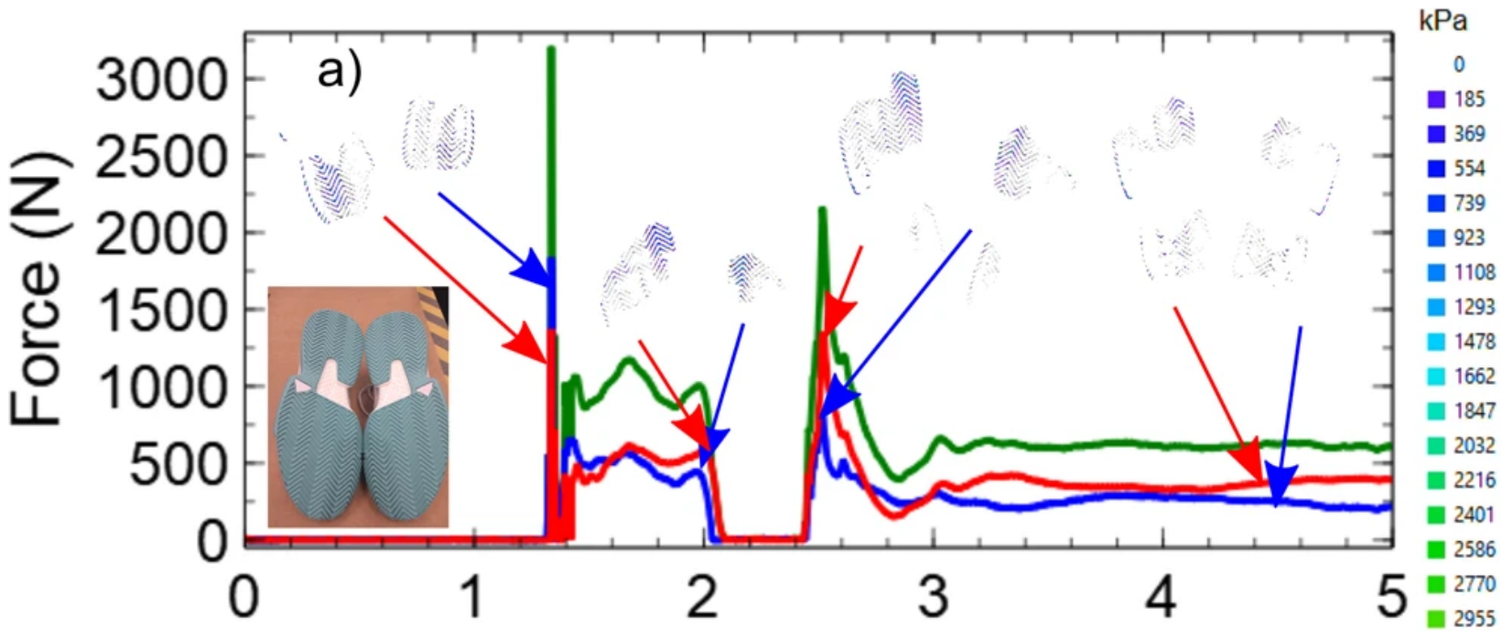

Figure 4.6: The FTIR derived forces for a drop jump performed by a new participant wearing blue soled shoes. The red data corresponds to the total FTIR-derived load under the left foot/platform, with the blue data being the equivalent for the right. The green data is the sum total load on both platforms. Example FTIR images, at various key stages of the movement, are included and the arrows indicate their origin in the curve. The pressures indicated by the colours of the FTIR images are highlighted in the legend. The shoes used are shown in the top right corner. [3]

The total summed FTIR data given in the linear plots show this participant is able to provide a much more consistent load between both feet at any one time, although they produce less power overall. By itself, this would potentially indicate much more control on their behalf, although with less lower body strength. The FTIR maps once again alter this picture, however. This participant does not land evenly: their feet are not aligned and they have a tendency to place their left foot facing outwards and roll onto the inner part of their right foot. This is quite clearly an unstable position, as any slip under the small contact area under the right foot would cause them to lose balance and potentially risk injury. As the power generation is still evenly distributed, this would indicate practice of the motion is required rather than any specific strength training - neither leg is weaker, they just need practice in landing more evenly. Being able to make this distinction demonstrates how this may be easily applied to minimise recovery efforts in training or rehabilitation settings.

It must also be highlighted here that there were three different colours of shoe soles used: red, white, and blue; again, the FTIR waveguide consisted of red light. This would mean there was a significant difference in the coefficient β between these red and white shoes, and the blue ones. The ratio was determined to be ~ 0.9 for white:blue and ~ 10.5 for red:blue. Although the blue soled shoes back-scattered significantly less light, the sensitivity of the camera still meant there was a wide range of individually distinguishable pressure values. In cases where a very high dynamic range is required, however, this may introduce limitations in the available information depth.

4.3 Conclusion

The design and operation of a simple-to-construct imaging platform, based on PMMA FTIR waveguides has been demonstrated. As long as the contacting object was mono-coloured, a USB camera and specifically designed software made capturing the pressure distributions below objects in dynamic situations simple, and this was applied to various exercises. These were common training exercises (jogging, drop jumps, counter-movement jumps) and the high resolution, real-time, data collection allowed for analysis of the participants' ability to perform them. Various inconsistencies in their movement were easily

identifiable in the pressure distributions and total contact load, which was in good agreement with the measurements obtained from a standard set of load cells traditionally used to take these measurements. This detailed pressure distribution information below shoes and feet could prove valuable in numerous treatment and training fields where inconsistencies/injury in the foot or lower body muscles need to be monitored. It could further provide insight into the design of advanced prostheses or footwear.

Bibliography

[1] J. S. Pedley, R. S. Lloyd, P. Read, I. S. Moore, and J. L. Oliver, "Drop jump: A technical model for scientific application," *Strength and conditioning journal*, vol. 39, 2017.

[2] A. Struzik, "Biomechanical characteristics of the countermovement jump," in Springer International Publishing, 2019, ISBN: 978-3-030-31793-5. DOI: 10.1007/978-3-030-31794-2_2.

[3] C. G. Tompkins and J. S. Sharp, "Dual optical force plate for time resolved measurement of forces and pressure distributions beneath shoes and feet," *Scientific reports*, vol. 9, 2019. DOI: 10.1038/s41598-019-45287-9.

[4] L. Yin, D. Sun, Q. C. Mei, Y. D. Gu, J. S. Baker, and N. Feng, "The kinematics and kinetics analysis of the lower extremity in the landing phase of a stop-jump task," *The open biomedical engineering journal*, vol. 9, 2015.

[5] K. Hofstetter, C. Grohs, J. Eberhardsteiner, and H. Mang, "Sliding behaviour of simplified tire tread patterns investigated by means of fem," *Computers Structures*, vol. 84, 2006. DOI: https://doi.org/10.1016/j.compstruc.2006.01.010.

Chapter 5

Traction Imaging Of Rotating Polygons

5.1 Experimental Methods

The experiment detailed here used the traction imaging device outlined previously. To take the most advantage of the device's unique ability to measure in-place traction forces in two dimensions, simple two dimensional shapes were analysed under two dimensional motion: rotating polygons. The polygonal pucks used in this experiment have been shown again in figure 5.1. These pucks were 3D printed in red PLA, with a resolution of 0.4 mm in x and y, and a z resolution of 0.12 mm. Two scales of polygons were used: one with a 22.5 mm radius, (which was the maximum size of object that would fit in the viewing window of the device), and one uniformly up-scaled to 45 mm (for close-up analysis of sections of the shapes). A constant contact load of 0.69 MPa was maintained throughout the experiments, by loading the pucks with lead masses, and rotation was achieved by turning handles attached to the pucks by hand. The contact area of each puck varied slightly, so the contact pressure had to be manually adjusted based on the calculable contact area. However, this was always within the pressure ranges tested in the calibration, where the traction results were independent of contact load. Images were captured at 30fps. The experimental results were compared to the previously outlined ABAQUS simulation. The PLA had a Young's modulus of approximately 4.1 GPa [1], so the pucks were effectively rigid compared to the traction platform.

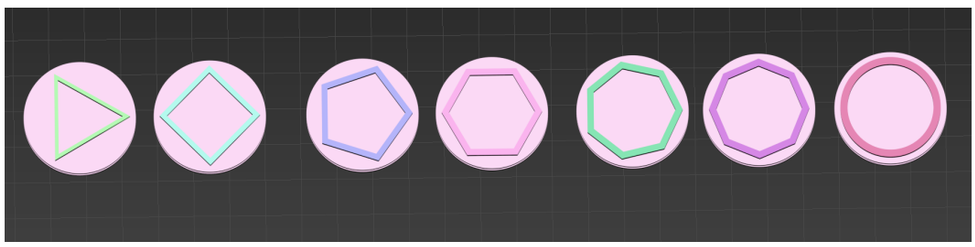

Figure 5.1: All patterns used in rotational measurements. The traction pattern consists of various polygonal shells, with increasing numbers of sides. For the pucks with 22.5 mm radii, the shell thickness was 1 mm and the radius of the polygons were 21 mm. The shell thickness was chosen so that they could be approximated as infinitely thin. For some experiments, explained later on, these pucks were also up-scaled to a 45 mm total radius, with a polygon radius of 42 mm and shell thickness 2 mm, respectively.

5.2 Full Scale Rotation Results

The results for each 22.5 mm radius polygonal shell are shown in detail below. As the number of sides (n) increases, the visual differences become less apparent, so only a select few values of n have been chosen to be displayed here. This is due to the resolution limitation of the device, which as illustrated previously, is only 20×20 unit cells across 45 mm. This was determined by the resolution of the camera and size of the dots. Each polygonal shell has a maximum radius r_{Max}, and a minimum radius r_{Min}, which are the radii of largest and smallest circles which circumscribe the shell (respectively).

The comparisons given in this section are qualitative comparisons to what is expected, based on simulations of the setup written in ABAQUS. Exact quantitative comparisons are not possible due to the limitations of the simulations, however the distribution of the features should be identical namely: the stress field under the contact region should increase with distance from the centre of rotation, and outside of the contact region there should be linear decay roughly radial from the nearest contact point, and stresses should be of the same order of magnitude in both the physical experiments and their associated simulations. There are more analytical comparisons when the size of the pucks are increased in section 5.3.

The colour mapping of the following images must also be noted. The displacement of the dots can only be tracked pixel-wise. The maximum possible

displacement is 8 pixels, and a minimum of 0.5, giving this device approximately two orders of magnitude of resolution. By default, the contour plots from the simulation are designed to highlight large variations in stress. Fine detail is generally of much less interest in practical applications, and as such uses uniform mapping to highlight regions over approximately 5 orders of magnitude. In practice, this meant a squared colour mapping highlighted the regions of interest best in the experimental results, and this had to be manually applied to the simulation (as only linear mapping and user defined contour values are possible). This does not affect the results, but is a necessary step in replicating the exact output presented here.

$\underline{n = 3}$

The polygonal shell with the lowest possible circularity ($r_{Max} : r_{Min} = 0.5$) is a triangular shell, and therefore had the largest disparity in shear. Figure 5.2 shows the experimental rotational load is concentrated almost solely in the corners of the object. From a practical standpoint, this is of particular note as it effectively makes this shape no different to a tripod. Shear is then evenly distributed along the sides of the polygons. Only a small portion of the load is distributed anywhere other than the corners. The simulated results are similar: the values fall in the same range, as shown by the coloured contours and the distribution is still focused mainly in the corners. It must be noted that there is some noise present in the simulated results, clearly visible here as there are variations in the maximum values at each corner. There are two main causes for this lack of rotational symmetry, both of which stem from the low resolution. The first, not unexpectedly, is because a triangular contact region is being projected onto a low-resolution square grid, leading to quantisation errors. The second reason is a directional bias, along the diagonal running from the top right to bottom left of the simulations. This is the "working-direction" of the simulation. In each axis (horizontal/diagonal), the simulation calculates interpolation steps from left/top, to right/bottom, starting outside of the contact region. Any interpolation errors will therefore run along this main diagonal. This gives a reasonable way to calculate error on the simulation results, using the variance measured between like-points in the corners, ±9%.

A feature that could be overlooked as a mixture of noise and low resolu-

tion in the experimental device is the apparent gaps in the traction pattern, roughly centred at the middle of each arm of the polygon. Further study, as explained in later sections, determines this to be a feature of the contact mechanics and makes this shape notably unstable - large portions of the surface provide limited to no slip resistance.

Figure 5.2: A picture of the puck (left), simulation (centre), and experimental result (right) of a polygonal shell, with $n = 3$ sides. In the simulated and experimental results, a 0.69 MPa contact load was uniformly applied and approximately $-1°$ to $1°$ of rotation was applied about the centre of the puck face. This face itself was 22.5 mm in diameter. The experimental and simulated results match well, showing shear concentrated in the corners of the puck face and uniformly distributed along each side.

$n = 4$

Increasing the number of sides to $n = 4$ increases the circularity ($r_{Max} : r_{Min}$) significantly, by a factor of 1.41. As expected, this also changes the load distribution substantially. There is still an obvious concentration at the corners, but the sides have begun to take some of the load, shown in figure 5.3. It is also noteworthy that there is more obvious aliasing in the simulated results here, easily noticeable by comparing the corners. The rotational asymmetry is also again noted, this is purely due to the interpolation errors along the main diagonal and demonstrates the effect clearly. In the simulation, this could be mitigated by simply increasing the number and density of nodes, but this is not possible in the experimental results. Without increasing the size of the pucks, this presumably means there is a comparable amount of aliasing in the experimental results. This was part of the reason larger pucks were made.

Figure 5.3: A picture of the puck (left), simulation (centre), and experimental result (right) of a polygonal shell, with $n = 4$ sides. In the simulated and experimental results, a 0.69 MPa contact load was uniformly applied and approximately $-1°$ to $1°$ of rotation was applied about the centre of the puck face. This face itself was 22.5 mm in diameter. The limitations of the coarse-grained setup are shown well in the simulation, as there is notable asymmetry in these results.

$n = 5$

By $n = 5$, it is difficult to identify regions where the load is concentrated. The results, in figure 5.4 show that the shear under each arm is essentially identical to all the others, and to the corners. This is expected to occur as the shapes are very quickly tending towards a circle, where the shear pattern should be perfectly uniform. There is some indication that there is additional detail being masked by the low resolution, most notably in the bottom arm of the simulated puck (where the arm is aligned with the grid and aliasing will be minimal), but experimental and simulated results are still comparable.

Figure 5.4: A picture of the puck (left), simulation (centre), and experimental result (right) of a polygonal shell, with $n = 5$ sides. In the simulated and experimental results, a 0.69 MPa contact load was uniformly applied and approximately $-1°$ to $1°$ of rotation was applied about the centre of the puck face. This face itself was 22.5 mm in diameter.

$5 < n < 255$

A number of pucks in this range were also made and tested, however there was no obvious difference between any of them - at this scale the arms of a puck are only a few unit cells long. They will take up the same number of unit cells until the $n = 8$ case, where the arms will be a minimum of 4 unit cells long. As the width of the shear regions is approximately the same number of unit cells in all data sets, also 4, these are indistinguishable. This is simply a limitation of the device: the circularity is still increasing, and it would be expected that there would still be some change to the shear distributions as a result. However, there were still some variation in the maximum and minimum shear forces in the contact region, which was more obvious when graphed (as was done later).

$n = 255 \approx \infty$

At this physical scale, a 255 side polygon was effectively perfectly circular ($r_{Max} : r_{Min} = 1$), as each individual side was both smaller than the resolution of the 3D printer, and the resolution of the traction platform. The size of each side was calculated as 0.3 mm. As expected and demonstrated in the simulation, the experimental traction pattern is effectively uniform under the contact area, this is shown in figure 5.5. As this should be the perfectly uniform state, this setup serves to demonstrate some of the limitations of the traction device, mainly noise and resolution. Noise of the experimental results was hence calculated from this, once again from the variance of like-points (now along each circular shell), as $\pm 10\%$.

Figure 5.5: A picture of the puck (left), simulation (centre), and experimental result (right) of a polygonal shell, with $n = 255$ sides. In the simulated and experimental results, a 0.69 MPa contact load was uniformly applied and approximately $-1°$ to $1°$ of rotation was applied about the centre of the puck face. This face itself was 22.5 mm in diameter. This examples why all pucks with $n > 5$ sides were visually identical at the available resolution of the device.

Overall trend

At this resolution, the results appear to match what is expected from a simple elastic simulation: the distance in r from the centre of rotation determines the local oscillatory shear within the contact region, outside of the contact region the shear has to decay to zero as $\frac{1}{r}$ [2]. However, the experimental results involve elastic bodies, which are known to have shape dependent friction [3]. Therefore, analysing the experimental cases at a higher resolution should show additional disparities which begin to deviate from the simple elastic case. This was indeed the case, and is detailed below.

5.3 Close-Up Rotation Results

The limited resolution of the traction device meant that it was not possible to probe the complete area under the rotating polygonal pucks in detail, so larger versions were made. Each new puck had a radius of 45 mm, and all dimensions were scaled proportionally to the smaller pucks.

These new pucks were larger than the imaging area of the traction device, so some caveats had to be made. Using the lithophane effect explained previously, each puck was arranged so that a minimum of one corner and half of each neighbouring side was visible to the camera. Given each polygon will be radially symmetric as long as the contact and rotational loads were uniformly distributed, this visible surface segment would represent the rest of the available surface. Each half-side is referred to as the "front" and "back". This is determined by whether this half preceded or followed a corner, in the direction of motion along the θ axis. For clarity, this arrangement has been described in figure 5.6.

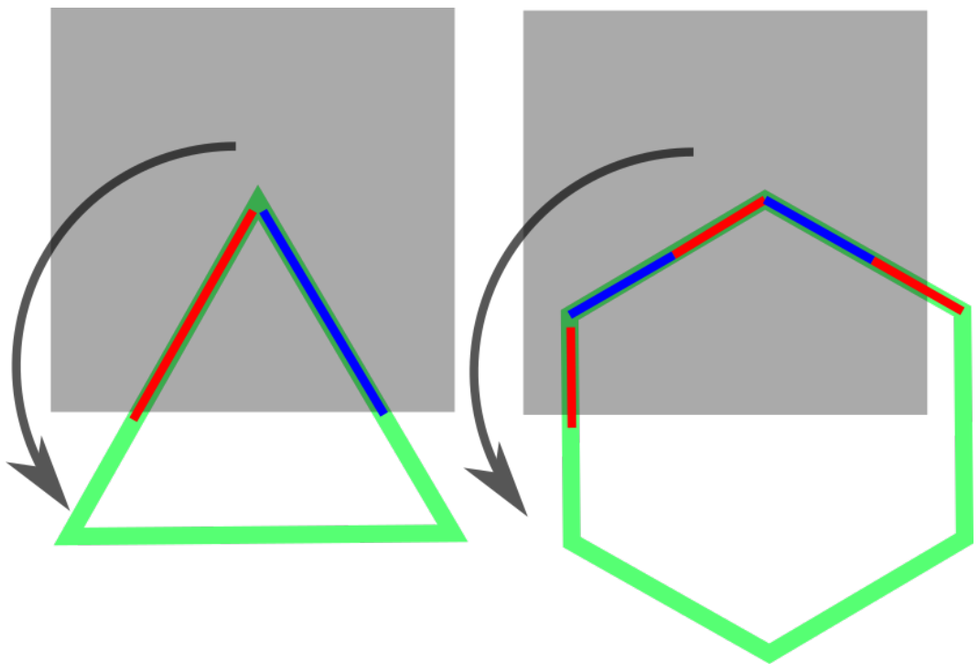

Figure 5.6: An illustration of how the pucks that were larger than the viewing window were arranged, to maximise the non-repeating area that was imaged. Here, example polygons of equal radius but varying number of sides are illustrated in green, and the viewing area of the camera is highlighted in grey. The area of the polygons defined as the "front" are further highlighted in red, while the "back" portions are in blue. The black arrow shows the direction of rotation. The pucks were positioned such that a minimum of one front section and one back section were visible. These could not always be along the same arm (as the arms were longer than the 45 mm-wide viewing window allowed). Assuming radial symmetry, this is unimportant, as each arm should experience identical traction distributions.

At these higher resolutions, additional features became obvious. Specifically, there was a build up of oscillatory shear along the front of the rotating body, and a noticeable lack of shear behind it, in the direction of motion. This is illustrated in figure 5.7 below. The direction of motion has been added to the image, as an arrow, and the outline of the contact area added for clarity. In this shear map, there is a high level of shear surrounding the corner in the top-centre of the image, in regions where the puck is not making contact with the material. A full arm that surrounds this corner is not visible, so the "behind" area precedes the corner, situated in the lower-centre, as circular symmetry means this should look the same as behind every other corner. This was proved simply by rotating the puck and repeating the measurement. The area behind the puck becomes visible to the camera approximately 40% of the way along the length of the front side in the image (ie the first 40% is out of frame), when measured from the corner that is out of view of the camera. The visible length of the back is also approximately 40%, meaning there is little

to no lost information from this arrangement and they can be considered a matched pair. Changing the direction of the rotation changes the direction of the shear build up, so that it is always at the front of a corner in the direction of motion, which gives a starting point to explain what is going on.

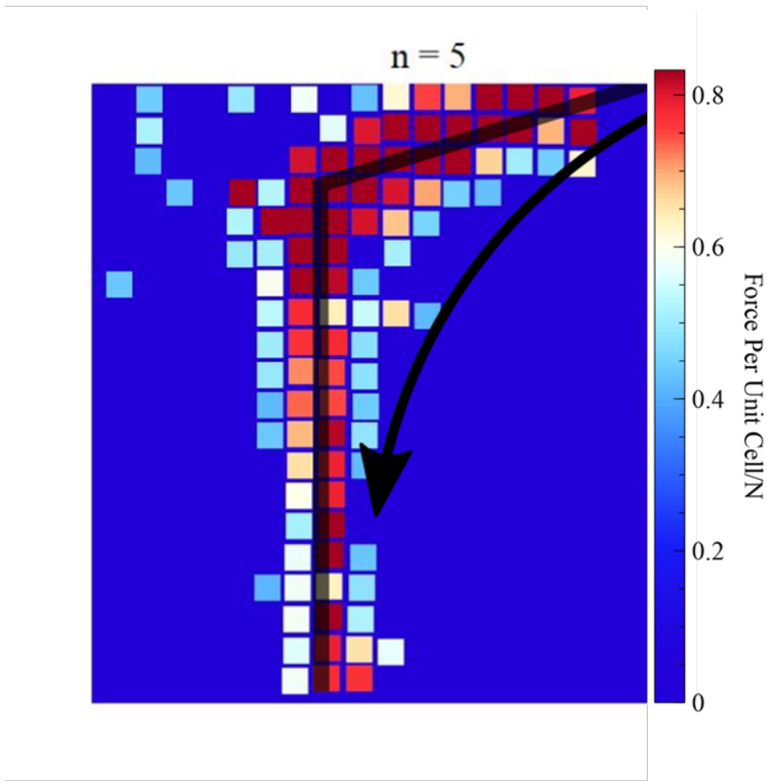

Figure 5.7: A close-up view of the traction forces at one of corners of a 5 sided polygon, under rotation, with a contact load of 135N. A puck with an external radius of 45 mm was used to simulate a close-up view, as the distance to the camera and density of the dots in the traction layer were both fixed. The scale was chosen so that only the largest non-repeating section of the contacting polygon was visible to the camera; given radial symmetry and a uniform load distribution, all equivalent areas should give equivalent traction results. The section of the polygon in view of the camera has been overlayed on the traction map, and the direction of motion indicated with an arrow. The primary observation, which differs from simple-elastic considerations, is that the concentration of shear at the corner is greater behind it than in-front (with respect to the direction of motion). Under simple elastic considerations these regions would be identical.

Other work has previously shown that the material under the 2D cross section of sliding soft objects tends to bunch at the leading edge of a sliding body, likely due to the material undergoing local slip and buckling, and stretch out at the tailing edge [3], [4]. This allows greater amounts of stress to build up in front of the sliding body than would be expected otherwise, and varies depending on the width of the leading edge.

In the rotational setup shown here, the direction of motion is in the θ di-

rection, and therefore the stress build up will depend on the width of the polygon in the direction perpendicular to this: the r axis. The width of the leading edge of a polygon is calculable with equation 3.9, and is maximal in the corners. The regions that are in the rotational shadow of the corner are therefore the tailing edge, which gives the directional dependence.

Repeating these rotational experiments and capturing shear maps over multiple pucks of different values of n gives the unsurprising result that the scale of this leading edge effect decreases as the number of sides increases (i.e the width of the leading edge decreases), eventually becoming 0 as $n \to \infty$, and allows the effect to be quantified.

To quantify the change in the leading edge effect with n, the maximum and minimum value of the shear under the contact region of a puck were selected by eye from a random frame in a video of each of the different pucks, and then a ratio of them calculated. It should be noted that the specific value of the overall load applied in each frame was irrelevant, both because they were plotted as a ratio and because there is no known (or observed) hysteresis in the load distribution below the limit of slip. This ratio was then plotted against the circularity of the polygons. Here, circularity (χ) has once again been defined as the ratio of the length of the minimum and maximum radii of a circle circumscribing the polygon. In the simple elastic case, the load under any point of the contacting body will scale as $r\theta$. Given a constant θ, it will therefore scale as r. So the ratio of the maximum and minimum r, which gives (χ), would also give $\frac{F_{Min}}{F_{Max}}$ and a plot with a unitary fit (i.e $y = x$). In the experimental case here, shown in figure 5.8, this is not the case.

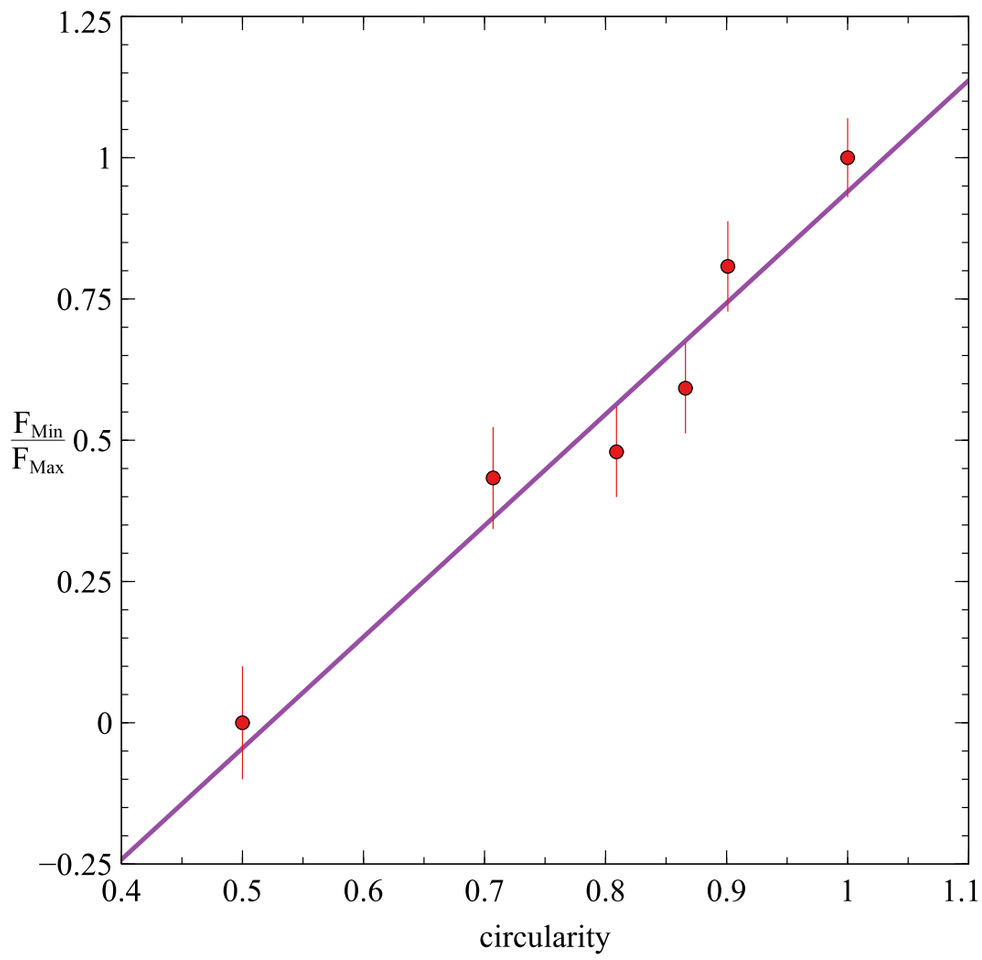

Figure 5.8: A graph of the ratio of the maximum and minimum forces observed under a rotated contacting object as a function of its circularity ($\chi = \frac{r_{Min}}{r_{Max}}$). Under simple elastic conditions, this graph would be unitary, ie $\frac{F_{Min}}{F_{Max}} = \chi$. However, the observed leading edge effect causes this to become $(1.97 \pm 0.6)\chi - (1.03 \pm 0.3)$. This is driven by how wide the leading edge of the rotating object is, compared to the minimum in the radial direction, which increases as circularity decreases. Once the object is perfectly circular, this effect is no longer present and the force distribution becomes unitary. The errors come from the quantisation of the displacement of the dots, by the pixel size of the camera. Circularity values below 0.5 are non-physical, as they require a regular polygon with $n < 3$ sides, so values of $\frac{r_{Min}}{r_{Max}}$ are also non-physical here.

Due to the known shape dependence of friction, said figure shows a very different gradient from what would be predicted from simple elastic considerations; here the fit was calculated to be $y = (1.97 \pm 0.6)x - (1.03 \pm 0.6)$. Errors are propagated through from the noise in the individual strains, determined in the previous section. That is to say, this graph is showing that the distribution of shear under a rotating body is different from the simple elastic case, and is dependent on the circularity, or the *relative* width of the leading edge in the radial direction. This can be used to find an analytical correction factor which can be applied to the simulations used to model these situations.

5.4 Developing a Corrective Factor For Forces

From the graph in figure 5.8, it was shown that the ratio between the maximum and minimum force follows the expression $m\chi + c$, where χ is the circularity of a given polygonal shell. In this modified case, it can be assumed that F_{Min} has decreased by some amount δF_{Min}, and F_{Max} has increased by δF_{Max}:

$$\frac{F_{Min}}{F_{Max}} \rightarrow \frac{F_{Min} - \delta F_{Min}}{F_{Max} + \delta F_{Max}} = m\chi + c. \tag{5.1}$$

Multiplying through by the denominator gives

$$F_{Min} - \delta F_{Min} = (F_{Max} + \delta F_{Max})(m\chi + c). \tag{5.2}$$

And, by definition $\chi = \frac{F_{Min}}{F_{Max}}$. Therefore, the factor of χ can be brought to the front of the right hand equation by substituting $\frac{F_{Min}}{\chi}$ for F_{Max}:

$$F_{Min} - \delta F_{Min} = \frac{1}{\chi}\left(F_{Min} + \frac{\delta F_{Max}}{\chi}\right)(m\chi + c)\,. \tag{5.3}$$

Simplifying for readability then gives:

$$F_{Min} - \delta F_{Min} = \left(F_{Min} + \frac{\delta F_{Max}}{\chi}\right)\left(m + \frac{c}{\chi}\right). \tag{5.4}$$

Expanding out the brackets and rearranging to make δF_{Min} the subject gives the final expression

$$\delta F_{Min} = F_{Min} - F_{Min}m - \frac{F_{Min}c}{\chi} - \frac{\delta F_{Max}m}{\chi} - \frac{\delta F_{Max}c}{\chi^2}. \tag{5.5}$$

This expression only has one set of real, non-zero, solutions:

$$\delta F_{Min} = F_{Min}(1 - m + c\frac{1}{\chi}) \tag{5.6}$$

and

$$\delta F_{Max} = 0. \tag{5.7}$$

The physical interpretation of this is that, for a given degree of rotation, the minimum shear within the contact region decreases, while the maximum remains the same. This has some important implications. Primarily, when contacting a soft surface, the load that can be maintained before slip and

failure of the interface is less than would be predicted in a general simulation. In the case of lower-order polygons, this is can be significantly different: up to a 66% decrease in the case of an $n = 3$ shell. It must also be noted that, in this case, a large portion of the contact interface does not contribute to distributing the traction load and it is effectively no different to a tripod. These corrections likely are dependent on the relative Young's moduli of the surface and the contacting object, but this cannot be experimentally confirmed without remaking waveguides of various stiffness values. They will, however, be independent of other physical properties such as scale, so long as the object is macroscopic, so that the various assumptions about its surface properties (such as those outlined in the Greenwood model) still hold. This correction can easily be reapplied to various mechanical situations as a result.

So far, a modification to the maximum and minimum forces experienced under a rotating polygon has been developed. These are useful by themselves in predicting the force distributions, however it would be ideal to be able to predict the entire traction distribution, instead of simply the extremes. The ideal way would be to simply develop an FEM model to do so, however the software required to do so is often closed source and there was no time to develop a complete alternative. Instead, a simpler alternative was found. To understand how, some knowledge of the steps involved in FEM is required.

An FEM solver is essentially an accurate method of interpolation, where multiple steps are taken to reduce the errors from propagating known quantities (strains, in this case) at well-defined points, to unknown quantities at some other given point. As discussed, these simulations are set up by initially applying a set of distributed forces to a defined surface, and the stress distribution in the surface can then be computed. These loads are positioned along uniformly distributed points in the surface, called nodes, and are used to interpolate the strains in the remaining regions of the surface. This is achieved by solving partial differential equations for the strains in the surface, and is known to be computationally intensive even for modern hardware [5]. As such, the surface is instead divided into course-grained tetrahedral/cuboids,

and a shape dependent integration function used to calculate the points at which stresses can be defined (referred to as integration points) to minimise artefacting. This is a complex optimization problem, which, in practice requires hardware-level knowledge of the (often proprietary) algorithms and the errors they propagate. However, it also identifies one step where the displacements are well defined without this: directly under the contacting interface. If only this region is studied, then the steps required to simulate the problem are simplified significantly.

5.5 Modified Traction Simulation

In this section a simple simulation is designed to demonstrate how the modification to the traction forces can be applied to simulated examples. In order to eliminate a large amount of the optimisation and complex steps required to make an accurate simulation, a number of constraints had to be added. As in the ABAQUS simulation, it was assumed that the traction load was applied directly to the surface and there is no provision for slip. Secondly, only the region of the surface directly under the contact area was considered. This was the region in the experimental data with key details the simulation was meant to emulate. Not simulating the strains outside of this area eliminated the need to solve the partial differential strain matrix normally required, and the strains could be directly coupled to the displacement of the surface at some radial distance r, caused by a rotation $d\theta$.

The mathematical description of polygonal shells, previously outlined in equation 3.9, was used once again in this simulation. The resolution of the simulation was also increased substantially from the previous ABAQUS simulation (10^2 points versus 10^6 points). This eliminated the need for redistributing the nodes to minimise aliasing. This was computationally viable with the MATLAB simulation and not the ABAQUS simulation because of the extra processing required when solving the differential equations.

As an initial step, the simple elastic case was considered: the load under each point was proportional to $rd\theta$, and this was compared to the equivalent simple elastic simulations made in ABAQUS, with the same elastic modulus.

A shell thickness of 50 arbitrary units was used in the set of examples given in figure 5.9.

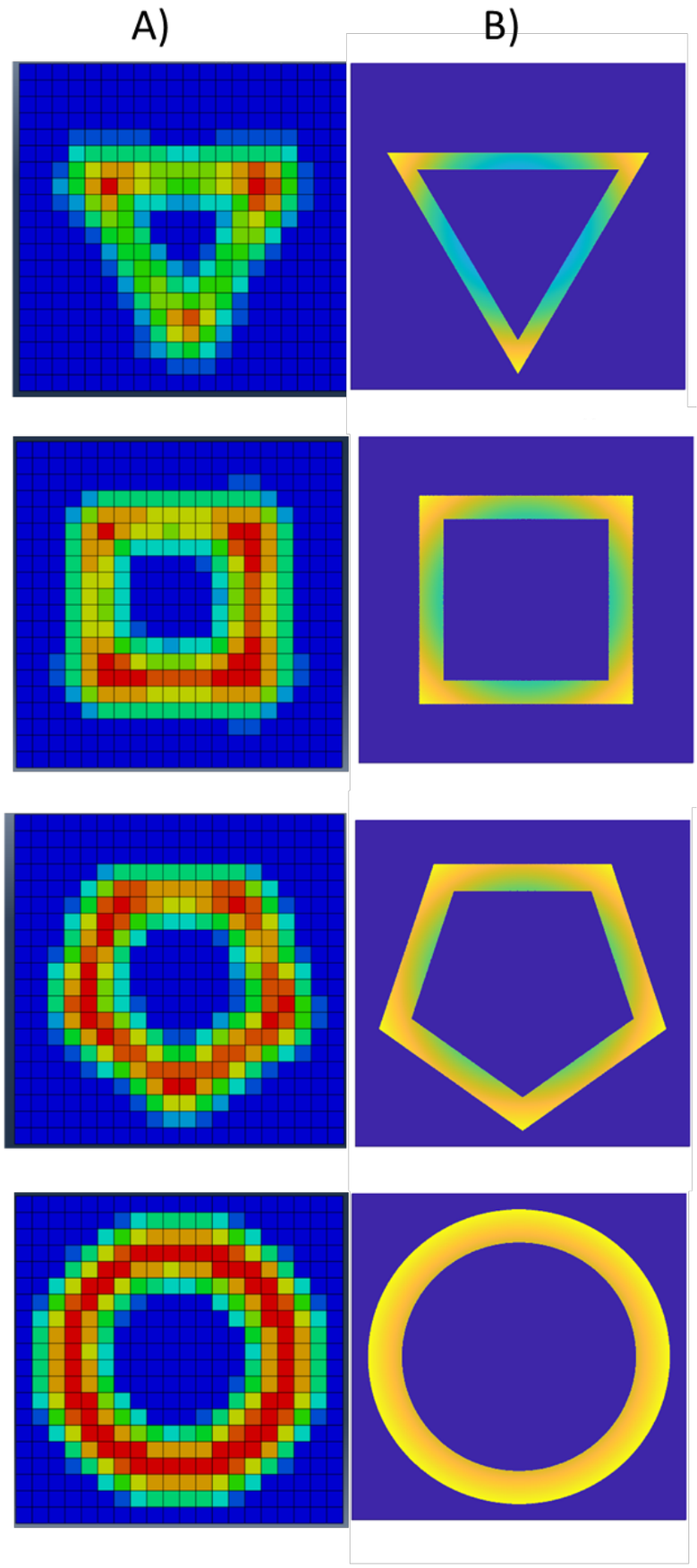

Figure 5.9: A comparison of the ABAQUS (a) and MATLAB (b) simulations used for analysing the traction distribution under a rotating polygonal shell. Both examples only consider simple elastic arguments, and results compare favourably. In the MATLAB simulation, only displacements directly under the contacting object are considered, to greatly simplify the mathematics required. The ABAQUS simulation calculates the strains in the entire plane, although this necessitates lower resolution.

The next step was to modify this simulation to take into account the expression for δF_{Min} in equation 5.6. This was achieved first by calculating the value of δF_{Min} expected, and converting this to what displacement it corresponds to at a given radius from the origin D_r, in the $\hat{\theta}$ direction. Using the same arguments that were used to develop the simple elastic theory [6], [7], this additional displacement must also be continuous and decay as $\frac{1}{r}$, such that $\delta F_{Max} = 0$. It is therefore simply a matter of computing this decay as a function of distance between a corner (where δF_{Max} is situated), and the centre of a side (where δF_{Min} is situated). Based on experimental observation, this force is compressive at the leading edge, and tensile at the rear edge. This gives the direction dependence, i.e. the sign, of δD_r. Applying this to the simple elastic case gives the modified displacement field.

A comparison of this modified displacement field, compared to the simple elastic case is shown in figure 5.10. It can clearly be seen that, by adding in this corrective factor, some of the features observed in the experimental case are recovered. Firstly, the feature exclusive to the $n = 3$ case is recovered: there is a large region where the displacement is 0, where no traction force is being transferred to the surface the polygon rests on. This feature is also not present in higher order polygonal shells, as required by the experimental observations. The other feature is the disparity in the lengths of the leading and rear edges. The leading edge region is longer and decays slower than the rear edge, which was also observed in the experimental case. This would align with the conclusion that this leading edge effect is caused by a compressive force acting in the direction of motion of the object, causing the surface to "bunch-up" at the leading edge. The faster decay in the rear edge is then the surface being stretched out and pulled, as it is not sliding under the puck. The evolution of this simulated effect is compared to the experimentally observed case in figure 5.11

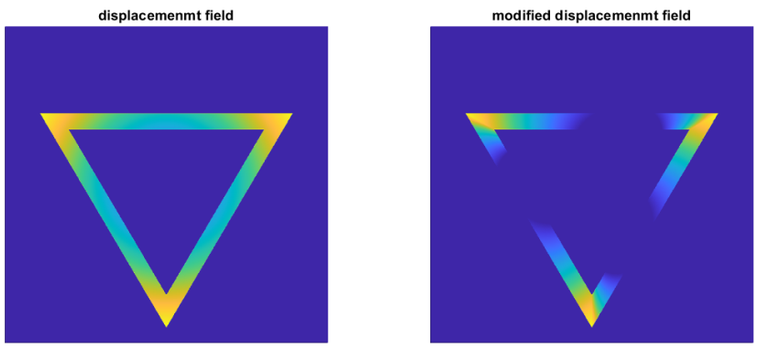

Figure 5.10: The two unmodified and modified displacement fields calculated under a contacting puck of $n = 3$ sides, which experienced a rotational displacement of 1°. The displacement values, and scale of the polygon, are in arbitrary units. This replicates a number of the features present in the higher resolution experimental results. Firstly the region where no traction load is being distributed by the puck is clearly present in the centre of each arm of the polygon. Secondly the disparity in the length of the leading and rear edge regions observed are also present: the leading edge region is longer, and decays much slower, due to a build up of compressive forces at the front of the polygon (in the radial direction).

A complete example of how this simulation compares to the key experimental cases is shown in 5.11 below. It can be seen that the simple elastic case is recovered as the number of sides increases, as expected. No features present appear to contradict the experimental observations, although their low resolution once again makes this comparison limited.

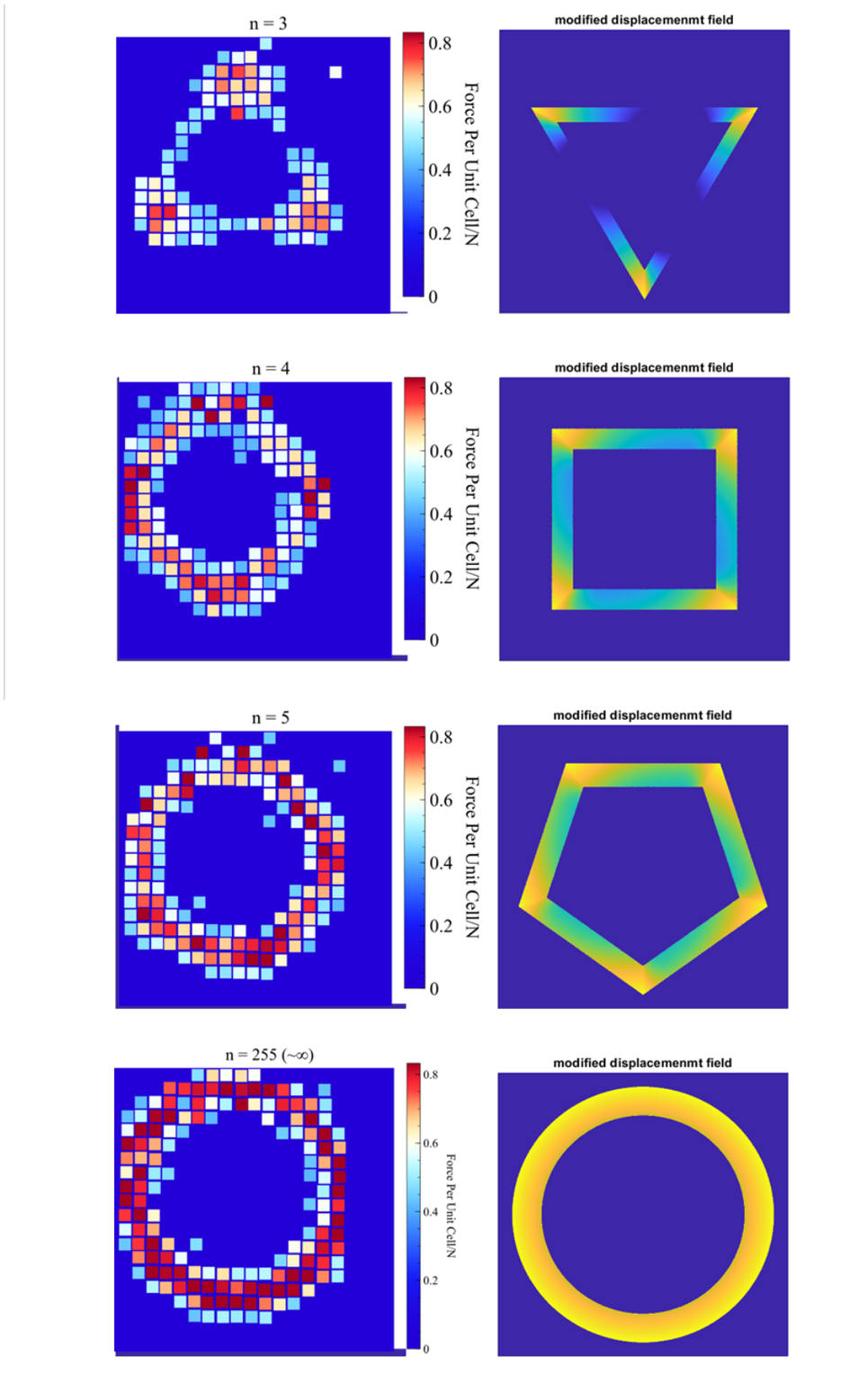

Figure 5.11: The complete evolution of the modified displacement field calculated in the MATLAB simulation, compared to the key experimental cases. The evolution of the observed features are in line with what is expected experimentally and the effect decreases as the circularity of the polygons increases. This simple result is encouraging and could be added to more complex simulations to help improve their accuracy when modelling these kinds of rotational problems.

5.6 Conclusion

The design and development of a prototype traction sensor has been outlined here, which is capable of directly measuring the two-dimensional in-plane shear between the sensor and a contacting object. Using this device, the traction distribution between various sliding chevron patterns and rotating polygonal shells has been analysed, analogous to the tread patterns used in shoe soles and tyre treads. This has resulted in various new understandings of friction between elastic and inelastic materials.

The traction distribution below the rotating polygons was analysed and compared to a standard simulation using the commercial software ABAQUS. It was found that there was a leading edge effect, which caused asymmetry in the traction distribution, as had previously been observed in one-dimensional cases. Uniquely, this redistribution acts along the direction of rotation and is dependent on the width of the cross section, or the circularity of the object. This means redistribution of forces varies with the number of sides of the polygon, independent of scale, with the minimum force decreasing with the circularity (χ) by $F_{min} \rightarrow F_{min} - F_{Min}(1 - m + c\frac{1}{\chi})$. Based on experimental results $m = 1.97 \pm 0.06$ and $c = 1.03 \pm 0.03$.

This not only demonstrates how the device itself can be used to image complex strain fields, useful for various design and sports science fields, but provides a further understanding of elastic properties that can then be applied to simulation. This corrected force was applied to a simple traction simulation written in MATLAB, and the results compare favourably.

Overall, the use of the traction imaging platform has given unique insight into the force distributions between elastic and inelastic bodies and provided insight into the cause of the complex shape dependence known to exist at these contacting interfaces. Corrections to current simulations and theoretical models are proposed, increasing their ability to quantify physical phenomena.

Bibliography

[1] V. Pinto, T. Ramos, S. Alves, *et al.*, "Comparative failure analysis of pla, pla/gnp and pla/cnt-cooh biodegradable nanocomposites thin films," *Procedia Engineering*, vol. 114, 2015. DOI: https://doi.org/10.1016/j.proeng.2015.08.004.

[2] A. C. Fischer-Cripps, *Introduction to Contact Mechanics*, Second Edition. Springer, 2007, ISBN: 978-0-387-68187-0.

[3] J. Hale, R. Lewis, and M. J. Carré, "Rubber friction and the effect of shape," *Tribology International*, vol. 141, 2020. DOI: https://doi.org/10.1016/j.triboint.2019.105911.

[4] K. Hofstetter, C. Grohs, J. Eberhardsteiner, and H. Mang, "Sliding behaviour of simplified tire tread patterns investigated by means of fem," *Computers Structures*, vol. 84, 2006. DOI: https://doi.org/10.1016/j.compstruc.2006.01.010.

[5] *COMSOL Multiphysics Cyclopedia*, Ninth Edition. COMSOL, 2017.

[6] A. E. H. (E. H. Love, *A treatise on the mathematical theory of elasticity*, 4th rev., enlarged ed. Dover, 1944, ISBN: 0486601749.

[7] S. Timoshenko, *Theory of elasticity*, 3rd ed. McGraw-Hill, 1970, ISBN: 0070647208.

Chapter 6

Traction Imaging Of Translated Chevrons

6.1 Experimental Methods

The experiments outlined here were designed to be extensions of the standard traction experiments usually undertaken with photoelasticity [1], [2], using the matrix-based traction imaging platform previously outlined. As explained before, the standard experimental geometry requires bringing objects with a uniform cross section into intimate contact. The device built here, however, has already been shown to not have this limitation. As such, these translation experiments have been extended, and simple shapes with a non-uniform cross section have been analysed. These were chevrons with varying internal angles, which have been shown again in figure 6.1.

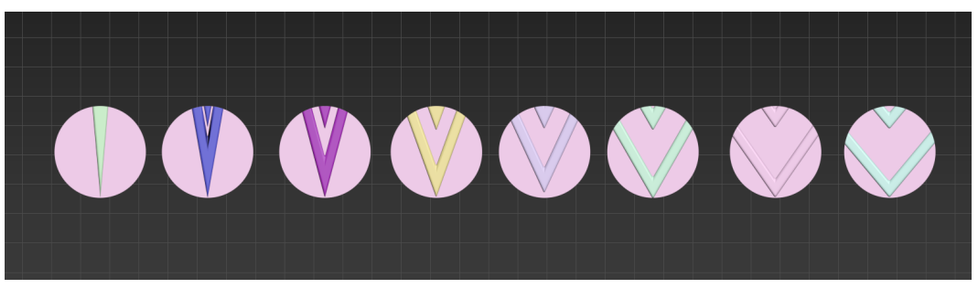

Figure 6.1: The chevron patterns used in translation measurements. Each puck had a radii of 22.5 mm and had two 3 mm thick chevrons, with a peak separation of 40 mm. The angle of each chevron varied between 15° and 90°. Smaller angles were not possible, as the arms of the chevrons began to merge together. Larger angles would effectively be the same as the puck/its motion being reflected along the y-axis, which was an easier way to study these effects.

These pucks were printed in red PLA, with a resolution of 0.4 mm in x and y, and a z resolution of 0.12 mm. 3 different alignments of the chevron and

direction of motion were analysed, and the associated nomenclature has been explained in figure 6.2, for reference. The PLA had a Young's modulus of approximately 4.1 GPa [3], so the pucks were effectively rigid compared to the traction platform.

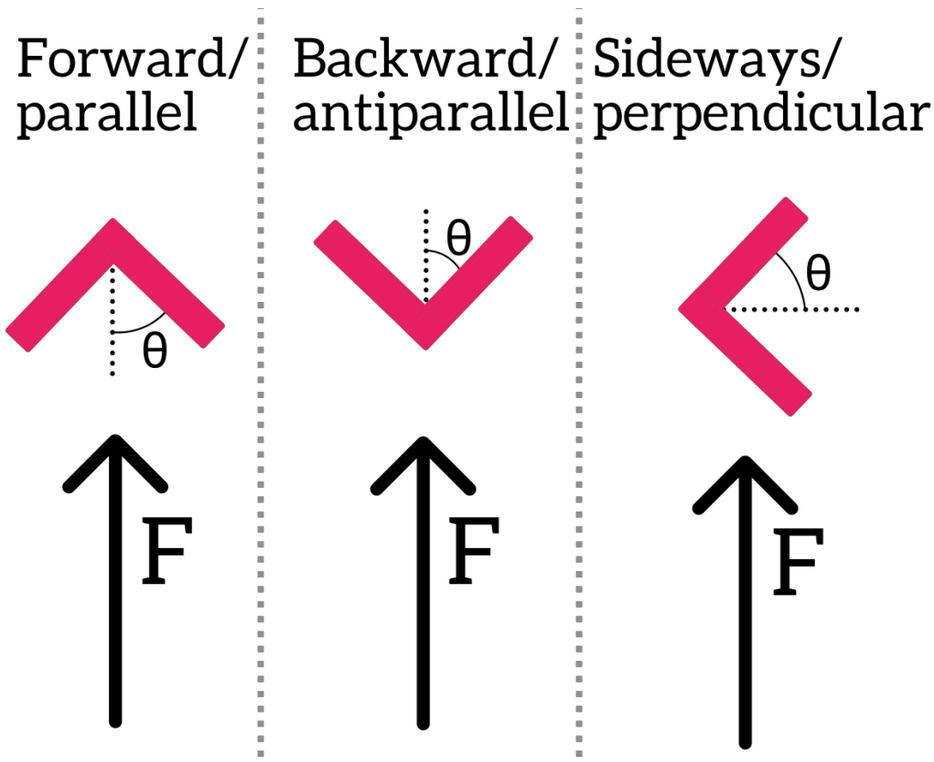

Figure 6.2: A visual description of the nomenclature used in the following experiments. In the first set, the chevron (red) is pointing in the same direction it is being pulled in (the direction of the applied force being labelled F). This is referred to as the forward or parallel case (i.e. where the chevron point is parallel with the translation vector). The next case is the backwards or anti-parallel case, where the chevron is now facing in the opposite direction to the direction of the applied force. The final case is the sideways/perpendicular case. The point of the chevron is now 90° out of plane to the direction of applied force. The "internal angle" (labelled θ in this figure) of a chevron in this chapter is the angle each arm subtends from the normal, so the right angles pictured here have an internal angle of 45°.

All pucks maintain an approximately constant contact pressure of 0.69 MPa, and are translated by a steel cable wrapped around the circumference of the puck. This is then attached to a calibrated load cell, which measures the force of translation. Images of the dots under the puck were captured at 30fps over 5 seconds, and converted into shear maps using the previously described code.

At this point in the experiment, it had already been shown that the shear modulus was independent of contact load, for the range of contact pressures studied. From a microscopic perspective, the load applied to the puck can be

transferred in one of two ways: If the local coefficient of friction is sufficiently high, it will be transferred as a shearing force into the contacting surface. Otherwise, the force will break the interfacial bonds and cause local micro-slip. If the same method that was previously used to calibrate the shear modulus of the platform using a cylindrical puck is applied to this situation, then the measured (apparent) shear modulus will not be the actual shear modulus of the material, as micro-slip is occurring. Therefore, a decreased apparent shear modulus corresponds to an increased coefficient of friction; the surface is easier to shear because a greater proportion of the load is going into shearing the surface rather than breaking the interfacial bonds.

As such, the shape dependence of the coefficient of friction was analysed using the same method as previously used to find the shear modulus for a cylindrical puck. The value calculated from this method has been named the apparent shear modulus, for convince, due to the identical method of obtaining the data and the fact that it is not inherently distinguishable from the actual shear modulus during experimentation. The distinction must be made clear however: the shear modulus is the actual material property, the *apparent* shear modulus is what it appears to be when micro-slip is occurring. This was then plotted against the internal angle of the chevrons.

6.2 Chevron Pattern Results

In order to analyse the traction distributions created by the herringbone patterns commonly used in shoe soles and other grip-structures [4]–[6], the patterns were reduced to their simplest form, a single chevron, and analysed under various angles of motion described in figure 6.2. These chevrons were 3D printed from PLA with a Young's modulus of approximately 4.1 GPa [3], so they were effectively rigid compared to the traction platform, and were 22.5 mm in radius. The directions of the applied motion were determined based on where the peak of each chevron was pointing: forward motion was defined as the chevron pointing in the direction of motion, in backward motion it was pointing against the direction of motion, and in sideways motion the chevron was pointing perpendicular to the axis of motion. This was applied to a set of chevrons with the internal angle varying from 10° to 90° . The contact area

of each puck varied slightly, so the contact load was modified to maintain an approximately constant contact pressure of 0.69 MPa. The first set of data taken was for forward motion.

Forward Motion

Sample traction force maps taken when the chevron pucks were pulled forwards are shown in figure 6.3, evolving with the internal angle of the chevron.

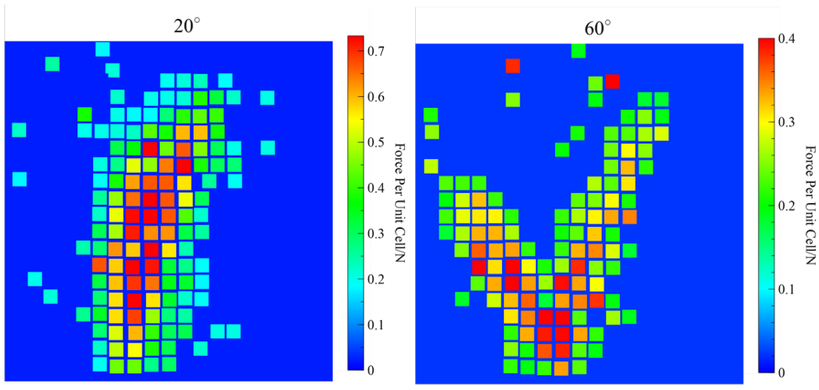

Figure 6.3: Example images of the evolution of the normalised traction force distribution under chevrons with different internal angles (20° and 60°), which are highlighted above each image, while they are pulled in the direction of the chevron point. Each cylindrical puck which circumscribed the chevrons had a radius of 22.5 mm and a contact pressure of 0.69 MPa.

The more interesting analysis comes from measuring the normalised apparent shear modulus. As explained in the method, the relative change in the shear modulus will couple to a change in the net coefficient of friction. It was also already known that changing the internal angle of the chevron changes the net coefficient of friction but has not been characterised (to this authors knowledge). A plot of the relative shear modulus as a function of internal angle (in radians) is shown in figure 6.4. Errors on the data are due to confidence bounds on the initial fits used to find the shear modulus, following the same method as in the calibration steps in chapter 3.

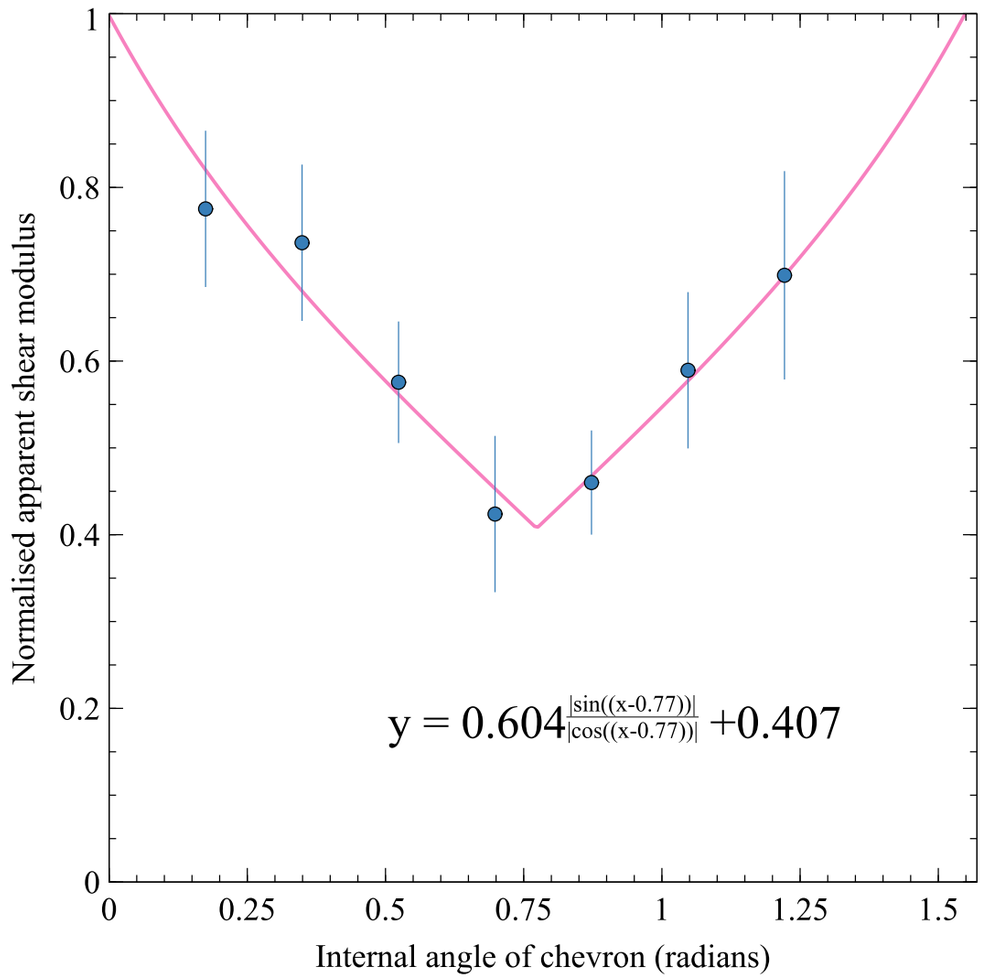

Figure 6.4: A plot of the normalized apparent shear modulus measured when a chevron patterned puck is translated along the traction platform, as a function of the internal angle of the chevron in radians. The direction of translation was parallel to the peak of the chevron. Contact pressure was kept uniform at 0.69 MPa. Errors are due to the confidence bounds used to calculate the fits for the relative shear modulus. The graph shows the normalized apparent shear modulus scales as the ratio of the sine and cosine of the angle subtended by the arms of the chevron from the normal axis (half the internal angle of the chevron). As expected, this is centred on approximately 45°/0.79 rad (actual value 44(±2)°/0.77(±0.04) rad), meaning the coefficient of friction is maximised with this shape. This also tends to 1 (0.99 ± 0.05) at an internal angle of 0° and 90°/1.57 rad. This is also expected, as the chevron is simply a sliding block at these angles.

As would be expected from qualitative observations, the shear modulus is minimized at an internal angle of 45° (44(±2)°). Mapping these data out as a function of the internal angle gives additional information. The relative change in the shear modulus scales with the ratio between the sine and cosine of the angle subtended between the arm of one chevron and the normal, i.e the internal angle. It scales between some minimum value and 1 (0.99 ± 0.05) when the internal angle is 0° and 90°, recovering the value expected from a sliding cuboidal block.

It must also be noted that this demonstrated the shape dependence of the coefficient of friction is not dependent on the shape of the elastic object itself, but on the shape of the interface between the two contacting bodies. This is important, as it means any designed object (say a tyre) must consider the elastic properties of the surface it is in contact with, as well as the properties of the object itself. Based on these observations, a simple theory as to the origin of the shape dependence is proposed.

The proposed theory is that compressive strain at the interface is driving the shape dependence, in a similar way to the weight distribution between a pair of angled beams with a mass at their peak. If the load is considered to be centred on the peak of the chevron, shearing it will compress the elastic surface and transfer the load to neighbouring regions. As the mechanical properties are homogeneous, the proportion of the total load (L) distributed in x will scale as

$$\frac{L}{2}\left|sin(\theta)\right| \tag{6.1}$$

for each arm of the chevron, where θ is the angle subtended between the arm of the chevron and the normal axis. The proportion distributed in the y axis will scale as

$$\frac{L}{2}\left|cos(\theta)\right|. \tag{6.2}$$

This setup is illustrated in figure 6.5 a) for clarity.

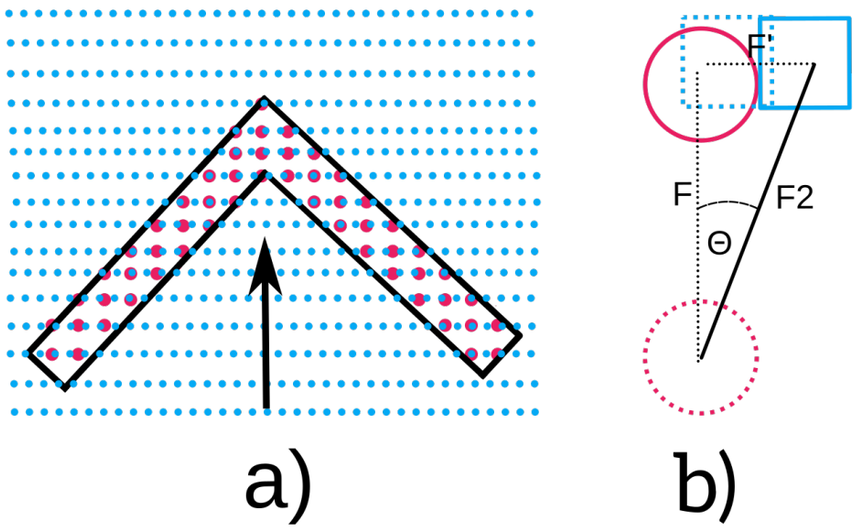

Figure 6.5: An illustration of how compressive strains would be distributed at the interface between a chevron. The overall problem is illustrated in panel a), showing the redistribution of force along each axis. This is governed by the angle of each arm from the normal axis (y), which is the internal angle θ. It is proposed that this is due to the collision of asperities in the materials: asperities in the surface which are in contact with the chevron (red) will be sheared, non-contacting asperities (blue) will not. However, if a red asperity is sheared enough that it collides with a blue asperity, then the blue asperity will also be sheared. An illustration of how this load would be redistributed microscopically is shown in b), where the blue asperity is off-axis with the motion of the red asperity. Due to the angle of the chevron, successive points must be pushed out of the way horizontally as the chevron is translated vertically, transferring compressive strain to these points. It must be noted that not all asperities in the elastic layer will make contact with asperities in the chevron, allowing collision between asperities (and therefore compression) within the apparent contact area, hence why this is observed to be a bulk rather than an edge effect.

Effectively, this would only require one alteration to theoretical models (like the Greenwood model) in order to account for this. In these models, asperities are considered far enough apart that they do not interact; an individual contact patch will be sheared until it fails, and the pair of asperities may go on to form new bonds with asperities in the now translated material [7]. What is proposed here is that the elastic modulus of the soft material is now sufficiently low that the bonded asperities may shear and encounter another asperity before the breakage occurs, allowing the additional shear to be shared and redistributed off axis. A natural question now arises: how does translation in one direction lead to off-axis shear?

Consider the interface at the edge of the chevron. For sake of clarity, consider the chevron to be made of points spaced by d equally in the$x$ and y axis. At

the edge of the chevron, there will be a line of points angled θ from the normal axis. The chevron is now translated a distance d in the y axis. From the reference frame of a point within the elastic plane, the edge of the chevron has now moved outwards in the x axis by $dsin\,(\theta)$. If there was a pair of contacting asperities at this position, then asperities within the elastic plane that have not been translated (because they are not in contact with the chevron) must be pushed out of the way to accommodate the pair. This then applies an off-axis shear on the new asperities proportional to the internal angle of the chevron. As work is now being done to translate these new asperities off axis, the overall force required to shear the original asperity to the point of yielding is now higher, increasing the coefficient of friction. For clarity, this is also illustrated in figure 6.5 b). As the real contact area is much less than the apparent contact area of the chevron, this allows non-contacting asperities to be displaced in the bulk of the chevron as well as at the edge, hence the observed bulk effect.

A further simple test which confirms this angular redistribution is to extract the x and y plane shear maps individually in some of the extreme cases. At these extreme cases, the shear should be mostly confined to a set axis, based on the internal angle. This is shown in figure 6.6.

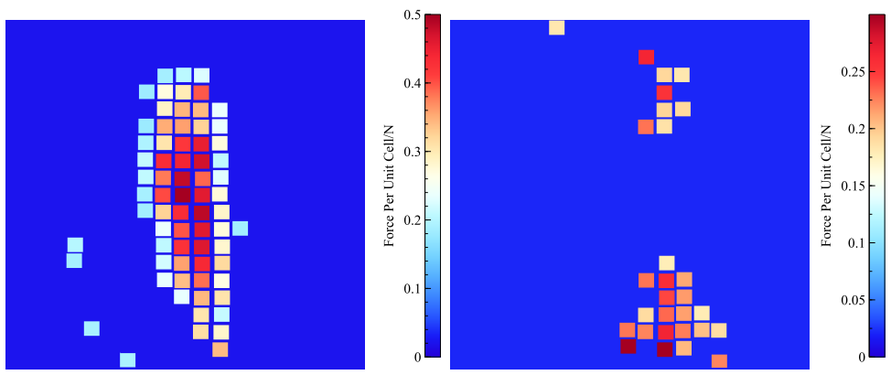

(a) 15° chevron, y strain (b) 15° chevron, x strain

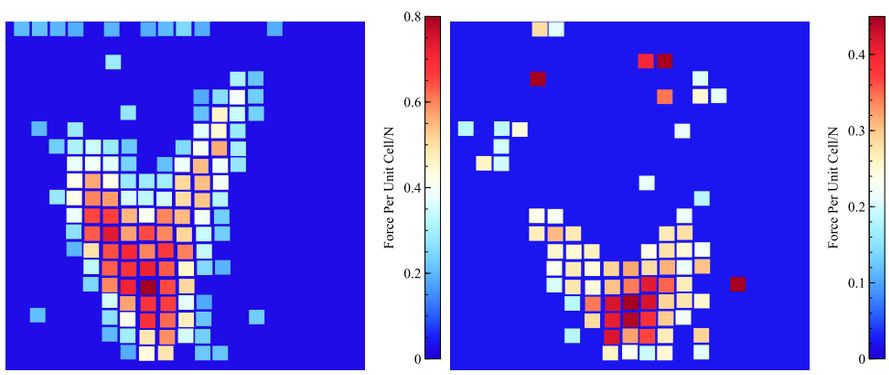

(c) 50° chevron, y strain (d) 50° chevron, x strain

Figure 6.6: Examples of the shear patterns under chevrons with different internal angles (15° and 50°), decomposed into their respective x and y magnitudes. Direction of the applied load is indicated by arrows on each plot. It can be seen that, when the internal angle is sufficiently low, the majority of the strain is in-plane with the direction of translation. By changing the internal angle θ such that $sin\,(\theta) \approx cos\,(\theta)$, there is a significant increase in out of plane shear under the entire contact area of the chevron. This would indicate the load is being redistributed as described.

In figure 6.6, it can clearly be seen that the shear can be split into its respective x and y magnitudes, and the ratio of these magnitudes scale with the appropriate sine and cosine of the internal angle. At small internal angles, the load is almost entirely concentrated in the direction of translation. Increasing the internal angle to approximately 45° strongly splits the load between shear in the x and y directions. This allows a greater amount of load to be redistributed into the surface before slip occurs, increasing the coefficient of friction by only altering the shape of the contact patch. Increasing the internal angle even further decreases the out of plane shear. Using the strain-based arguments outlines above, this is predictable.

This outlines how an elastic material may have a shape dependent coefficient of friction, but how would this fit with current models, as the Young's modulus varies? In mathematical terms, this may be described as follows. For each contacting asperity, it will require the application of a force F to fully separate the contact region. For a Hookian elastic material, with spring constant k, the applied force F will have an associated displacement $x = \frac{F}{k}$. If the linear density of asperities is ρ, then the probability (p) of a sheared asperity colliding with a non-sheared (non-contacting) asperity will be

$$p = \frac{F\rho}{k}. \tag{6.3}$$

After collision, the net applied force will go into both breaking the initial connection, and displacing the new asperity. The material will still yield when the force applied to the contacting asperity is F, with some additional force F' required to shear the new asperity, giving $F \rightarrow F2 = F + F'$. Using a simple trigonometric identity, the value of F' can be described in terms of $tan\,(\theta)$, F, and the probability of the interaction occurring

$$F' = Ftan\,(\theta) \times p = Ftan\,(\theta)\,\frac{F\rho}{k}. \tag{6.4}$$

Therefore, the total applied load $F2$ can be written as

$$F2 = F + F' = F\left(1 + \frac{f\rho}{k}tan\,(\theta)\right). \tag{6.5}$$

This second term then naturally tends to zero as $\rho \rightarrow 0$, or when $k \rightarrow \infty$,

meaning it is only relevant for elastic surfaces with close packed asperities. As friction models such as the Greenwood theory assume low asperity density and high elastic modulus, the standard friction model can still be recovered from this equation.

This kind of shape dependent friction would therefore be expected for any surface with a shear modulus sufficiently low to allow asperities to collide, as long as the required load is low enough to prevent slip. Theoretical modelling exact predictions would therefore require knowledge of the asperity size and distribution, much like regular microscopic friction analysis, with the addition of the shear modulus as an extra requirement.

The theoretical picture described here is also, encouragingly, consistent when the orientation of the chevron is changed.

Backward Motion

Sample traction force maps taken when the chevron pucks were pulled backwards are shown in figure 6.7, evolving with the internal angle of the chevron.

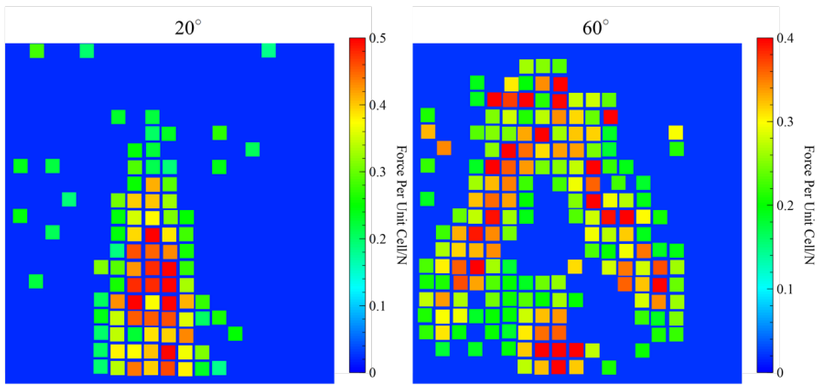

Figure 6.7: Example images of the evolution of the normalised traction force distribution under chevrons with different internal angles (20° and 60°), which are highlighted above each image, while they are pulled against the direction of the chevron point. Each cylindrical puck which circumscribed the chevrons had a radius of 22.5 mm and a contact pressure of 0.69 MPa.

If the cause of the observed shape dependence in the forward case was indeed compressive strain at the interface, then the same should hold true when the chevron is rotated to different alignments. In the case where it is anti-aligned with the direction of applied load, as opposed to aligned, the effect should be reversed. That is to say, instead of the shear modulus being minimised at an

angle of 45°, it should now be maximised. Experimentally, this appears to be the case, as figure 6.8 shows. This data was collected in the same manner as the forward case and used the same pucks and contact pressures.

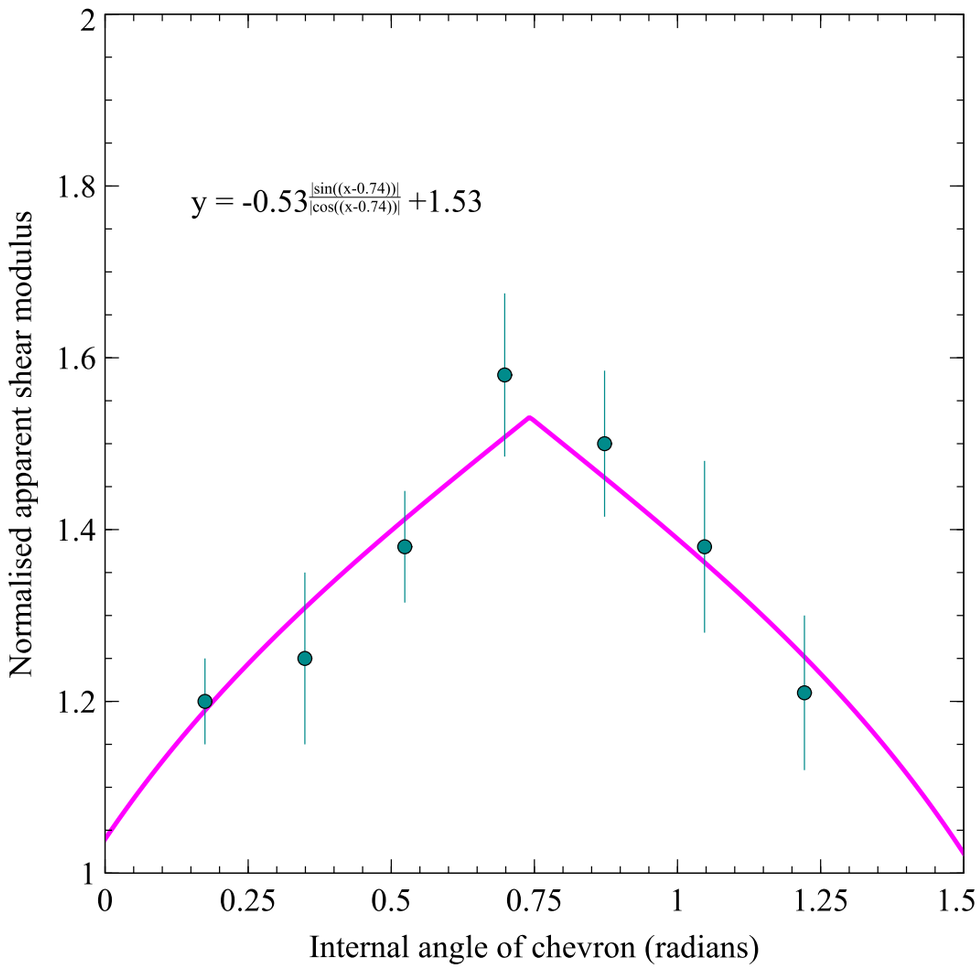

Figure 6.8: A plot of the normalized apparent shear modulus measured when a chevron patterned puck is translated along the traction platform, as a function of the internal angle of the chevron in radians. The direction of translation was anti-parallel to the peak of the chevron. Contact pressure was kept uniform at 0.69 MPa. Errors are due to the confidence bounds used to calculate the fits for the relative shear modulus. The change in the shear modulus as a function of internal angle is the reverse of what was observed in the parallel aligned case. Otherwise, the fit is the same: it scales according to the ratio of the sine and cosine of the angle subtended by the arms of the chevron from the normal axis. The function is again centred on approximately 45°/0.79 rad.

The collected data shows the normalized apparent shear modulus again changes as the ratio between the sine and cosine of half of the internal angle, however this time it is inverted: the shear modulus is maximal at 45° (experimentally measured as 43(±4)°), instead of minimal. This would imply the coefficient of friction is minimised for a 45° chevron, when translated against the direction of motion. The sliding block case is again recovered when the internal angle is 0° and 90°, as the normalized apparent shear modulus tends to 1

at these angles (experimentally measured as 1.06 ± 0.08). Again, this is explained by the same simple mechanical argument, this time with tensile strain instead of compressive strain: the probability of collision decreases, because asperities are pulled out of the way of their neighbours, rather than towards them.

The final case which was considered was the sideways case, where both of the alignment arguments previously outlined should simultaneously hold true.

Sideways Motion

Sample traction force maps taken when the chevron pucks were pulled sideways are shown in figure 6.9, evolving with the internal angle of the chevron.

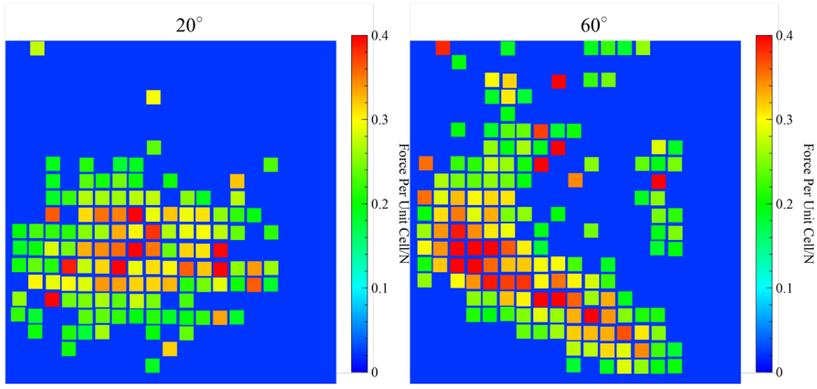

Figure 6.9: Example images of the evolution of the normalised traction force distribution under chevrons with different internal angles (20° and 60°), which are highlighted above each image, while they are pulled perpendicular to the direction of the chevron point. Each cylindrical puck which circumscribed the chevrons had a radius of 22.5 mm and a contact pressure of 0.69 MPa.

Unlike the cases where the chevron was aligned parallel and anti-parallel with the direction of the applied load, the change of net shear under the chevron in the perpendicular case is not as easy to predict. Each arm of the chevron is now angled either $+\theta$ or $-\theta$ from the normal axis, so it would be expected that their net effects should cancel out and the shear modulus should not change with the internal angle (assuming the effects are of equal magnitude and the chevron is properly aligned with the translation axis). What will change, however, is the width of the leading edges of the chevron: there will be two leading edges with a projected length in the direction of motion which scales as $cos\,(\theta)$. This will probably lead to some leading edge effect which scales according to the cosine of the internal angle. However, the chevron itself

is thick enough that the length of the internal and external sides (along the $tan(\theta)$ axis) are not proportional. At extreme angles, the internal sides begin to merge together.

The overall picture of this is as follows: there should be no net effect on the shear modulus from the bulk of the chevron (although each arm will likely experience different magnitudes of shear, in line with the previous two alignments). There should also be a leading edge effect which scales the shear modulus according to $cos\,(\theta)$ (although the changing width of the sides should make this noisy at extreme angles). The experimental picture begins to show this, with the normalized apparent shear modulus shown in figure 6.10. As before, this data was captured using the methods previously described for the forward case and the calibration of the shear modulus of the platform.

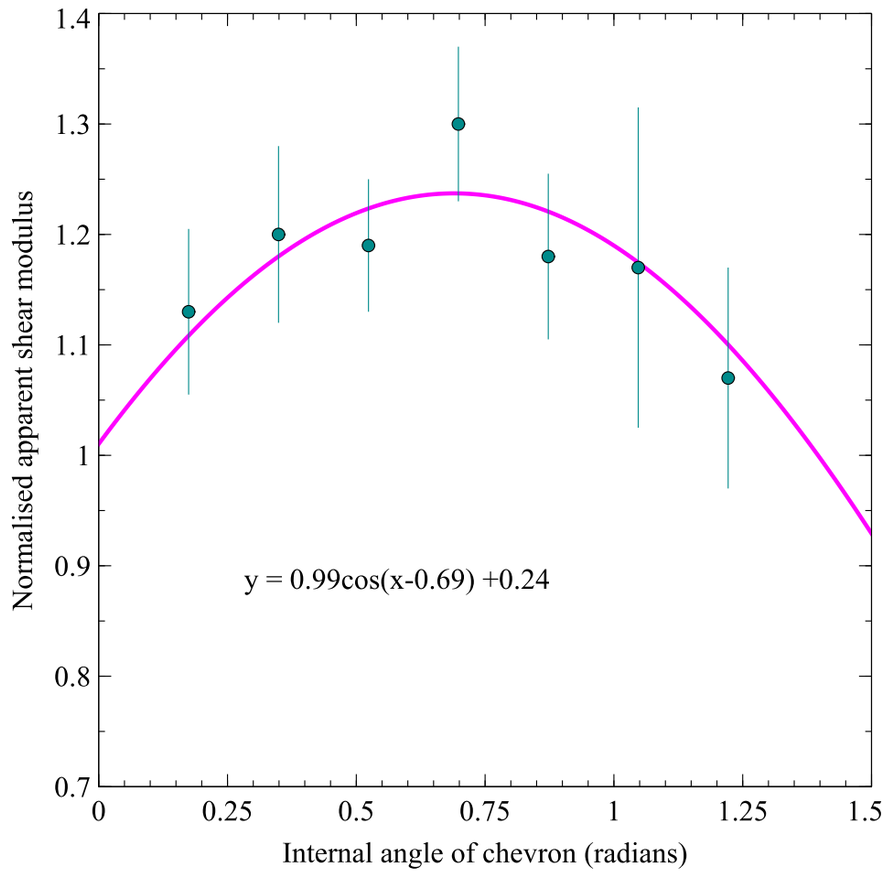

Figure 6.10: A plot of the normalized apparent shear modulus measured when a chevron patterned puck is translated along the traction platform, as a function of the internal angle of the chevron in radians. The direction of translation was perpendicular to the peak of the chevron. Contact pressure was kept uniform at 0.69 MPa. Errors are due to the confidence bounds used to calculate the fits for the relative shear modulus. The signal to noise ratio is quite poor, due to the (expected) minimal change in the relative displacement with respect to the internal angle. Beyond this, the features are also predictable. The first notable feature is the scale of the change is much less than the previously examined cases, varying by $\sim 20\%$ instead of $\sim 60\%$. Given the limited resolution of the traction platform and that each arm is roughly 4-5 unit cells thick (meaning low sample density in the bulk contact region), a value of this scale is not unreasonable for a leading edge effect. The variation can also be approximately fit with a cosine graph, although predictably it is noisy. The fit given here is $y = 0.99cos(\theta - 0.69) + 0.24$. It would still be expected that this would be centred on 45°/0.79 rad, and indeed it was centred on $40(\pm6)°/0.70(\pm0.1)$ rad.

As is expected, the shear modulus is again maximised at approximately 45° (experimentally measured as $40(\pm6)°$). However, the effect is much less pronounced than in either previous case, varying by $\sim 20\%$ instead of $\sim 60\%$. However, it is only the *net* effect where there is minimal change. Referring back to 6.9, the shear in both visible arms of the 60° is very different. Given the top arm has the same alignment as the parallel case, and the bottom arm the same alignment as the anti-parallel case, this is unsurprising and further supports the theoretical arguments.

6.3 Conclusion

The prototype traction force sensor was used to analyse the shear distribution under a sliding puck with a chevron-based pattern, resulting in more information on the fundamental interaction between hard and elastic surfaces. It was shown that a chevron-based contact area causes a shape dependent friction effect, which could be quantified using simple mechanical arguments of compressive or tensile strain.

When the direction of motion was aligned with the chevron it was shown that the relative net shear modulus scaled with the internal angle of the chevron (θ) by $0.604\frac{|sin(\theta-0.77)|}{|cos(\theta-0.77)|}+0.407$. This shows that the shape dependence of friction is governed solely by the internal angle of the chevron, and a simple mechanical argument based on compressive strain was proposed as the driving factor. Both the theory and experimental results show the maximum coefficient of friction is achieved with a chevron with an internal angle of 45° (44($\pm$2)° was experimentally measured), as is commonly considered the case from qualitative analysis.

Modifications to common theoretical models were then proposed, as a general key assumption (that asperities are far enough apart that they do not collide) must be false for the experimental results to hold true. It was proposed that the maximum force before the onset of sliding friction could be expressed as $F' = F\left(1+\frac{f\rho}{k}tan\left(\theta\right)\right)$, where F is the force determined from standard friction models, ρ is the asperity density, k the elastic modulus of asperities, and θ the collision angle. Further, more detailed, theoretical work would be needed to confirm this.

The orientation of the chevrons were then altered, and it was shown that the same arguments hold true in antiparallel and perpendicular orientations. In the antiparallel orientation, the apparent shear modulus scaled as $-0.53\frac{|sin(\theta-0.74)|}{|cos(\theta-0.74)|}+1.53$, which was likely caused by extensive strain. In the perpendicular case, the orientation of the chevron arms was a combination of the previous two cases, such that the effects cancelled out. The apparent shear modulus now scaled as $0.99cos(\theta-0.69)+0.24$, due to the leading edge effect at the interface.

Bibliography

[1] J. Hale, R. Lewis, and M. J. Carré, "Rubber friction and the effect of shape," *Tribology International*, vol. 141, 2020. DOI: https://doi.org/10.1016/j.triboint.2019.105911.

[2] V. C. Hoang, W. Zhan, Y. Fang, and P. Huang, "Experimental and simulation analyses of the stress field of slider-on-block contact for static and slip states," *SN Applied Sciences*, vol. 2, 2020.

[3] V. Pinto, T. Ramos, S. Alves, *et al.*, "Comparative failure analysis of pla, pla/gnp and pla/cnt-cooh biodegradable nanocomposites thin films," *Procedia Engineering*, vol. 114, 2015. DOI: https://doi.org/10.1016/j.proeng.2015.08.004.

[4] T. Edeskär, "Technical and environmental properties of tyre shreds focusing on ground engineering applications," 2004.

[5] K.-S. Shih, S.-Y. Jhou, W.-C. Hsu, *et al.*, "A biomechanical investigation of athletic footwear traction performance: Integration of gait analysis with computational simulation," *Applied Sciences*, vol. 10, 2020. DOI: 10.3390/app10051672.

[6] S. N. Srihari and Y. Tang, "Computational methods for the analysis of footwear impression evidence," in *Computational Intelligence in Digital Forensics: Forensic Investigation and Applications*. Springer International Publishing, 2014, vol. 555. DOI: 10.1007/978-3-319-05885-6_15.

[7] J. A. Greenwood and J. B. P. Williamson, "Contact of nominally flat surfaces," *Proceedings of the Royal Society of London. Series A, Mathematical and Physical Sciences*, vol. 295, 1966.

Chapter 7

Advanced Corrections

In this chapter, a pair of preliminary experiments are briefly detailed. the first is a modification to the method of calibrating the contact imaging device, so hard objects can be imaged instead of soft objects. The second is a combination of the contact and traction devices, which shows how they can be used simultaneously and some additional considerations which have to be made as a result.

7.1 Hard Contacting Objects On A Contact Platform

Until now, the contacting objects have been soft. They have had a Young's modulus at least two orders of magnitude lower than the waveguide they are pressed into, for example PMMA has a Young's modulus of 2.9 GPa[1] whereas it is 1.2 MPa for PDMS [2] and between ∼300-800 kPa for human flesh [3], [4]. This means that the contacting object deforms significantly more than the waveguide, such that the waveguide can be approximated as perfectly rigid. This would mean the measured FTIR response is solely due to the deformation of the contacting object. However, in the case where the contacting object is stiffer than the waveguide, this assumption no longer holds. Practical versions of the cases considered here would involve contacting objects like steel cleated shoes are an example, as steel has a Young's modulus of around 200 GPa [1].

No cleated shoes were available here, however ball bearings provide a similar analogue for illustration purposes. An example of this, with 5 mm diameter bearings pressed into the wall of a perspex storage container which has been turned into an FTIR waveguide, is shown in figure 7.1.

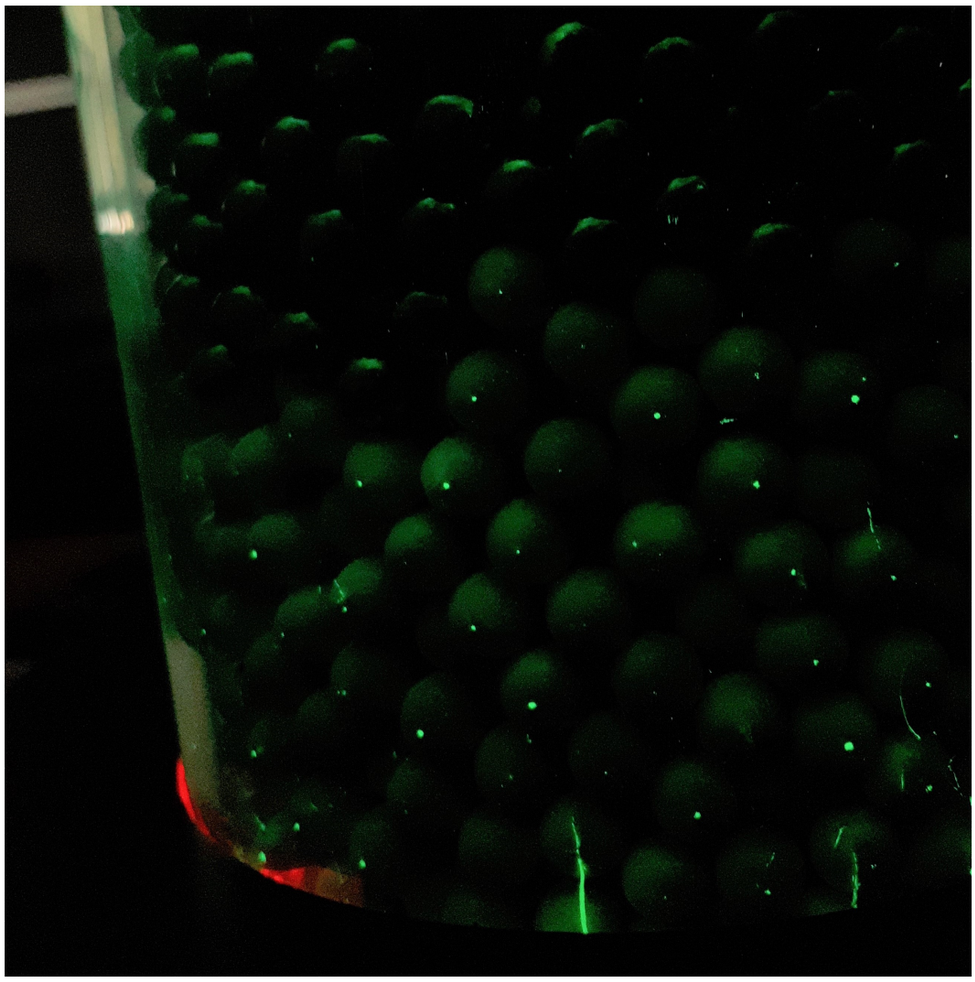

Figure 7.1: An example of the FTIR images produced when a contacting object (5 mm diameter ball bearings) is pressed against a waveguide (PMMA tube) with significantly lower Young's modulus. The FTIR waveguide used here uses green light, and the small green patches are the contact points. The white streaks at the bottim are scratches in the perspex, highlighting how useful a protective PDMS coating can be.

In this image, the ball bearings are pressed against the inside of a cylindrical waveguide, which was illuminated with green light. The small green patches in the image are the contact points. As neither the object nor waveguide is particularly deformable, these patches are quite small for the given load (values of the order of 10 N giving patches of the order 0.1 mm^2 in size). These small contact patches also translate to flat surfaces - any natural surface height variation will lead to a small actual contact area which does not increase significantly. The camera could be brought close, to accurately image the distributions in patches such as these, but the field of view would be exceedingly small. It was therefore necessary to alter some property of the waveguide to account for this, so the pressure distributions under large contacting objects could be feasibly measured.

The solution for this had already been reached: a thin (<0.1 mm) layer of

PDMS added as a protective layer onto the perspex. This thin layer increased the contact area enough that the pressures could be easily imaged. Some consideration was necessary for how this would change the contact mechanics during calibration, however. Previously, both the waveguide and contacting object could be considered bulk objects, with well defined deformations. In this arrangement, the contacting object is still a bulk body, but the waveguide must be considered as a thin deformable film attached to another bulk (rigid) body. A version of this problem is well known, and thus a solution could be easily implemented [5].

The problem consists of a rigid semi-infinite plane, covered by a deformable thin film, and a rigid contacting sphere. "Thin", in this instance is defined as the thickness of the film (h) being much less than the contact radius between the surface and body (a), i.e $h << a$. This setup is shown schematically in figure 7.2. A sphere was chosen as the contacting object for calibration because the radial pressure distribution is well defined for this thin-film correction, and axi-symmetric loading is simpler than for a cylinder.

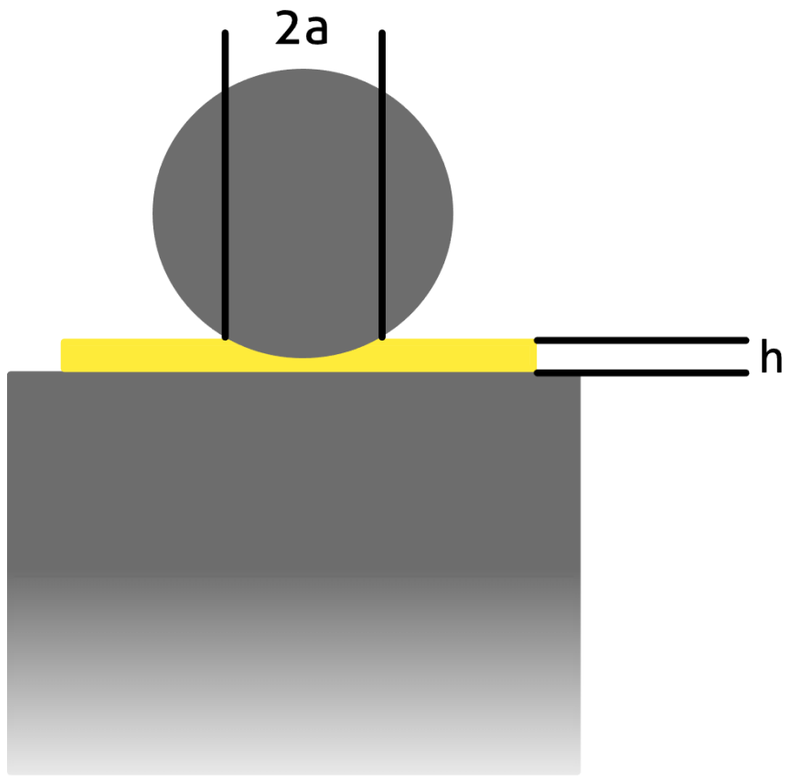

Figure 7.2: A schematic outline of the thin film problem with a spherical contacting object. This consists of an elastic thin film of thickness h, sandwiched between two rigid bodies (grey). The rigid bodies are a semi-infinite plane and a sphere. The sphere makes contact with the thin film and the associated contact patch has a radius a. When the contact patch is sufficiently large ($a >> h$), the thin film correction must be applied, as the rigid semi-infinite plane will begin to restrict and alter the compressive behaviour of the thin film.

The thin film does not deform as if it were a semi-infinite plane, because the rigid plane behind it restricts its deformation, resulting in the thin film correction to the pressure distribution P [5]:

$$P \rightarrow P' = P\left(1 + \beta\left(\frac{a}{h}\right)^3\right). \tag{7.1}$$

Here, β is a correction factor which depends on the Poisson ratio (ν) of the surface. If it is assumed that the surface is incompressible ($\nu = 0.5$), then it has been found that $\beta = 1.33$. It should be made clear that this will not alter the pressure distribution under a sphere and its associated contact mechanics: the FTIR response will still follow the theory outlined in chapter 2. However, an additional correction will need to be added when calibrating for the forces, because it would be the thin film on the waveguide which would be deforming,

rather than a bulk soft body.

It is possible to implement a thin film correction to the forces in the following way. First, the position-dependent intensity scaling factor of the waveguide would have to be calibrated. This is independent of the object used for calibration, so a soft object may be used as before, and give a normalisation similar to that in figure 3.3. Next, the intensity-force curve for a hard contacting object will need to be measured. Using a sphere gives well defined radially dependent pressures [6], and therefore intensities, which can be calculated if the total load is known. However, equation 7.1 shows that the pressures are also dependent on the thickness of the thin film. The thickness of the film may be measured, say with callipers, and used to correct the pressures. The intensity-force calibration may then proceed as before. However, there is an additional consideration: it is unlikely the thickness of the thin film is constant over the entire waveguide surface. Therefore, it would be ideal to directly use the backscattered light from the contact patches to calibrate the thickness over the whole waveguide.

This step has been achieved, and was undertaken by first measuring the value of h at some arbitrary position of the waveguide and measuring the distribution of P' as a function of applied load. At any other given point on the surface, where only h had changed, the distribution would need to be scaled. By taking multiple additional measurements of P' at known positions, a two dimensional fit can be calculated across the waveguide that normalises this distribution for varying values of h. This fit of different values of h is shown in figure 7.3.

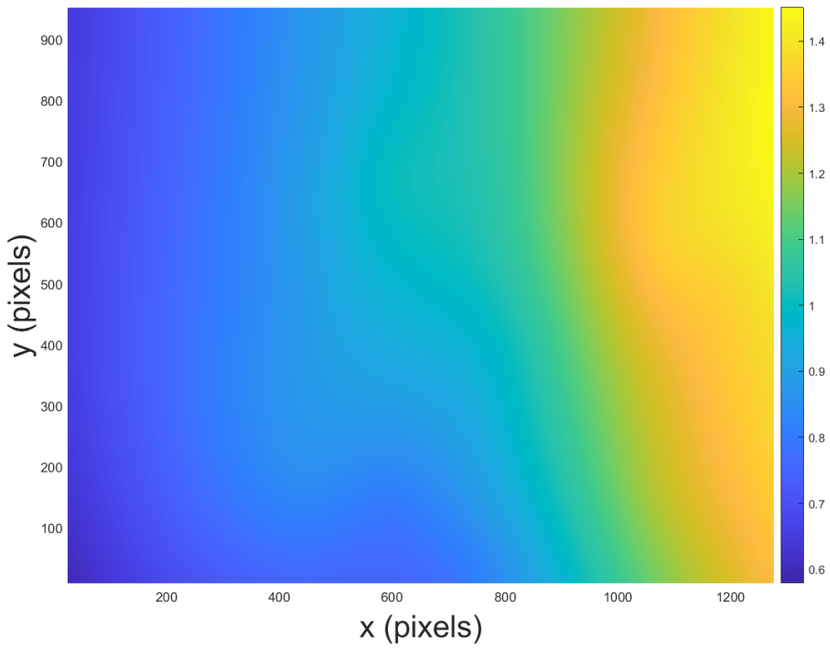

Figure 7.3: An example of the scaling factor needed to account for varying thickness of the thin PDMS layer which was added on top of the FTIR waveguides. This was needed for the thin film correction used when a contacting object was stiffer than the waveguide. The value of the scaling factor is highlighted in the legend on the right. This was created using a poly 2-2 fit based on data points collected across the waveguide surface.

This fit shows considerable variation in the relative thickness of the thin film, changing by ±40% across the surface. The shape of this distribution would indicate the cause for this was the waveguide not being sufficiently level when the PDMS was poured (the method was to level it using a spirit level, by eye). This is evidenced by the thickness increasing along the x-direction, meaning the left of the waveguide was higher than the right and the uncured PDMS slowly pooled in the other direction. At the scale of the waveguide (∼200 mm), it would only require a 0.2° tilt to achieve this variation.

7.2 Dual Contact-Traction Imaging Device

So far, two devices have been designed and demonstrated: a contact pressure imaging device, and an in-plane traction imaging device. Were these two devices to be combined, then a complete picture of the forces at an interface could be made. The device demonstrated here was a combination of the previous two devices, with some important modifications to avoid cross-talk with the two sensors. The traction layer itself was already designed with this in mind, so modification was minimal. The only change that was required was

to remove the thin black layer of PDMS, as this absorbed the wavelengths used in the contact imaging setup. This added more noise to the background and meant the room light had to be kept turned off. The greatest change was in the light sources used in both imaging setups. The contact imaging light source was changed to near infra-red (wavelength 920 nm), as Rhodamine B is transparent at this wavelength but contacting materials (like human skin) are still reflective. It is also relatively easy to source a camera that can image at this wavelength, as it is commonly used for night-vision sensing [7], [8].

The camera that was chosen was a Raspberry Pi NoIR camera, which is based on a standard Sony IMX219 visible light sensor with a resolution of 3280×2464 and the infra-red filter removed [9]. Presumably due to frequency doubling in the colour filter layer in the individual sensor elements, this meant that the infra-red signal was received in the blue channel of the camera, which is the only sensor channel with a quantum efficiency above the background level (5%) at this doubled frequency (460 nm) [10]. This sensor design was not explicitly made to receive NIR light, so the sensitivity was lower than at visible wavelengths and higher exposure times/lower frame rates were necessary. The infra-red signal being received by the blue sensor channel also meant any blue and NIR light would be indistinguishable (although a band-pass filter could solve this, if available). Aside from the intensity of the LEDs and the camera being different, the received FTIR signals will also potentially be scaled because of the higher wavelength of light, compared to the red light used in the contact platform (920 nm vs 632 nm). As the attenuation constant of an evanescent wave is inversely proportional to frequency [11], this will mean an NIR wavelength will travel further into the air and scatter off a larger volume of asperities and therefore the received signal will also be scaled higher.

As the blue channel was now being used for the contact imaging, it could no longer be used for illuminating the dots. Instead, green light was used for illumination (which still had a strong absorption peak, see figure 3.16), and red light was used to image the emission of the dots. As the overall quantum efficiency is lower with these wavelengths, the emission from the dots was dimmer and therefore larger exposure times were required for this part of the device as well.

The final change was to the waveguide itself. The previous contact and traction devices both used LED-based waveguides as their illumination source, this device does the same by alternating green and NIR LEDs in a mounting bracket made around the perspex slab, which is illustrated in figure 7.4. As each LED has a slightly different operating voltage (1.6V for green and 1.4V for NIR), they cannot be added in series without causing an overvoltage in the NIR LEDs. This causes the NIR LEDs to also emit in the red, and make tracking the dots impossible when an object which can scatter red light is in contact. As such, two series loops had to be used.

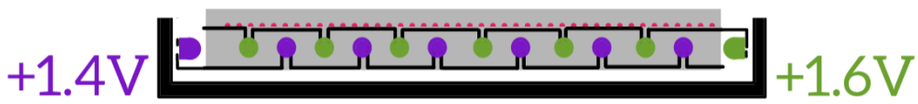

Figure 7.4: A diagram of the completed dual contact-traction imaging waveguide and its components. The green LEDs are represented in green, NIR LEDs in purple, and the Rhodamine B doped dots they are aligned relative to in red. As in the traction device, a 3 mm thick waveguide containing 2.5 mm radii Rhodamine B dye doped dots was attached to a 25 mm×600 mm×300 mm perspex slab. A 3D printed bracket, with spaces for the LEDs, housed the waveguide. The circuits that connected the LEDs together have also been illustrated. Two circuits were required because of a slight voltage mismatch between the green and NIR LEDs, which caused the NIR LEDs to also emit red light if added in series with the green LEDs.

It was not possible to have another mounting bracket for the new waveguide and camera mount built in the remaining months, due to a backlog in the available machine workshop. Instead, the waveguide was simply sat onto a pair of cast iron blocks and the camera held in place below it with masses on the ribbon cable connecting it to a Raspberry Pi. Software was then written in Python to control the camera parameters (exposure time, capture resolution, shutter speed, white balance, and desired data port) and capture images of the surface.

Some simple tests were then performed with this waveguide. Objects were brought into contact with the waveguide and the resulting images captured. Attempts were then made to completely isolate the contact and traction signals. The clearest results with the dual contact-traction device were gained when a

finger was pressed into the device. Separating out the raw images into their individual channels gave the images in figure 7.5. The most obvious problem here is that the dots are not completely transparent to the NIR light. Colour bleeding from ambient light/the green LEDs was easily disproven by turning off the green LEDs. The most likely reason for this is contaminants in the PDMS layer. These will introduce additional interfaces that will break the internal reflection condition and scatter light, independent of whether the contaminant is optically transparent or not.

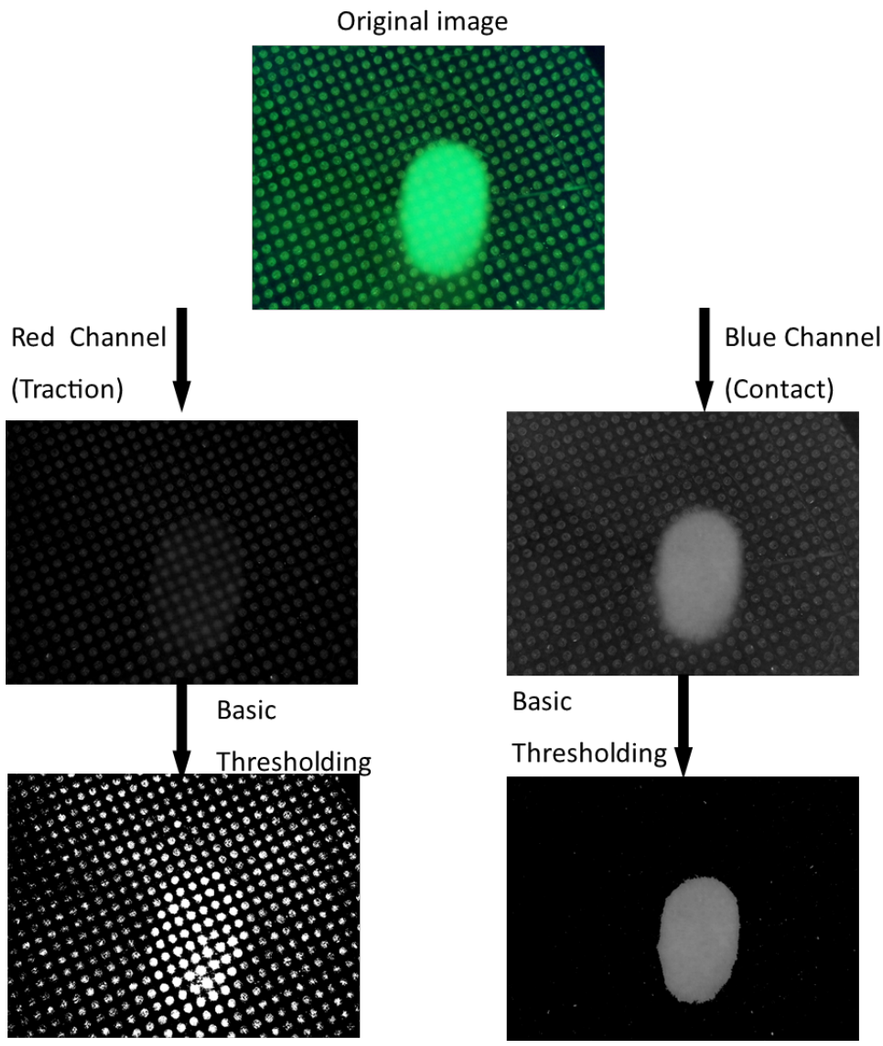

Figure 7.5: Examples of the processed and unprocessed contact and traction responses extracted from a single frame taken with the dual contact-traction setup. In the raw responses, there appears to be cross-talk between the two signals. This is caused by the contacting object scattering the emitted light from the Rhodamine B dye, and imperfections breaking the internal reflection condition for the NIR light. This effect is minimal enough that it can be easily removed with thresholding, as the processed images show. Most importantly, the scattering and absorbance from the dots has not noticeably affected the contact results, ie there is no circular patch in the response where the back-scattered NIR light has been further scattered by the dye. Unlike in previous experiments, only rudimentary threshold has been applied. The same image filtering techniques will clear the images even further, and additional options are available for filtering the traction image, as the contact patch is well defined.

Some of these imperfections are caused by dust/debris getting trapped between the layers during the moulding process (pieces of white silicone are visibly present), however the main cause is identified by extracting the florescence component (red colour channel) from highly magnified images of the dots. These images were captured with a Sony camera fitted with a macro lens at a resolution of 2064×4624, meaning $0.5\,\mu m \times 0.4\,\mu m$ could be resolved. In these images, like in figure 7.6, large variations in light intensity throughout the dots are self-evident. As these are florescence images, the only source of this light can be emission from the Rhodamine B dye. Further, the FTIR result appears unaffected by the dots themselves.

The FTIR results would not be unaffected by the dots if the dye was actively absorbing and scattering the NIR light, rather than just breaking the internal reflection condition. This would only be the case if the solvent the dye was dissolved in was evaporating and recrystallising the dye, causing small hollows in the PDMS. As a test for this, the intensity of each region of the dots was counted and binned in figure 7.6. The fluorescent intensity of a dye is proportional to its concentration [12]. It has also been previously shown that the size distribution of crystals which form in a suspended medium (like Rhodamine B crystallising in PDMS, by evaporation of solvent) forms an approximately log-normal distribution [13]. Therefore, if this formation was driving the fluorescence within the dots, the observed intensity count should also follow a function of this form. If it was contamination from other debris, or simple absorption, a more symmetric distribution would be expected. A log-normal function was indeed discovered, so the source of the fluorescence was likely identified. Given this indicates that the source of the light within the dots is simply additional background interfacial scattering, it was determined to not affect the results, although small changes in the Young's modulus would be expected in these regions because of the additional interfaces

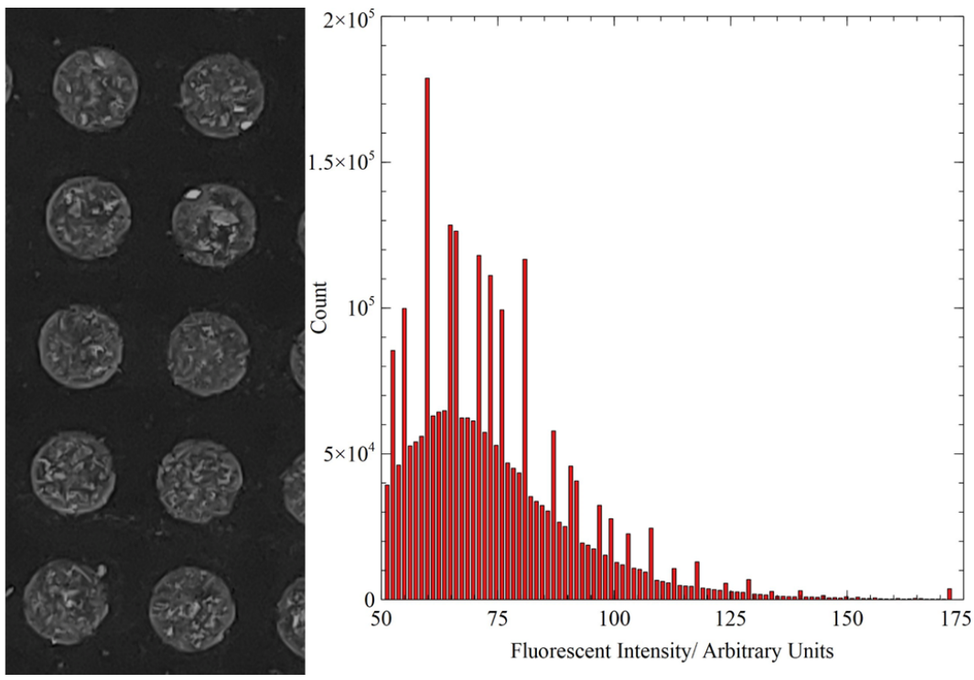

Figure 7.6: A close up view of the fluorescence of the dye-doped regions of the dual contact-traction waveguide, showing variations in emitted light intensity throughout each dot. Right of this is the binned fluorescent intensity data. Knowing the fluorescent intensity is linearly related to the dye concentration, and that this is proportional to the size of dye crystals [12], the distribution of sizes matches what is expected for crystallisation as the dye drops out of solution [13].

The second observation is a slight FTIR response in the traction pattern from the dots, however this was below the background noise threshold and therefore did not alter the apparent size of the dye-doped regions. Experimentally, both of these aberrations could be removed from the desired signals by simple thresholding, given in figure 7.5.

Bibliography

[1] *Tables of physical and chemical constants / originally compiled by G.W.C. Kaye and T.H. Laby ; now prepared under the direction of an editorial committee.* 16th ed. 1995, ISBN: 0582226295.

[2] J. S. Sharp, S. F. Poole, and B. W. Kleiman, "Optical Measurement of Contact Forces Using Frustrated Total InternalReflection," *PHYSICAL REVIEW APPLIED*, vol. 10, 2018. DOI: 0.1103/PhysRevApplied.10.034051.

[3] C.-C. Hsu, W.-C. Tsai, C. Chen, *et al.*, "Effects of aging on the plantar soft tissue properties under the metatarsal heads at different impact velocities," *Ultrasound in medicine biology*, vol. 31, 2005. DOI: 10.1016/j.ultrasmedbio.2005.05.009.

[4] W. R. Ledoux and J. J. Blevins, "The compressive material properties of the plantar soft tissue," *Journal of Biomechanics*, vol. 40, 2007. DOI: https://doi.org/10.1016/j.jbiomech.2007.02.009.

[5] K. R. Shull, "Contact mechanics and the adhesion of soft solids," *Materials Science and Engineering: R: Reports*, vol. 36, 2002. DOI: https://doi.org/10.1016/S0927-796X(01)00039-0.

[6] 1. Johnson K. L. (Kenneth Langstreth), *Contact mechanics [electronic resource] / K.L. Johnson.* eng. Cambridge, 1985, ISBN: 9781615832187.

[7] K. Chrzanowski, "Review of night vision technology," *Opto-Electronics Review*, vol. 21, 2013. DOI: 10.2478/s11772-013-0089-3.

[8] A. W. Browne, E. Deyneka, F. Ceccarelli, *et al.*, "Deep learning to enable color vision in the dark," *PLOS ONE*, vol. 17, 2022. DOI: 10.1371/journal.pone.0265185.

[9] R. P. Ltd, *Raspberry Pi Documentation [online]*. 2022. [Online]. Available: https://github.com/raspberrypi/documentation.

[10] M. A. Pagnutti, R. E. Ryan, G. J. C. V, *et al.*, "Laying the foundation to use Raspberry Pi 3 V2 camera module imagery for scientific and engineering purposes," *Journal of Electronic Imaging*, vol. 26, DOI: 10.1117/1.JEI.26.1.013014.

[11] E. Hecht, *Optics*, 5th Edition. Harlow : Pearson Education, 2017, ISBN: 9781292096933.

[12] A. T. Rhys-Williams, *An Introduction to Fluorescence Spectroscopy*. Perkin Elmer, 2000.

[13] D. Donhowe, R. Hartel, and R. Bradley, "Determination of ice crystal size distributions in frozen desserts," *Journal of Dairy Science*, vol. 74, 1991. DOI: https://doi.org/10.3168/jds.S0022-0302(91)78521-4.

Chapter 8

Overall Conclusion

The primary outcome of this work was the development and application of two novel devices: a contact force sensor, and a traction force sensor. The contact force sensor, which takes advantage of frustrated total internal reflection was then applied to some simple bio-mechanics exercises, to demonstrate the devices ability to resolve complex pressure distributions at a high resolution and speed. The exercises themselves demonstrated how useful bio-mechanical and product design data can be recovered from the additional information these two-dimensional pressure distributions give.

The design of the traction device was then demonstrated, and the results it produces shown to compare well to what is expected from simple elastic FEM simulations. The device was then used to analyse the shear below various objects and the shape dependence of friction between an elastic and inelastic body was studied. Using various polygon shaped contacting objects, the shape dependant shear pattern during rotational motion was analysed and a modification to the force distribution discovered. Using this, a modification to the standard simple elastic simulations was proposed, to better account for elastic materials.

Using a set of chevron based patterns, a more fundamental analysis of the shape dependence of friction was undertaken. It was concluded that the likely cause of this was compressive/tensile strain between colliding surface elements redistributing the frictional load off-axis. This eliminates one of the standard assumptions used in theoretical modelling of friction, so an alteration the standard theoretical models was proposed, which both captures the shape

dependence of friction in elastic materials, and recovers the standard friction equations at high Young's moduli.

Finally, two shorter side experiments were shown: the first demonstrated how, with additional corrections, the contact imaging device can be used to image contacting objects harder than the FTIR waveguide material, rather than the soft objects generally used here. The second experiment demonstrated how the contact and traction imaging devices could be combined, to produce a device capable of imaging both sets of forces simultaneously.

Chapter 9

Future Work

The most obvious continuation point is to produce a large scale dual contact-traction imaging device. The work here has been done in such a way that this can naturally develop with little change to the materials or methods needed. The basic prototype developed here could easily be up-scaled with a higher resolution camera. Modifying the dye concentration and dot size in the traction layer would further expand the range of possible studies. It would also be logical to repeat the training exercises demonstrated in the contact imaging experiments, to analyse the entire force distribution an athlete generates with the floor and attempt to identify how these distributions relate to desired/undesired motion.

The traction distributions analysed here have also only been under static friction regimes, sliding or rolling friction conditions would be a natural progression, especially when analysing patterns for objects like tyres. Further details on possible avenues to explore, separated by device type, are highlighted below.

9.1 Contact Imaging

There are still a number of avenues to explore with the contact imaging device. Mono-colour soft and stiff objects can be imaged using the device, and colour can be corrected for so long as the colour is uniform. Any large variation in surface colour due to dirt, wear, or simply stylistic choice will currently make the device unusable. In these situations it would be necessary to identify each region separately and assign a scaling factor to each colour region. It is possible that this could be achieved by the following process: adding a ring light under the platform that will illuminate an object without producing an FTIR response. Next, capture an image of this and identify the colour and shape of each region. Turn off this ring light and turn on the FTIR waveguide and capture an image of the FTIR response. If this happens at sufficiently high frame rates that the contacting object has not observably moved or changed shape, the two regions are comparable. If the waveguide was calibrated for a specific colour (for example pure white, RGB(255,255,255)), then the colour regions will scale linearly with the colour of the regions identified by the camera. The spectral response of the camera will already have been accounted for when capturing the colours. For example, if there are two regions identified with colours RGB(100,0,0) and RGB(255,0,0), and red light is used as the waveguide source, then each colour region will need to be scaled by $\frac{100}{255}$ and $\frac{255}{255}$, respectively.

This assumes the mechanical properties of the different coloured regions are comparable - variations in the stiffness of the object will make this method invalid and would need to be corrected for in some other way. Indeed, it is less trivial to identify an object with combined soft and stiff regions even if they are the same colour, and this would need to be explored in detail. Aside from these shortcomings, the FTIR contact imaging device is usable and could readily be applied to more detailed contact mechanics or bio-mechanics studies than those presented here.

9.2 Traction Imaging

There are numerous avenues that could be explored using the traction imaging device. These are detailed throughout this section but may be summarised into the following groups: continuation of the rotational traction experiments, continuation of the translational traction experiments, and analysing materials of different Young's moduli. The method of imaging used in this device may also be applied to more topics, and this is a separately detailed point.

The rotational experiments have already shown how the distribution of shear during rotation is modified compared to standard elastic arguments, and this could be explored further, in order to determine the dependencies in more detail. The case of translating chevrons would be a more natural point to continue detailed theoretical analysis, however, as it is simpler to arrange.

In order to test the proposed cause of the shape dependence, it would be ideal to design a simulation which fully models the surfaces and their asperities as a mass-spring system, on a molecular scale, and view the shear over time. Collisions between asperities, and their associated shear before micro-slip, are key properties that could only reasonably be observed in this way. Earlier this year, a similar simulation has demonstrated the super-computing power available to researchers is now sufficient to allow this level of detail (in their case, frictional heating was studied) [1]. This could be reapplied to the elastic arguments presented here.

Other avenues of research, with less extreme resource requirements, are also available in this regard: simply testing different well known mechanical shapes. Moving on to softer contacting objects is also sensible when mimicking shoes and tyres. It would also be reasonable to test the remaining parameter space for rotational corrective force calculated here: It was not analysed how this effect varied with Young's modulus of the elastic waveguide layer. This would be approached by making and calibrating numerous waveguides of various different Young's moduli and would be a significant investment in time and materials. Beyond this, some improvements could be made to make the devices more applicable to other areas of study.

In order to be suitable for measuring large surface areas, to apply to biomechanics/engineering situations, or smaller areas in higher detail, the resolution of the device needs to be improved. The first step towards this was the dual contact-traction device.

9.3 Dual Contact-Traction Imaging

There is a large amount of work that can still be done with the dual contact-traction imaging waveguide - the design is not ideal, but a viable proof of concept. It has been shown how this can be implemented using various frequencies of light both inside and outside the visible spectrum. A large potential limitation here is the reflectivity of dyes used in common objects in the NIR wavelength used here (940 nm). A large number dyes do not scatter light strongly at this wavelength, and this will limit the ability to resolve pressures. Cameras which will image at other wavelengths are uncommon, and as a result expensive and low resolution. To take the greatest advantage of the setup, a different fluorescent dye would be ideal. This dye should be excited outside of the visible spectrum (and not be observable by the camera, even through any frequency doubling effect), emit over a small range of visible wavelengths, be optically transparent over the remainder of the visible spectrum, and be soluble in an uncured elastomer like PDMS. This would require both research (as optical characteristics are commonly available) and experimentation (solubility in monomer solutions and ideal dye concentrations) in order to optimise the setup based on the use. This would be time consuming, and potentially expensive, but otherwise a simple avenue. Aside from this, the combined contact-traction setup would have all the potential of the previous devices.

Bibliography

[1] S. Eder, P. Grützmacher, M. Rodríguez Ripoll, C. Gachot, and D. Dini, "Does speed kill or make friction better?—designing materials for high velocity sliding," *Applied Materials Today*, vol. 29, 2022. DOI: https://doi.org/10.1016/j.apmt.2022.101588.

Chapter 10

Ethics Declarations

This author declares no competing interests.

List of Figures